



## RESEARCH ACTIVITIES

### Theoretical and Computational Molecular Science

It is our goal to develop new theoretical and computational methods based on quantum mechanics, statistical mechanics, and molecular simulation in order to predict and understand the structures, reactions, and functions of molecules in gas, solution, and condensed phases as well as in nano- and bio-systems prior to or in cooperation with experiment.

# Theoretical Study and Design of Functional Molecules: New Bonding, Structures, and Reactions

Department of Theoretical and Computational Molecular Science  
Division of Theoretical Molecular Science I



NAGASE, Shigeru  
OHTSUKA, Yuki  
TANAKA, Masato  
KATOUDA, Michio  
GAO, Xingfa  
GUO, Jing-Doing  
WANG, Lu  
MIYAKE, Toshiko  
LUO, Gangfu  
GHOSH, Manik Kumer  
WATANABE, Hidekazu  
SAKAKI, Shigeyoshi  
YAMADA, Mariko  
KONDO, Naoko

Professor  
Assistant Professor  
IMS Fellow  
Post-Doctoral Fellow  
Post-Doctoral Fellow\*  
Post-Doctoral Fellow  
Post-Doctoral Fellow†  
Post-Doctoral Fellow‡  
Post-Doctoral Fellow  
Post-Doctoral Fellow  
Post-Doctoral Fellow  
Visiting Scientist  
Secretary  
Secretary

In theoretical and computational chemistry, it is an important goal to develop functional molecules prior to or in cooperation with experiment. Thus, new bonds and structures provided by heavier atoms are investigated together with the reactivities. In addition, chemical modification and properties of nano-carbons are investigated to develop functional nanomolecular systems. Efficient computational methods are also developed to perform reliable quantum chemistry calculations for small and large molecular systems.

## 1. Application of Second-Order Møller-Plesset Perturbation Theory with Resolution-of-Identity Approximation to Periodic Systems

Electron correlation plays an important role in the accurate description of the conductive, optical, and magnetic properties of periodic systems. Second-order Møller-Plesset perturbation theory (MP2) is the simplest method to account for electron correlation at an *ab initio* level. Periodic boundary condition (PBC) calculations by the MP2 method (PBC MP2) have been developed. However, the computational cost is considerably high and practical applications are limited to small periodic systems. A promising approach to reduce the computational cost is resorting to the resolution-of-identity (RI) approximation of four-center two-electron atomic integrals (ERIs). However, no attempt has been made to incorporate the RI approximation with the PBC MP2 method because the lattice sums of long-range AO ERIs show extremely slow  $r^{-1}$  decay.

Therefore, we have developed an efficient PBC RI-MP2 method in the crystal orbital framework, which is applicable to large periodic systems.<sup>1)</sup> In this method, the slow convergence of lattice sum of long-range AO ERIs is avoided using Poisson and Gaussian mixed auxiliary basis functions. To assess the accuracy and computational efficiency of the developed PBC RI-MP2 code, test calculations were performed for trans-polyacetylene using the 6-31G\*\* basis sets. PBC RI-MP2 is

98 times faster than PBC MP2, and the energy difference between PBC RI-MP2 and PBC MP2 is only 0.4 mH. In addition, the required memory and disk sizes for PBC RI-MP2 are much smaller than those for PBC MP2. To calculate much larger periodic systems, we plan to develop an efficient parallel code of PBC RI-MP2.

## 2. Molecular Tailoring Approach to Very Large Molecules

Several divide-and-conquer approaches have been developed to overcome the high scaling problem of *ab initio* calculations. The molecular tailoring approach (MTA) was interfaced with the efficient MP2 and RI-MP2 codes developed in our group.<sup>2,3)</sup> The performance was extensively benchmarked for a variety of large molecular systems and critically compared with the popular fragment molecular orbital (FMO) method. It was found that FMO2-MP2 is superior to FMO3-MP2 and MTA-MP2 in terms of computational costs. However, the errors of FMO2-MP2 are considerably large and beyond chemical accuracy. FMO3-MP2 is accurate for biological systems, while it is unsuccessful for water clusters. The errors of MTA-MP2 are within 1 kcal/mol for all systems with reasonable time advantage. The accuracy of FMO decreases for the basis sets that include diffuse functions. In contrast, MTA performs well regardless of basis sets.

## 3. Application of Projector Monte Carlo Method Based on Slater Determinants to Excited States

A projector Monte Carlo method based on Slater determinants (PMC-SD) is expanded to excited state calculations.<sup>4)</sup> Target excited states are calculated state-by-state by eliminating the components of the lower states from the imaginary time propagator. As the test calculations of excited states of

H<sub>2</sub>O show, the accuracy of the PMC-SD method is improved systematically by increasing the number of walkers and the full-CI energies are obtainable as a limit for a given basis set. The avoided crossing of covalent and ionic states in the dissociation of LiF is well reproduced using the PMC-SD method.

#### 4. New Bonds Provided by Heavier Main Group Elements and Functionalization of Endohedral Metallofullerenes and Nanographenes

Silicon behaves like carbon in forming covalent bonds to four neighboring atoms. These bonds form the framework of many organosilicon compounds and crystalline silicon. Silicon can also form a pentacoordinated anionic structure, a so-called silicate. No compounds containing a direct bond between two silicate moieties (disilicates), where two silicate structures are combined in one species, have been reported because of the electronic repulsion between the anionic halves and difficulty preventing the release of anions. However, we have developed a stable compound containing the linkage of two pentavalent silicon atoms, as shown in Figure 1.<sup>5)</sup> The unique electronic properties are promising for the construction of functional materials with silicon wire made up of silicate chains.

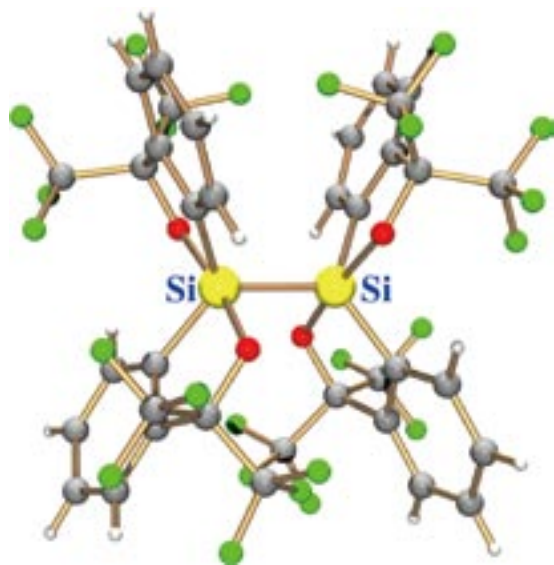


**Figure 1.** The stable bond between pentavalent silicon atoms.

The concept of aromaticity has long played an important role in carbon chemistry since the discovery of benzene in 1825. To determine that the heavier group 14 elements can sustain aromaticity, silicon, germanium, and tin analogs of carbocyclic aromatic compounds have been synthesized, most of these showing considerable aromaticity. However, there has

been no clear evidence of whether the concept of aromaticity can be expanded to the ring incorporating the heaviest lead atom. Very recently, dilithioplumbole has been successfully synthesized and isolated in collaboration with our research group.<sup>6)</sup> Relativistic theoretical calculations show that its cyclic compound has considerable aromatic character as a result of the important overlap between 2p (C) and 6p (Pb) orbitals. The present results highlight the future possibility of introducing heavier elements including Pb into a broader range of carbon frameworks.

Chemical functionalization of endohedral metallofullerenes regulates the positions and movements of the encapsulated metal atoms.<sup>7)</sup> This control of metal positions and movements within fullerene cages can be valuable for designing functional molecular devices with new electronic or magnetic properties. Also investigated are graphene oxides and monovalency defects in graphene.<sup>8,9)</sup>

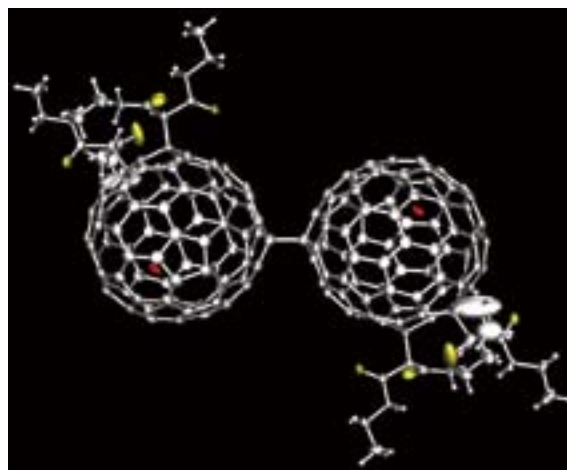


**Figure 2.** Functionalization of endohedral metallofullerenes.

#### References

- 1) M. Katouda and S. Nagase, *J. Chem. Phys.* **133**, 184103 (9 pages) (2010).
- 2) M. Katouda and S. Nagase, *Int. J. Quant. Chem.* **109**, 2121–2130 (2009).
- 3) A. P. Rahalkar, M. Katouda, S. R. Gadre and S. Nagase. *J. Comput. Chem.* **31**, 2405–2418 (2010).
- 4) Y. Ohtsuka and S. Nagase, *Chem. Phys. Lett.* **485**, 367–370 (2010).
- 5) N. Kano, H. Miyake, K. Sasaki, T. Kawashima, N. Mizorogi and S. Nagase, *Nat. Chem.* **2**, 112–116 (2010).
- 6) M. Saito, M. Sakaguchi, T. Tajima, K. Ishimura, S. Nagase and M. Hada, *Science* **328**, 339–342 (2010).
- 7) M. Yamada, T. Akasaka and S. Nagase, *Acc. Chem. Res.* **43**, 92–102 (2010).
- 8) X. Gao, J. Jiang and S. Nagase, *J. Phys. Chem. C* **114**, 832–842 (2010).
- 9) X. Gao, L. Liu, S. Irlle and S. Nagase, *Angew. Chem., Int. Ed.* **49**, 3200–3202 (2010).

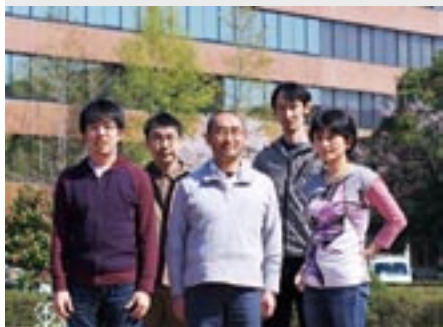
\* Present Address; Department of Physics and Applied Physics, Research Polytechnic Institute, New York 12180, U.S.A.

† Present Address; Department of Physics, University of Nebraska at Omaha, Nebraska 68182-0266, U.S.A.

‡ Present Address; Department of Chemistry, Hiroshima University, Higashi-Hiroshima 739-8526

# Electron and Electromagnetic Field Dynamics in Nanostructures

Department of Theoretical and Computational Molecular Science  
Division of Theoretical Molecular Science I



NOBUSADA, Katsuyuki  
YASUIKE, Tomokazu  
IWASA, Takeshi  
KUBOTA, Yoji  
NODA, Masashi  
YAMADA, Mariko

Associate Professor  
Assistant Professor  
JSPS Post-Doctoral Fellow  
Post-Doctoral Fellow  
Post-Doctoral Fellow  
Secretary

We have developed theoretical methods to calculate photo-induced electron dynamics in nanostructured materials such as nanoparticles, quantum-dot arrays, and adsorbate-surface systems. Specifically, we have developed generalized theory of a light-matter interaction beyond a dipole approximation on the basis of the multipolar Hamiltonian with the aim of understanding the near-field excitation of molecules at the 1 nm scale. Optical forces exerted on a 1 nm-sized metal particle were calculated in the framework of real-time and real-space time-dependent density functional theory combined with the new light-matter interaction formalism. We have also studied exciton-polariton transmission in quantum dot waveguides in an array of quantum dot. Furthermore, collectivity of plasmonic excitations in small sodium clusters was investigated in depth.

## 1. Near-Field Induced Optical Force on a Metal Particle and $C_{60}$ : Real Time and Real Space Electron Dynamics Simulation<sup>1)</sup>

Optical forces induced by a near-field are calculated for a 1 nm-sized metal particle mimicked by a jellium model and for  $C_{60}$  in the framework of real-time and real-space time-dependent density functional theory combined with a non-uniform light-matter interaction formalism, fully taking account of multipole interaction. A highly localized near-field non-uniformly polarizes these molecules. The locally induced polarization charges in the molecules are partly canceled by the screening charges. The polarization and screening charges generally contribute to the attractive and repulsive forces, respectively, and a sensible balance between these charges results in several peaks in the optical force as a function of the frequency of the near-field. The resonance excitation does not necessarily maximally induce the net force and the force exerted on the molecules strongly depends on the details of their electronic structures. The optical force is larger in the metal particle than  $C_{60}$ . We also found that the optical force depends linearly on the intensity of the near-field.

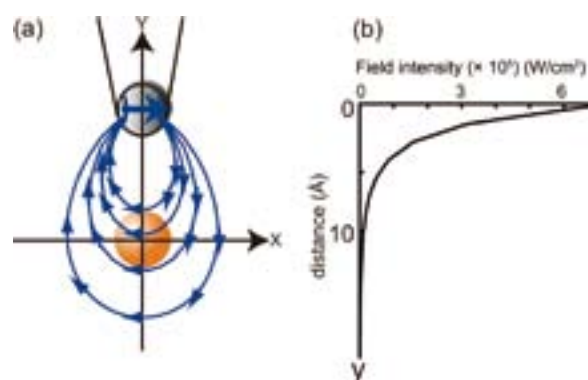


**Figure 1.** (a) Schematic of a near-field fiber tip (gray ball) and a target particle (orange ball). The near-field is approximated by the radiation from an  $x$ -polarized oscillating dipole (solid blue arrow). The blue curves denote the electric field lines. (b) Electric field intensity as a function of distance between the tip and the particle.

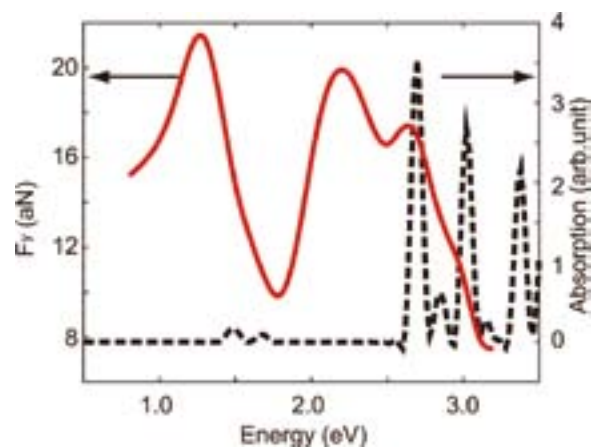


**Figure 2.** Absorption spectrum (dashed-black) of the silver nanoparticle and the time-averaged force on the particle (red) as a function of energy.

## 2. Exciton–Polariton Transmission in Quantum Dot Waveguides and a New Transmission Path due to Thermal Relaxation<sup>2)</sup>

Exciton–polariton transmission in quantum dot waveguides is investigated with quantum time-evolution equations in Liouville space for quantum wave packet dynamics. The transmission efficiency of the exciton–polariton wave with the longitudinal and transverse mode transformation strongly depends on the geometric parameters (bending angle and interdot distance) of the waveguides and on configuration of an additional branch attached to the waveguide. We have numerically demonstrated the transmission efficiency significantly improves by controlling these geometric parameters and the configuration of the branched waveguide. The optimal bending angle for efficient transmission with the longitudinal and transverse mode transformation deviates from the right angle owing to more than nearest-neighbor-site interactions through a shortcut. We have also found that existence of thermal relaxation enables to open a new transmission channel along which the exciton–polariton transmission through the Coulomb interaction is suppressed.

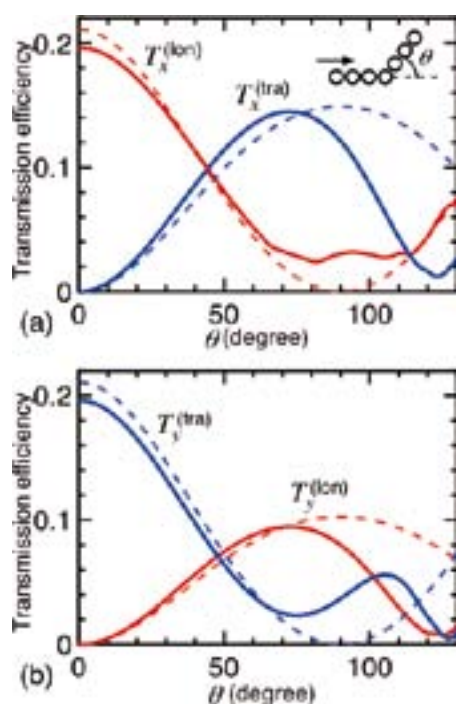


**Figure 3.** Bending angle dependence of transmission efficiency. The solid and dashed curves are the results for the full interaction calculations and for the calculation under the nearest-neighbor interaction approximation, respectively.

## 3. Collectivity of Plasmonic Excitations in Small Sodium Clusters

Plasmonic excitations in small sodium clusters are investi-

gated by using the linear-response density functional theory (LRDFT). The computed photoabsorption spectra show a small number of strong peaks, and the intensities for some of those peaks monotonically grow up with increasing the cluster size. The dipolar character of the transition density distributions for them shows a clear correspondence to a classical picture of plasmonic excitation. The collectivity of the electronic motion induced by the plasmonic excitation is quantitatively analyzed in terms of the collectivity index defined by the transition density matrix. The excitation mode dependence of the collectivity in non-spherical clusters and large collectivities for the higher-energy plasmonic excitations are found. The collectivity analysis also clarifies the existence of the non-dipolar collective motion at the energies very close to the higher-energy plasmonic excitations. The importance of the non-dipolar motion is pointed out in light of nano-optics.

## 4. Isolation, Structure, and Stability of a Dodecanethiolate-Protected Pd<sub>1</sub>Au<sub>24</sub> Cluster<sup>3)</sup>

A dodecanethiolate-protected Pd<sub>1</sub>Au<sub>24</sub>(SC<sub>12</sub>H<sub>25</sub>)<sub>18</sub> cluster, which is a mono-Pd-doped cluster of the well understood magic gold cluster Au<sub>25</sub>(SR)<sub>18</sub>, was isolated in high purity using solvent fractionation and high-performance liquid chromatography (HPLC) after the preparation of dodecanethiolate-protected palladium–gold bimetal clusters. The cluster thus isolated was identified as the neutral [Pd<sub>1</sub>Au<sub>24</sub>(SC<sub>12</sub>H<sub>25</sub>)<sub>18</sub>]<sup>0</sup> from the retention time in reverse phase columns and by elemental analyses. The LDI mass spectrum of [Pd<sub>1</sub>Au<sub>24</sub>(SC<sub>12</sub>H<sub>25</sub>)<sub>18</sub>]<sup>0</sup> indicates that [Pd<sub>1</sub>Au<sub>24</sub>(SC<sub>12</sub>H<sub>25</sub>)<sub>18</sub>]<sup>0</sup> adopts a similar framework structure to Au<sub>25</sub>(SR)<sub>18</sub>, in which an icosahedral Au<sup>13</sup> core is protected by six [–S–Au–S–Au–S–] oligomers. The optical absorption spectrum of [Pd<sub>1</sub>Au<sub>24</sub>(SC<sub>12</sub>H<sub>25</sub>)<sub>18</sub>]<sup>0</sup> exhibits peaks at ~690 and ~620 nm, which is consistent with calculated results on [Pd<sub>1</sub>@Au<sub>24</sub>(SC<sub>1</sub>H<sub>3</sub>)<sub>18</sub>]<sup>0</sup> in which the central gold atom of Au<sub>25</sub>(SC<sub>1</sub>H<sub>3</sub>)<sub>18</sub> is replaced with Pd. These results strongly indicate that the isolated [Pd<sub>1</sub>Au<sub>24</sub>(SC<sub>12</sub>H<sub>25</sub>)<sub>18</sub>]<sup>0</sup> has a core-shell [Pd<sub>1</sub>@Au<sub>24</sub>(SC<sub>12</sub>H<sub>25</sub>)<sub>18</sub>]<sup>0</sup> structure in which the central Pd atom is surrounded by a frame of Au<sub>24</sub>(SC<sub>12</sub>H<sub>25</sub>)<sub>18</sub>. Experiments on the stability of the cluster showed that Pd<sub>1</sub>@Au<sub>24</sub>(SC<sub>12</sub>H<sub>25</sub>)<sub>18</sub> is more stable against degradation in solution and laser dissociation than Au<sub>25</sub>(SC<sub>12</sub>H<sub>25</sub>)<sub>18</sub>. These results indicate that the doping of a central atom is a powerful method to increase the stability beyond the Au<sub>25</sub>(SR)<sub>18</sub> cluster.

## References

- 1) T. Iwasa and K. Nobusada, *Phys. Rev. A* **80**, 043409 (11 pages) (2009).
- 2) Y. Kubota and K. Nobusada, *J. Phys. Soc. Jpn.* **78**, 114603 (7 pages) (2009).
- 3) Y. Negishi, W. Kurashige, Y. Niihori, T. Iwasa and K. Nobusada, *Phys. Chem. Chem. Phys.* **12**, 6219–6225 (2010).

# Advanced Electronic Structure Theory in Quantum Chemistry

Department of Theoretical and Computational Molecular Science  
Division of Theoretical Molecular Science I



YANAI, Takeshi  
KURASHIGE, Yuki  
MIZUKAMI, Wataru  
YAMADA, Mariko

Associate Professor  
Assistant Professor  
Graduate Student  
Secretary

Aiming at predictive computational modelings of molecular electronic structures with *ab initio* quantum chemistry calculations, our scientific exploration is to establish a cutting-edge theoretical methodology that allows one to compute accurately and efficiently the complex electronic structures, in which strongly-interacting electrons play a crucial role to characterize the nature of molecules. The complicated electronic structures can be handled accurately with the multi-reference theory, which deals with multiple important electronic configurations on equal footing. However, with the standard multireference methods such as the complete active space self-consistent field (CASSCF), the tractable size of the reference space is limited to small active space because the complexity of the calculations grows exponentially with the reference size. The existing multireference methods are nevertheless usefully applied to chemical theory problems such as exploring chemical reactions of bonding, dissociation and isomerization along the reaction coordinates, electronically excited states, unstable electronic structures of radical systems, and multiple covalent bindings in molecular metal complexes, *etc.* Our resultant works to be reported here are (1) to develop a type of the multireference correlation model named Canonical Transformation (CT) theory, which can efficiently describe short-range dynamic correlation on top of the multi-configurational starting wave function, and (2) to construct the extensive complete active space self-consistent field (CASSCF) method combined with *ab initio* density matrix renormalization group (DMRG) method for making unprecedentedly larger active spaces available for the CASSCF calculations.

## 1. Discovery of New Quantum States of Electron Spins in Polycarbenes from *Ab Initio* Density Matrix Renormalization Group Calculations<sup>1)</sup>

An investigation into spin structures of poly(*m*-phenylene-carbene)s, a prototype of organic magnetic molecules, is presented using the *ab initio* density matrix renormalization group method. It is revealed by achieving large-scale multi-

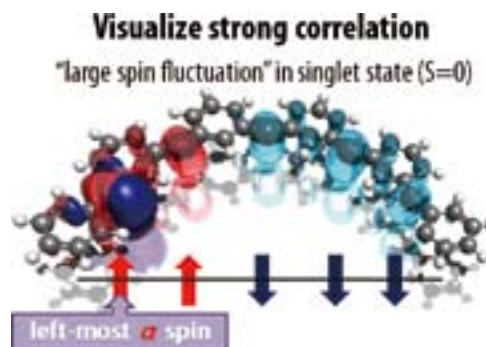


**Figure 1.** The spin correlation densities  $\sigma_i^{\text{spin}}(r)$  of the CASSCF wave functions with respect to the non-bonding  $sp^2$  orbital on the leftmost carbene site of polycarbene with  $n = 5$  (solid red and blue color) for the singlet state. Crystal red and blue represent  $\alpha$  spin ( $\sigma_i^{\text{spin}}(r) > 0$ ) and  $\beta$  spin ( $\sigma_i^{\text{spin}}(r) < 0$ ), respectively. The density visualizes the spin correlation against the  $\alpha$  spin at the nonbonding orbital at the leftmost carbene site. The orbital and molecular geometry is superimposed.

reference calculations that the energy differences between high-spin and low-spin states (spin-gaps) of polycarbenes decrease with increasing the number of carbene sites. This size-dependency of the spin-gaps strikingly contradicts the predictions with single-reference methods including density functional theory. The wave function analysis shows that the low-spin states are beyond the *classical* spin picture, namely, much of multireference character, and thus are manifested as strongly correlated *quantum* states. The size dependence of the spin-gaps involves an odd-even oscillation, which cannot be explained by the model Hamiltonians with a single magnetic-coupling constant (**Figure 1**).

## 2. Multireference Quantum Chemistry through a Joint Density Matrix Renormalization Group and Canonical Transformation Theory<sup>2-4)</sup>

We presented the joint application of the density matrix

renormalisation group and canonical transformation theory to multireference quantum chemistry. The density matrix renormalization group provides the ability to describe static correlation in large active spaces, while the canonical transformation theory provides a high-order description of the dynamic correlation effects. We demonstrate the joint theory in two benchmark systems designed to test the dynamic and static correlation capabilities of the methods, namely (i) total correlation energies in long polyenes, and (ii) the isomerisation curve of the  $[\text{Cu}_2\text{O}_2]^{2+}$  core. The largest complete active spaces treated by the joint DMRG-CT theory in these systems correspond to a (24e,24o) active space in the polyenes and a (28e,32o) active space in  $[\text{Cu}_2\text{O}_2]^{2+}$ .

### 3. *Ab Initio* Study of the Excited Singlet States of All-*trans* $\alpha,\omega$ -Diphenylpolyenes with One to Seven Polyene Double Bonds: Simulation of the Spectral Data within Franck–Condon Approximation<sup>5)</sup>

Computational simulations of the electronic spectra with *ab initio* electronic structure calculations are presented for all-*trans*  $\alpha,\omega$ -diphenylpolyenes with the polyene double bond number ( $N$ ) from one to seven. A direct comparison of the fluorescence spectra of diphenylpolyenes was made between the results of highly accurate calculations and the experimental data for the systems with various chain lengths. For the realistic simulation of the emission, the total vibrational wave function was described approximately as a direct product of one-dimensional (1D) vibrational wave functions along the normal coordinates that are determined from the vibrational analysis of the ground state. The observed spectra can be reproduced in a computationally efficient way by selecting effective C–C and C=C stretching modes for the constructions of the 1D vibrational Hamiltonians. The electronic structure

calculations were performed using the multireference Møller–Plesset perturbation theory with complete active space configuration interaction reference functions (CASCI-MRMP). Based on the vertical excitation energies computed, the lowest singlet excited state of diphenylbutadiene is shown to be the optically forbidden  $2^1\text{A}_g$  state. The simulations of fluorescence spectra involving vibronic coupling effects reveal that the observed strong single C=C band consists of two major degenerate vibrational C=C modes for the shorter diphenylpolyenes with  $N = 3$  and 5. Further, the relative intensities of the C–C stretching modes in the fluorescence spectra tend to be larger than those of the C=C stretching modes for the systems with  $N$  over 5. This indicates that the geometric differences of the energy minima between the ground ( $1^1\text{A}_g$ ) and  $2^1\text{A}_g$  states grows larger towards the direction of the C–C stretching mode with increasing  $N$  (Figure 2).

### 4. Tensor Factorizations of Local Second-Order Møller–Plesset Theory<sup>6)</sup>

Efficient electronic structure methods require efficient tensor representations of the wavefunction. Here we describe a general way to view tensor factorization. We use these ideas to construct low-complexity representations of the doubles amplitudes in local second order Møller–Plesset perturbation theory. We introduce two approximations—the direct factorized virtual approximation and the complete factorized virtual approximation. Conceptually, these lie between the projected atomic orbital representation used in the Pulay-Saebo local correlation theories and pair natural orbital correlation theories. We have tested the factorized virtual approximations on a variety of systems and properties including total energies, reaction energies, and potential energy curves. Compared to the Pulay-Saebo ansatz, we find that these approximations exhibit favourable accuracy and computational timings, while yielding smooth potential energy curves.

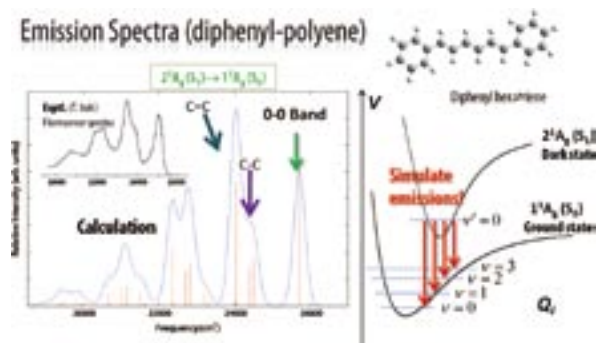


**Figure 2.** Simulated fluorescence spectrum of the vibronic transitions  $2\text{A}_g \rightarrow 1\text{A}_g$  of all-*trans*  $\alpha,\omega$ -diphenylhexatriene (DP3) with  $N = 3$  ( $N$  is the number of double bond in the polyene chain). Inset: The observed spectrum measured by T. Itoh (the Joint Studies Program (2008–2009) of the Institute for Molecular Science).

### References

- 1) W. Mizukami, Y. Kurashige and T. Yanai, *J. Chem. Phys.* in press.
- 2) T. Yanai, Y. Kurashige, E. Neuscamman and G. K.-L. Chan, *J. Chem. Phys.* **132**, 024105 (9 pages) (2010).
- 3) E. Neuscamman, T. Yanai and G. K.-L. Chan, *J. Chem. Phys.* **132**, 024106 (13 pages) (2010).
- 4) E. Neuscamman, T. Yanai and G. K.-L. Chan, *Int. Rev. Phys. Chem.* **29**, 231 (2010).
- 5) W. Mizukami, Y. Kurashige, M. Ehara, T. Yanai and T. Itoh, *J. Chem. Phys.* **131**, 174313 (10 pages) (2009).
- 6) J. Yang, Y. Kurashige, F. R. Manby and G. K.-L. Chan, *J. Chem. Phys.*, submitted.

### Award

MIZUKAMI, Wataru; 2009 The Best Poster Award at the 3<sup>rd</sup> annual meeting of Japan Society for Molecular Science.

# Developing the Statistical Mechanics Theory of Liquids in Chemistry and Biophysics

Department of Theoretical and Computational Molecular Science  
Division of Theoretical Molecular Science II



HIRATA, Fumio	Professor
CHONG, Song-ho	Assistant Professor
YOSHIDA, Norio	Assistant Professor
MARUYAMA, Yutaka	Post-Doctoral Fellow
MIYATA, Tatsuhiko	Post-Doctoral Fellow
PHONGPHANPHANEE, Saree	Post-Doctoral Fellow
SINDHIKARA, Daniel	Post-Doctoral Fellow
KIYOTA, Yasuomi	Graduate Student
SUETAKE, Yasumi	Secretary
KONDO, Naoko	Secretary
YAMADA, Mariko	Secretary

“Molecular recognition” is an essential elementary process for protein to function. The process is a thermodynamic process which is characterized with the free energy difference between two states of a host-guest system, namely, associated and dissociated states. It is readily understood that the structural fluctuation of protein gives a big effect on the free energy barrier. In that respect, the “molecular recognition” is a thermodynamic process which is conjugated with the structural fluctuation of protein.

We have been developing a new theory concerning the molecular recognition, based on the 3D-RISM/RISM theory which is a statistical mechanics of liquids. The theory has successfully “probed” small ligands such as water molecules and ions bound in a small cavity of protein.<sup>1-3)</sup>

## 1. Ligand Mapping on Protein Surfaces by the 3D-RISM Theory: Toward Computational Fragment-Based Drug Design<sup>4)</sup>

In line with the recent development of fragment-based drug design, a novel computational method for mapping of small ligand molecules onto protein surface is proposed in this paper. The method uses the three-dimensional (3D) spatial distribution functions of the atomic sites of ligand calculated by a molecular theory of solvation, known as the 3D reference interaction site model (3D-RISM) theory, to identify the most probable binding modes of the ligand molecule. In this study, the 3D-RISM-based method is applied to the binding of several small organic solvents to thermolysin, in order to evaluate its efficiency. The results demonstrate that our method can reproduce the major binding modes found by X-ray crystallography with sufficient accuracy. Moreover, it is found that the method can successfully identify some binding modes associated with a known inhibitor, which could not be detected by the experiment. The dependence of ligand-binding modes on the ligand concentration, which can hardly be treated with other existing methods, is also investigated. The results indicate that some binding modes are readily affected by a shift in

the ligand concentration, while the others are not substantially altered. An analysis of the water distribution implies that the ligand-binding modes are determined by a subtle balance in the binding affinity between ligand and water.

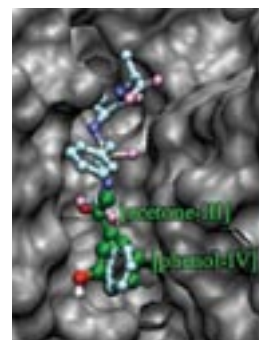


**Figure 1.** Comparison of two binding modes identified using 3D-RISM with the crystallographic structure in active site.

## 2. Molecular Selectivity in Aquaporin Channels Studied by the 3D-RISM Theory<sup>5)</sup>

The three dimensional distribution function (3D-DF) and potential of means force (PMF) of small neutral molecules inside the two aquaporin channels, AQP1 and GlpF, are calculated based on the 3D-RISM theory, the statistical mechanics theory of molecular liquids, in order to investigate the permeability of those ligands through the channels. The ligands investigated are Neon (Ne), carbon dioxide (CO<sub>2</sub>), Nitrogen oxide (NO), ammonia (NH<sub>3</sub>), urea, and glycerol.

Neon showed continuous distribution through out the channel pore in AQP1 as is the case of water, although the PMF of Ne at the selective filter (SF) region is higher than that of water, indicating that the stability of molecules in the channel is determined not only by their size, but also by the charge distribution. The ligand molecules, CO<sub>2</sub>, NO, urea, and glycerol have large barrier in PMF at the SF region in AQP1, indicating that those ligands are not permeable through the



channel. On the other hand,  $\text{NH}_3$  has only small activation barrier,  $\sim 2.5$  kJ/mol, to be overcome. Therefore, our theory predicts that a  $\text{NH}_3$  molecule can be permeated through the AQP1 channel. In GlpF, all the ligands have negative PMF throughout the channel except for glycerol which has a small barrier at the SF area,  $\sim 2.1$  kJ/mol. The barrier can be readily overcome by the thermal motion. So, our results are quite consistent with the experiments for urea and glycerol, for which the corresponding data are available.

The potential of mean forces of the ligand molecules in GlpF obtained from the MD simulations show distinctly different patterns from our results: PMFs of  $\text{NH}_3$  and urea from MD have large positive values throughout the channel, while those of  $\text{CO}_2$  and glycerol has some negative regions. In any case, the barriers in PMF at the SF region are so high and large for all the four ligands examined. It seems impossible for them to overcome the barrier in order to be permeated through the channel. This raises a serious question to the results from MD simulations, because the experimental observation indicates that GlpF can conduct glycerol and urea pretty well. (Actually, the name “glyceroporin,” came from that function of the channel.)

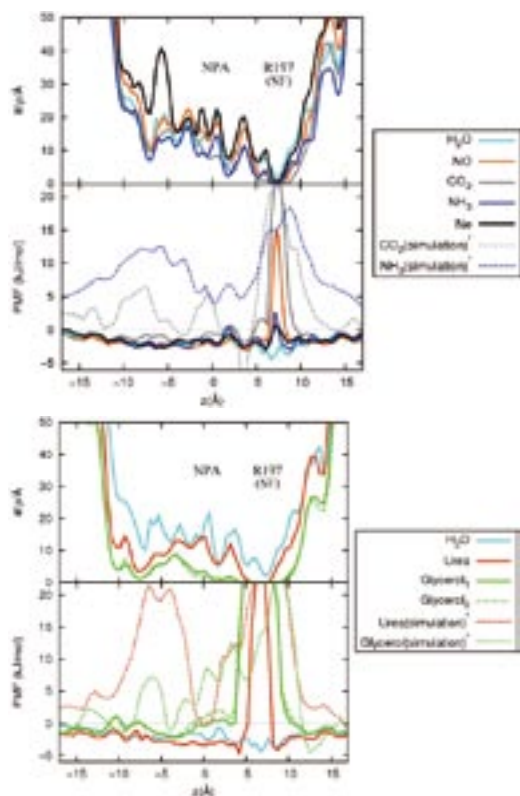


Figure 2. PMFs of water, Ne,  $\text{CO}_2$ ,  $\text{NH}_3$ , urea and glycerol in AQP1.

### 3. Proton Transport through the Influenza A M2 Channel: 3D-RISM Study<sup>6)</sup>

The three dimensional distribution and the potential of mean force of water and hydronium ions in five protonated states of the Influenza A M2 channel are calculated by means

of the 3D-RISM theory in order to clarify the proton conduction mechanism of the channel. Each protonated state denoted as  $i\text{H}$ , where  $i$  runs from 0 to 4, has a different number of protonated histidines from 0 to 4. The distribution of water in each state exhibits closed structure of  $0\text{H}$ ,  $1\text{H}$  and  $2\text{H}$ , and opened structure in  $3\text{H}$  and  $4\text{H}$ . In the closed form, the distribution function and potential of mean forces calculated by the 3D-RISM theory indicate that hydronium ions are excluded from the channel. In contrast, the ion can distribute throughout the opened channel. The barrier in potential of mean force of  $3\text{H}$ ,  $\sim 3$ – $5$  kJ/mol, is lower than that of  $4\text{H}$ ,  $5$ – $7$  kJ/mol, indicating that  $3\text{H}$  has higher permeability to proton. Based on the radial distribution functions of water and hydronium ions around the imidazole rings of His37, we propose a new mechanism of proton transfer through the gating region of the channel. In this process, a hydronium ion hands a proton to a non-protonated histidine through a hydrogen-bond between them, and then the other protonated histidine releases a proton to a water molecule via a hydrogen-bond. The process transfers a proton effectively from a water molecule to the other.

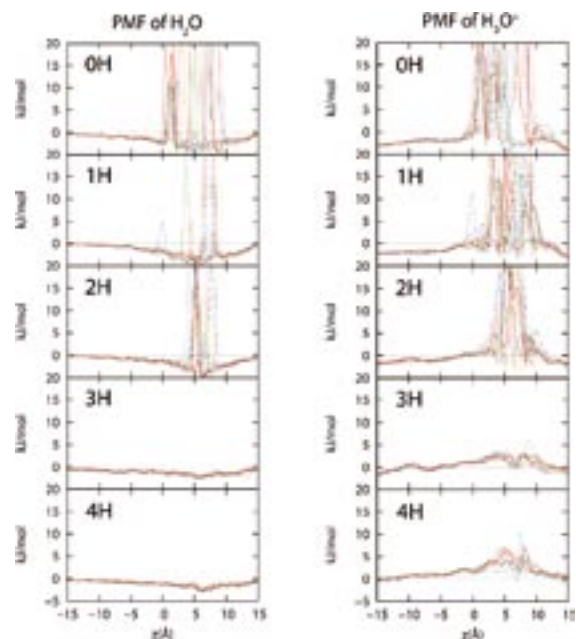


Figure 3. Potential of Mean force of water and hydronium ion in each state, a line represents the PMF for a conformation in the state.

#### References

- 1) F. Hirata, *Molecular Theory of Solvation*, Kluwer; Dordrecht, Netherlands (2003).
- 2) A. Kovalenko and F. Hirata, *J. Chem. Phys.* **110**, 10095–10112 (1999).
- 3) T. Imai, R. Hiraoka, A. Kovalenko and F. Hirata, *J. Am. Chem. Soc. (Communication)* **127**, 15334–15335 (2005).
- 4) T. Imai, K. Oda, A. Kovalenko, F. Hirata and A. Kidera, *J. Am. Chem. Soc.* **131**, 12430 (2009).
- 5) S. Phongphananee, N. Yoshida and F. Hirata, *J. Phys. Chem. B* **114**, 7967 (2010).
- 6) S. Phongphananee, T. Rungromongkol, N. Yoshida, S. Hannongbua and F. Hirata, *J. Am. Chem. Soc.* **132**, 9782 (2010).

# Theory of Photoinduced Phase Transitions

Department of Theoretical and Computational Molecular Science  
Division of Theoretical Molecular Science II



YONEMITSU, Kenji  
TANAKA, Yasuhiro  
KONDO, Naoko

Associate Professor  
Assistant Professor  
Secretary

Photoirradiation of materials usually creates electrons and holes, which are often accompanied by local structural deformation. With the help of cooperativity, the electronic and/or structural deformation can proliferate to change the physical property such as conductivity, permittivity, and magnetic susceptibility. The resultant nonequilibrium phase may not be reached by changing temperature or pressure because the energy of a photon is much higher than thermal energies. Our theoretical researches are focused on the mechanisms and dynamics of photoinduced phase transitions, how they are controlled, and how the photoinduced electron-lattice states are different from those which are realized in thermal equilibrium.<sup>1)</sup>

## 1. Growth Dynamics of Photoinduced Domains in Charge-Ordered Conductors<sup>2,3)</sup>

We focus on quasi-two-dimensional quarter-filled-band charge-ordered insulators,  $\theta$ -(BEDT-TTF)<sub>2</sub>RbZn(SCN)<sub>4</sub> and  $\alpha$ -(BEDT-TTF)<sub>2</sub>I<sub>3</sub>, where quite different photoinduced melting dynamics are observed. To elucidate such dynamics of initially quite similar, “horizontal-stripe” charge orders, we theoretically study photoinduced evolution of the wave functions in extended Peierls-Hubbard models on anisotropic triangular lattices. The exact many-electron wave function coupled with classical phonons is used for 12-site systems, and the unrestricted Hartree-Fock approximation is used for 144-site systems. These charge orders are stabilized by both Coulomb repulsion and electron-lattice interactions. Their relative importance is different between the two materials.

In  $\theta$ -(BEDT-TTF)<sub>2</sub>RbZn(SCN)<sub>4</sub>, the high-temperature metallic phase has a crystal structure with a high symmetry so that different charge-order patterns are nearly degenerate. At low temperatures, a relatively large lattice distortion emerges as molecular rotations (Figure 1, left panel), lifting the degeneracy among these patterns. The lattice stabilization energy is

consequently large, so that a high photoexcitation density is required for the melting. Because each hole-rich stripe is stabilized by uniform molecular rotation, a photoinduced metallic domain created by local photoexcitation grows in a quite anisotropic manner (Figure 2, left panel). The photoinduced charge dynamics shows a complex behavior owing to a large number of nearly degenerate eigenstates.

In  $\alpha$ -(BEDT-TTF)<sub>2</sub>I<sub>3</sub>, the high-temperature metallic phase has a crystal structure with a low symmetry so that charge disproportionation already takes place from kinetic origin. At low temperatures, a small lattice distortion (Figure 1, right panel) is sufficient to stabilize the charge order. The lattice stabilization energy is small, and a low photoexcitation density is sufficient to melt the charge order, producing a metallic phase. Because each hole-rich bond is locally stabilized, a photoinduced metallic domain created by local photoexcitation grows isotropically (Figure 2, right panel), *i.e.*, in any direction of the conducting layer. Thus, a very large metallic domain is finally photogenerated. The photoinduced charge dynamics shows a coherent oscillation when resonantly excited.

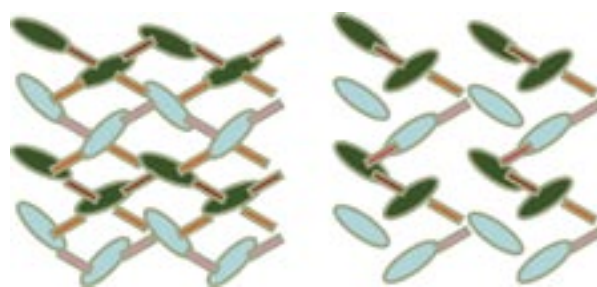


**Figure 1.** Schematic molecular arrangements in  $\theta$ -(BEDT-TTF)<sub>2</sub>RbZn(SCN)<sub>4</sub> (left) and  $\alpha$ -(BEDT-TTF)<sub>2</sub>I<sub>3</sub> (right). The ellipses with dark and bright colors represent hole-rich and hole-poor molecules, respectively. Note the angles of ellipses. The rectangles with dark, intermediate, and bright colors correspond to large, intermediate, and small transfer integrals, respectively.

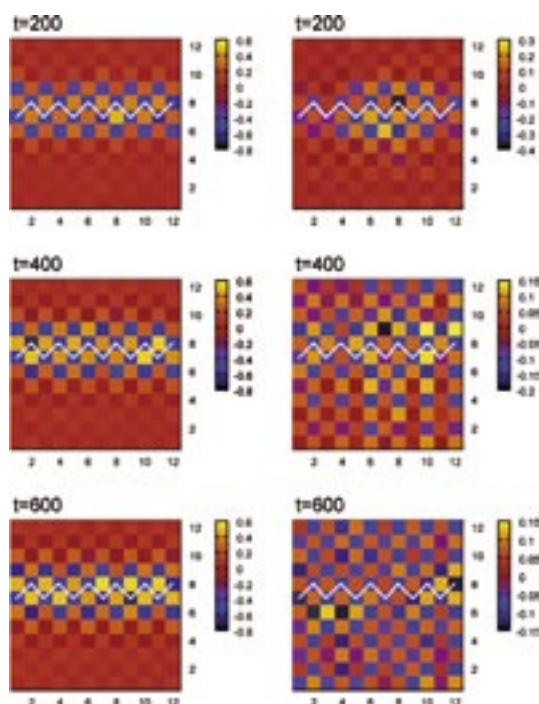


**Figure 2.** Charge densities at different times, from which those before photoexcitation are subtracted.<sup>2)</sup> The left and right panels show  $\theta$ -(BEDT-TTF)<sub>2</sub>RbZn(SCN)<sub>4</sub> and  $\alpha$ -(BEDT-TTF)<sub>2</sub>I<sub>3</sub>, respectively. The squares indicate molecules, and the white lines hole-rich stripes.

## 2. Quantum Electron–Vibration Interference in Photoinduced Insulator–Metal Transition

As described above, a photoinduced insulator-to-metal transition is realized in  $\alpha$ -(BEDT-TTF)<sub>2</sub>I<sub>3</sub>. In reality, the transition is achieved in two stages: An ultrafast one consisting of mainly electronic processes and a slow one consisting of domain processes responsible for the critical slowing down. Although the latter stage can be described in principle by statistical mechanics, the former stage directly reflects interactions among electrons and interactions between electrons and phonons. The latest experimental technique allows us to observe such early-stage dynamics.

Here, it is important to consider electron–molecular-vibration (EMV) couplings. Charge transfers between neighboring molecules are governed by intermolecular transfer integrals. Their magnitudes are about 0.1 or 0.2 eV. The energy range of C=C stretching vibrations inside a molecule is also 0.1 to 0.2 eV. Thus, they can interfere with each other (Figure 3). Then, we theoretically study photoinduced evolution of the wave function in an extended Holstein–Peierls–Hubbard model. The exact many-electron–phonon (molecular vibration) wave function coupled with classical lattice phonons is used for 8-site systems.

Photoexcitation directly oscillates an electron back and forth between neighboring molecules. It excites a molecular

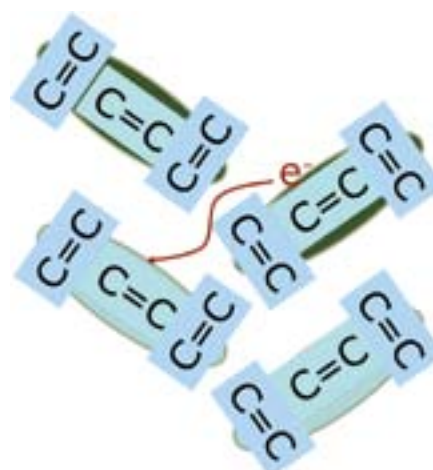


**Figure 3.** Schematic illustration of electron–molecular-vibration coupling.

vibration through the EMV coupling. They are initially in phase. Soon, their motions become out of phase, causing destructive quantum interference (Figure 4, 50 to 100 fs).

After that, the electronic motion is synchronized with the slower motion of molecular vibrations (Figure 4, after 100 fs) and finally dephased. In reality, there are several modes of molecular vibrations with different energies and coupling strengths. However, the quantum interference obtained above qualitatively simulates the experimentally observed, early-stage dynamics.

From this analysis, the EMV coupling turns out to stabilize the charge order as well as the intersite Coulomb repulsion. The relative importance of molecular vibrations and lattice phonons depends on the timescale of observation. The former is important at the early stage, while the latter is important at the later stage.

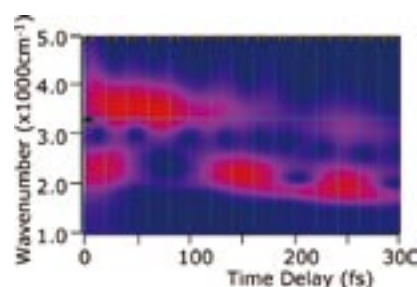


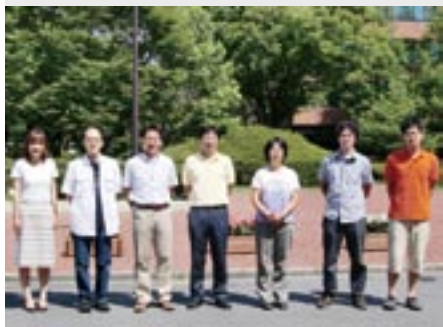
**Figure 4.** Wavelet transform of photoinduced charge-density modulation.

## References

- 1) K. Yonemitsu and K. Nasu, *Phys. Rep.* **465**, 1–60 (2008).
- 2) Y. Tanaka and K. Yonemitsu, *J. Phys. Soc. Jpn.* **79**, 024712 (8 pages) (2010).
- 3) S. Miyashita, Y. Tanaka, S. Iwai and K. Yonemitsu, *J. Phys. Soc. Jpn.* **79**, 034708 (9 pages) (2010).

# Theoretical Studies on Condensed Phase Dynamics

Department of Theoretical and Computational Molecular Science  
Division of Computational Molecular Science



SAITO, Shinji	Professor
KIM, Kang	Assistant Professor
HIGASHI, Masahiro	IMS Fellow
KOBAYASHI, Chigusa	Post-Doctoral Fellow
YAGASAKI, Takuma	Post-Doctoral Fellow
IMOTO, Sho	Graduate Student*
UENO, Harumi	Secretary

Liquids and biological systems show complicated dynamics because of their structural flexibility and dynamical hierarchy. Understanding these complicated dynamics is indispensable to elucidate chemical reactions and relaxation in solutions and functions of proteins. We have been investigating complex dynamics in supercooled liquids<sup>1-3)</sup> and chemical reactions in biological systems<sup>4)</sup> using molecular dynamics simulations and electronic structure calculations. In addition, we have been theoretically investigating liquid dynamics by using higher-order nonlinear IR spectroscopy.<sup>5,6)</sup>

## 1. Multi-Time Density Correlation Functions in Glass-Forming Liquids: Probing Dynamical Heterogeneity and Its Lifetime<sup>1)</sup>

A multi-time extension of a density correlation function is introduced to reveal temporal information about dynamical heterogeneity in glass-forming liquids. We utilize a multi-time correlation function that is analogous to the higher-order response function analyzed in multidimensional nonlinear spectroscopy. Here, we provide comprehensive numerical results of the four-point, three-time density correlation function from longtime trajectories generated by molecular dynamics simulations of glass-forming binary soft-sphere mixtures. We confirm that the two-dimensional representations in both time and frequency domains are sensitive to the dynamical heterogeneity and that these reveal the couplings of correlated motions, which exist over a wide range of time scales. The correlated motions detected by the three-time correlation function are divided into mobile and immobile contributions that are determined from the particle displacement during the first time interval. We show that the peak positions of the correlations are in accord with the information on the non-Gaussian parameters of the van Hove self-correlation function. Furthermore, it is demonstrated that the progressive changes in

the second time interval in the three-time correlation function enable us to analyze how correlations in dynamics evolve in time. From this analysis, we evaluated the lifetime of the dynamical heterogeneity and its temperature dependence systematically. Our results show that the lifetime of the dynamical heterogeneity becomes much slower than the  $\alpha$ -relaxation time that is determined from the two-point density correlation function when the system is highly supercooled.

## 2. Slow Dynamics in Random Media: Crossover from Glass to Localization Transition<sup>2)</sup>

We study slow dynamics of particles moving in a matrix of immobile obstacles using molecular-dynamics simulations. The glass transition point decreases drastically as the obstacle density increases. At higher obstacle densities, the dynamics of mobile particles changes qualitatively from glass-like to a Lorentz-gas-like relaxation. This crossover is studied by density correlation functions, nonergodic parameters, mean square displacement, and nonlinear dynamic susceptibility. Our finding is qualitatively consistent with the results of recent numerical and theoretical studies on various spatially heterogeneous systems. Furthermore, we show that slow dynamics is surprisingly rich and sensitive to obstacle configurations. Especially, the reentrant transition is observed for a particular configuration, although its origin is not directly linked to the similar prediction based on the mode-coupling theory.

## 3. Relation between Conformational Heterogeneity and Reaction Cycle of Ras: Molecular Simulation of Ras<sup>4)</sup>

Ras functions as a molecular switch by cycling between the active GTP-bound state and the inactive GDP-bound state.

It is known experimentally that there is another GTP-bound state called state 1. We investigate the conformational changes and fluctuations arising from the difference in the coordinations between the switch regions and ligands in the GTP- and GDP-bound states by using 830 ns molecular dynamics simulations in total. The present result suggests that the large fluctuations among multiple conformations of switch I in state 1 owing to the absence of the coordination between Thr-35 and  $Mg^{2+}$  inhibit the binding of Ras to effectors. Furthermore, we elucidate the conformational heterogeneity in Ras by using principal component analysis and propose a two-step reaction path from the GDP-bound state to the active GTP-bound state *via* state 1. The present study suggests that state 1 plays an important role in the signal transduction as an intermediate state of the nucleotide exchange process, though state 1 itself is an inactive state for signal transduction.

#### 4. Molecular Dynamics Simulation of Nonlinear Spectroscopies of Intermolecular Motions in Liquid Water<sup>5)</sup>

Water is the most extensively studied of liquids because of both its ubiquity and its anomalous thermodynamic and dynamic properties. The properties of water are dominated by hydrogen bonds and hydrogen bond network rearrangements. Fundamental information on the dynamics of liquid water has been provided by linear infrared (IR), Raman, and neutron-scattering experiments; molecular dynamics simulations have also provided insights. Recently developed higher-order nonlinear spectroscopies open new windows into the study of the hydrogen bond dynamics of liquid water. For example, the vibrational lifetimes of stretches and a bend, intramolecular features of water dynamics, can be accurately measured and are found to be on the femtosecond time scale at room temperature. Higher-order nonlinear spectroscopy is expressed by a multi-time correlation function, whereas traditional linear spectroscopy is given by a one-time correlation function. Thus, nonlinear spectroscopy yields more detailed information on the dynamics of condensed media than linear spectroscopy. In this Account, we describe the theoretical background and methods for calculating higher-order nonlinear spectroscopy; equilibrium and non-equilibrium molecular dynamics simulations, and a combination of both, are used. We also present the intermolecular dynamics of liquid water revealed by fifth-order two-dimensional (2D) Raman spectroscopy and third order IR spectroscopy. 2D Raman spectroscopy is sensitive to couplings between modes; the calculated 2D Raman signal of liquid water shows large anharmonicity in the translational motion and strong coupling between the translational and librational motions. Third-order IR spectroscopy makes it

possible to examine the time-dependent couplings. The 2D IR spectra and three-pulse photon echo peak shift show the fast frequency modulation of the librational motion. A significant effect of the translational motion on the fast frequency modulation of the librational motion is elucidated by introducing the “translation-free” molecular dynamics simulation. The isotropic pump–probe signal and the polarization anisotropy decay show fast transfer of the librational energy to the surrounding water molecules, followed by relaxation to the hot ground state.

#### 5. Ultrafast Energy Relaxation and Anisotropy Decay of the Librational Motion in Liquid Water: A Molecular Dynamics Study<sup>6)</sup>

We theoretically investigate intermolecular motions in liquid water in terms of third-order IR spectroscopy. We calculate two-dimensional infrared (2D IR) spectra, pump–probe signals and three-pulse stimulated photon echo signals from the combination of equilibrium and nonequilibrium molecular dynamics simulations. The 2D IR spectra and the three-pulse photon echo peak shift exhibit that the frequency correlation of the librational motion decays with a time scale of 100 fs. The two-color 2D IR spectra and the pump–probe signals reveal that the energy transfer from the librational motion at  $700\text{ cm}^{-1}$  to the low frequency motion below  $300\text{ cm}^{-1}$  occurs with a time scale of 60 fs and the subsequent relaxation to the hot ground state takes place on a 500 fs time scale. The time scale of the anisotropy decay of the librational motion is found to be  $\sim 115$  fs. The energy dissipation processes are investigated in detail by using the nonequilibrium molecular dynamics simulation in which an electric field pulse is applied. We show that the fast energy transfer from the librational motion to the low frequency motion is mainly due to the librational-librational energy transfer. We also show that the fast anisotropy decay mainly arises from the rapid intermolecular energy transfer.

#### References

- 1) K. Kim and S. Saito, *J. Chem. Phys.* **133**, 044511 (10 pages) (2010).
- 2) K. Kim, K. Miyazaki and S. Saito, *Europhys. Lett.* **88**, 36002 (5 pages) (2010).
- 3) K. Kim and S. Saito, *J. Phys. Soc. Jpn.* **79**, 093601 (4 pages) (2010).
- 4) C. Kobayashi and S. Saito, *Biophys. J.* **99**, 3726–3734 (2010).
- 5) T. Yagasaki and S. Saito, *Acc. Chem. Res.* **42**, 1250–1258 (2009).
- 6) T. Yagasaki, J. Ono and S. Saito, *J. Chem. Phys.* **131**, 164511 (11 pages) (2009).

\* carrying out graduate research on Cooperative Education Program of IMS with Nagoya University

# Theoretical Study on Molecular Excited States and Chemical Reactions

Department of Theoretical and Computational Molecular Science  
Division of Computational Molecular Science



EHARA, Masahiro  
FUKUDA, Ryoichi  
TASHIRO, Motomichi  
SURAMITR, Songwut  
LU, Yun-peng  
HORIKAWA, Takenori  
KAWAGUCHI, Ritsuko

Professor  
Assistant Professor  
IMS Research Assistant Professor  
Visiting Scientist  
Visiting Scientist  
Graduate Student  
Secretary

Molecules in the excited states show characteristic photo-physical properties and reactivity. We investigate the molecular excited states and chemical reactions which are relevant in chemistry, physics, and chemical biology with developing the highly accurate electronic structure theory. We are also interested in the excited-state dynamics and energy relaxation so that we also develop the methodology of large-scale quantum dynamics. In this report, we report our recent studies on the development of the PCM-SAC-CI method,<sup>1)</sup> Molecular double core-hole spectroscopy,<sup>2)</sup> and Ultraviolet B blocking molecule.<sup>3)</sup>

## 1. Development of PCM-SAC-CI Method for Solvation Free Energy and Geometry<sup>1)</sup>

Electronic excitations of molecules and molecular systems in particular circumstances, such as in solutions, have attracted attention for a long time. Solvatochromism, the shift of transition energies by a solvent, is an important consideration in such research. Photochemical and electrochemical reactions in solution are other considerations. Reliable computational studies are essential for elucidating the mechanism of such complex processes because it is difficult to detect short-lived intermediate states in certain solvents experimentally. There is a strong demand for the development of theoretical and computational methods to understand photochemical and electrochemical phenomena in solution, such as those associated with utilizing photo-energy with functional dyes, organic photovoltaic cells, charge transport in batteries and molecular devices, *etc.*

In this work we present the theory and implementation of the symmetry-adapted cluster (SAC) and symmetry-adapted cluster-configuration interaction (SAC-CI) method, including the solvent effect, using the polarizable continuum model (PCM). The PCM and SAC/SAC-CI were consistently combined in terms of the energy functional formalism. The excitation energies were calculated by means of the state-specific approach, the advantage of which over the linear-response approach has been shown. The single point energy calculation and its analytical energy derivatives are presented and imple-

mented, where the free energy and its derivatives are evaluated because of the presence of solute-solvent interactions. We have applied this method to *s-trans* acrolein and methylenecyclopropene of their electronic excitation in solution. The molecular geometries in the ground and excited states were optimized in vacuum and in solution, and both the vertical and adiabatic excitations were studied. The PCM-SAC/SAC-CI reproduced the known trend of the solvent effect on the vertical excitation energies but the shift values were underestimated. The excited state geometry in planar and nonplanar conformations was investigated. The importance of using state-specific methods was shown for the solvent effect on the optimized geometry in the excited state. The mechanism of the solvent effect is discussed in terms of the Mulliken charges and electronic dipole moment.

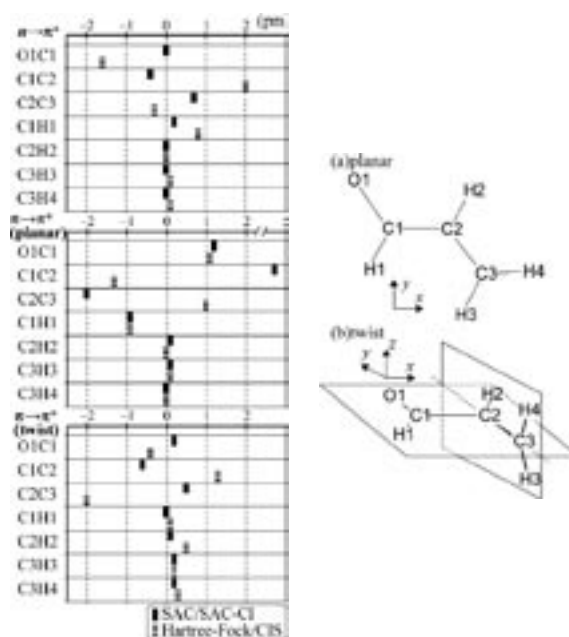


**Figure 1.** Solvent effect on the changes of bond lengths (in pm) upon electronic excitations for *s-trans* acrolein. The solvent effect denotes the shift in aqueous solution from vacuum.

## 2. Molecular Double Core-Hole Spectroscopy for Chemical Analysis<sup>2)</sup>

More than two decades ago, Cederbaum *et al.* discovered that the creation of double core vacancies in molecular systems probes the chemical environment more sensitively than the creation of single core vacancies. Two-atomic site double ionization potentials, or briefly two-site DIPs are particularly sensitive to the chemical environment as the examples of the  $C_2H_2$ ,  $C_2H_4$ ,  $C_2H_6$  and  $C_6H_6$  molecules demonstrate. The chemical shifts of one-atomic site DIPs, or briefly one-site DIPs, were found to be similar to the chemical shifts of the single core level ionization potentials (IPs), or ionization energies (IEs). This finding has given impetus to a number of theoretical studies aimed at elucidating properties of molecular double core hole states.

In this work, we explore the potential of double core hole electron spectroscopy for chemical analysis in terms of x-ray two-photon photoelectron spectroscopy (XTPPS). The creation of deep single and double core vacancies induces significant reorganization of valence electrons. The corresponding relaxation energies and the interatomic relaxation energies are evaluated by CASSCF calculations. We propose a method how to experimentally extract these quantities by the measurement of single and double core-hole ionization potentials (IPs and DIPs). The influence of the chemical environment on these DIPs is also discussed for states with two holes at the same atomic site and states with two holes at two different atomic sites. Electron density difference between the ground and double core-hole states clearly shows the relaxations accompanying the double core-hole ionization. The effect is also compared with the sensitivity of single core hole ionization potentials (IPs) arising in single core hole electron spectroscopy. We have demonstrated the method for a representative set of small molecules LiF, BeO, BF, CO,  $N_2$ ,  $C_2H_2$ ,  $C_2H_4$ ,  $C_2H_6$ ,  $CO_2$  and  $N_2O$ . The scalar relativistic effect on IPs and on DIPs are briefly addressed.

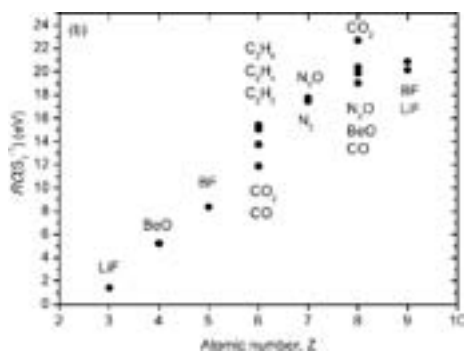


**Figure 2.** Generalized relaxation energy extracted by the double-core hole IP.

## 3. Photochemistry of Ultraviolet B Blocking Cinnamates<sup>3)</sup>

We investigated the absorption and emission spectra of UVB blocking cinnamate derivatives with five different substituted positions using the symmetry-adapted cluster configuration interaction (SAC-CI) method. This series included *cis*- and *trans*-isomers of *ortho*-, *meta*-, and *para*-monomethoxy substituted compounds and 2,4,5-(*ortho*-, *meta*-, *para*-) and 2,4,6-(*ortho*-, *para*-) trimethoxy substituted compounds. The ground state and excited state geometries were obtained at the B3LYP and CIS levels of theory. All the compounds were stable as *cis*- and *trans*-isomers in the planar structure in both the  $S_0$  and  $S_1$  states, except the 2,4,6-trimethoxy substituted compound. The SAC-CI calculations reproduced the recently observed absorption and emission spectra satisfactorily. Three low-lying excited states were found to be relevant for the absorption in the UV blocking energy region. The calculated oscillator strengths of the *trans*-isomers were larger than the respective *cis*-isomers, which is in good agreement with the experimental data. In the *ortho*- and *meta*-monomethoxy compounds, the most intense peak was assigned as the transition from next HOMO to LUMO, whereas in the *para*-monomethoxy compound, it was assigned to the HOMO to LUMO transition. This feature was interpreted as being from the variation of the MOs due to the different substituted positions, and was used to explain the behavior of the excited states of the trimethoxy compounds. The emission from the local minimum in the planar structure was calculated for the *cis*- and *trans*-isomers of the five compounds. The relaxation paths which lead to the non-radiative decay were also investigated briefly. Figure 3 compares the UV and SAC-CI spectra of *para*-methoxy-methyl-cinnamate.

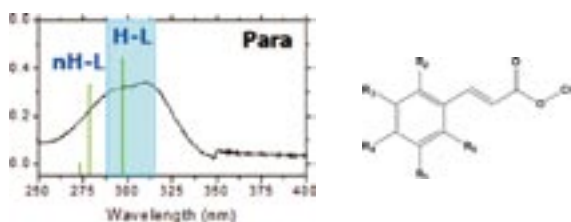


**Figure 3.** Absorption spectrum of *para*-methoxy-methyl-cinnamate.

### References

- 1) R. Cammi, R. Fukuda, M. Ehara and H. Nakatsuji, *J. Chem. Phys.* **133**, 024104 (24 pages) (2010).
- 2) M. Tashiro, M. Ehara, H. Fukuzawa, K. Ueda, C. Buth, N. Z. Kryzhevoi and L. S. Cederbaum, *J. Chem. Phys.* **132**, 184302 (11 pages) (2010).
- 3) M. Promkatkaew, S. Suramitr, T. K. Karpkird, S. Namuangruk, M. Ehara and S. Hannongbua, *J. Chem. Phys.* **131**, 224306 (10 pages) (2009).

### Award

EHARA, Masahiro; QSCP (Quantum Systems in Chemistry and Physics) Prize 2009 CMOA (Centre de Mecanique Ondulatoire Appliquee).

# Development of New Algorithms for Molecular Dynamics Simulation and Its Application to Biomolecular Systems

Department of Theoretical and Computational Molecular Science  
Division of Computational Molecular Science



OKUMURA, Hisashi	Associate Professor
ITOH, G. Satoru	Assistant Professor
KAWAGUCHI, Ritsuko	Secretary
UENO, Harumi	Secretary

Effective samplings in the conformational space by Monte Carlo and molecular dynamics simulations are necessary to predict the native structures of proteins. In the conventional canonical-ensemble simulations, however, it is difficult to realize effective samplings in complex systems such as proteins. This is because the usual canonical-ensemble simulations tend to get trapped in a few of many local-minimum states. To overcome these difficulties, we proposed new generalized-ensemble algorithms.

## 1. Replica-Exchange Method in van der Waals Radius Space: Overcoming Steric Restrictions for Biomolecules<sup>1)</sup>

The replica-exchange method is one of the most well-known methods among the generalized-ensemble algorithms. For large systems such as proteins in aqueous solution, however, the usual replica-exchange method has a difficulty. We need to increase the number of replicas in proportion to  $O(f^{1/2})$ , where  $f$  is the number of degrees of freedom. Large biomolecular systems, therefore, require a large number of replicas in the replica-exchange method and hence huge amount of computation time. In order to overcome this difficulty, Hamiltonian replica-exchange method is sometimes employed.

We present a new type of the Hamiltonian replica-exchange method, where the van der Waals radius parameter and not the

temperature is exchanged. By decreasing the van der Waals radii, which control spatial sizes of atoms, this Hamiltonian replica-exchange method overcomes the steric restrictions and energy barriers. Furthermore, the simulation based on this method escapes from the local-minimum free-energy states and realizes effective sampling in the conformational space. We applied this method to an alanine dipeptide (Figure 1) in aqueous solution and showed the effectiveness of the method by comparing the results with those obtained from the conventional canonical and replica-exchange methods.

## 2. Optimization of Partial Multicanonical Algorithm for Molecular Dynamics and Monte Carlo Simulations

The multicanonical ensemble algorithm is another one of the most well-known generalized-ensemble algorithms. A non-Boltzmann weight factor is employed in this ensemble so that a free one-dimensional random walk can be realized in the potential-energy space. Thus, a simulation with this algorithm can escape from the free-energy-minimum states and sample a wide range of the conformational space. Because of this advantage, the multicanonical algorithm has been frequently applied to a biomolecule, which has a free-energy surface with many local minima. However, the non-Boltzmann weight factor in the multicanonical algorithm is not *a priori* known and has to be determined by a preliminary simulation. As the



system size increases, the distribution of the total potential energy gets narrower. Thus, the determination of the multicanonical weight factor to give a flat distribution becomes difficult in a large system.

In order to alleviate this difficulty, we proposed recently the partial multicanonical ensemble algorithm for molecular dynamics and Monte Carlo simulations. The partial multicanonical algorithm samples a wide range of an important part of the potential energy. Although it is a strong technique for structure prediction of biomolecules, the choice of the partial potential energy has not been optimized. In order to find the best choice, partial multicanonical molecular dynamics simulations of an alanine dipeptide in explicit water solvent were performed with 15 trial choices for the partial potential energy. The best choice was found to be the sum of the electrostatic, Lennard-Jones, and torsion-angle potential energies between solute atoms. In this case, the partial multicanonical simulation sampled all of the local-minimum free-energy states of the  $P_{II}$ ,  $C_5$ ,  $\alpha_R$ ,  $\alpha_P$ ,  $\alpha_L$ , and  $C_7^{ax}$  states and visited these states most frequently. Furthermore, backbone dihedral angles  $\phi$  and  $\psi$  rotated very well. It is also found that the most important term among these three terms is the electrostatic potential energy and that the Lennard-Jones term also helps the simulation to overcome the steric restrictions. On the other hand, multicanonical simulation sampled all of the six states, but visited these states less time. Conventional canonical simulation sampled only four of the six states: The  $P_{II}$ ,  $C_5$ ,  $\alpha_R$ , and  $\alpha_P$  states.

### 3. Conformational Populations of Ligand-Sized Molecules by Replica Exchange Molecular Dynamics and Temperature Reweighting<sup>2)</sup>

The use of the replica exchange molecular dynamics method for the efficient estimation of conformational populations of ligand-sized molecules in solution is investigated.

We compare the computational efficiency of the traditional constant temperature molecular dynamics technique with that of the parallel replica exchange molecular dynamics method for a series of alkanes and rilpivirine (TMC278), an inhibitor against HIV-1 reverse transcriptase, with implicit solvation. We show that conformational populations are accurately estimated by both methods; however, replica exchange estimates converge at a faster rate, especially for rilpivirine, which is characterized by multiple stable states separated by high-free energy barriers. Furthermore, convergence is enhanced when the weighted histogram analysis method is used to estimate populations from the data collected from multiple replica exchange temperature replicas. For small drug-like molecules with energetic barriers separating the stable states, the use of replica exchange with the weighted histogram analysis method is an efficient computational approach for estimating the contribution of ligand conformational reorganization to binding affinities.

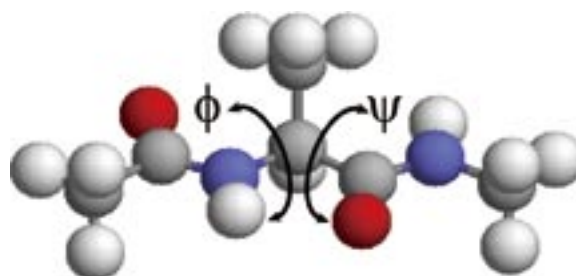


**Figure 1.** The initial conformations of alanine dipeptide for the molecular dynamics simulation.

#### References

- 1) S. G. Itoh, H. Okumura and Y. Okamoto, *J. Chem. Phys.* **132**, 134105 (8 pages) (2010).
- 2) H. Okumura, E. Gallicchio and R. M. Levy, *J. Comput. Chem.* **31**, 1357–1367 (2010).

# Theory and Computation of Reactions and Properties in Solutions and Liquids

Department of Theoretical and Computational Molecular Science  
Division of Computational Molecular Science



ISHIDA, Tateki

Assistant Professor

Our researches are focused on the projects both on ultrafast photoinduced excited state reaction in solution and on ionic liquids (ILs). The project on photoinduced excited state reaction processes in solution focuses on the development of a theoretical method to describe solvent motion and dynamics around a solute molecule in short-time region, including the application of the developed theoretical treatment to solvation processes and excited-state intramolecular electron transfer processes in Betaine dye molecule solution. On the other hand, the aim of ILs projects is to pursue specific interionic dynamics in ILs through many-body polarization effects and to study a new perspective on the characteristics of ILs using dicationic ILs.

## 1. Photoinduced Excited State Reaction Processes: Effects of Solvent Motions and Solvation Processes on Excited-State Intramolecular Processes in Solution

We propose a procedure for describing equation of motions for atoms considering the inertial term with an interaction site model for capturing solvent dynamics attributed to solvent motions in a short-time regime,  $t < 100$  fs. We present a method for calculating the time-dependent evolution of the electronic structure of a solute molecule in solution coupling an electronic structure theory with a solution of the equation which governs the development of the fluctuation of solvent number density with the inertial term. The prescription is applied to the study of solvation dynamics of the simplest betaine dye molecule pyridinium *N*-phenoxide in acetonitrile and methanol in the excited state. It is shown that the coupling between solvation and a fast intramolecular reaction such as charge transfer is likely to play an important role in solvation dynamics of the simplest betaine. Also, it is indicated that intramolecular electron transfer processes in the present dye system could be promoted by solvation dynamics rather than solute structural relaxation such as in twisted intramolecular

charge transfer (TICT) processes.

## 2. Molecular Dynamics Study of the Dynamical Behavior in Ionic Liquids through Interionic Interactions

We have focused on the interionic dynamics of an IL, 1-Butyl-3-Methylimidazolium cation with the anion,  $[\text{PF}_6]^-$ ,  $[\text{BMIm}][\text{PF}_6]$ , and have investigated the interionic interaction in the IL and the polarization effects on the system. Molecular dynamics simulations have been carried out to pursue the understanding of interionic properties in ILs at molecular level. The analyses of velocity cross-correlation functions have been performed to study the interionic interactions. We have computed the momentum correlation functions between ionic species. From simulation results, it is suggested that, at the short time region up to 1 ps, the velocity cross-correlation is predominantly governed by the longitudinal contribution. It is found out that, compared with the longitudinal correlation in the nonpolarizable model, the longitudinal motions are further influenced in the polarizable model. It is indicated that the behavior of mean-squared displacement of the cation at a long-time region is not influenced by polarization effects, while the anion shows important difference. Also, it is concluded that the cage effect in ILs could be reduced by many-body polarization effects. (DOI 10.1016/j.jnoncrysol.2010.05.086)

## 3. New Perspective on the Characteristics of Ionic Liquids

We focus on dicationic ILs with typical counter anions. The molecular dynamics simulations for dicationic ILs systems have been performed. The interionic interactions and the properties dependent on the specific distribution of ionic species are investigated including the analysis of velocity autocorrelation and polarizability time correlation functions.

## Visiting Professors



Visiting Professor  
**NAKAI, Hiromi** (*from Waseda University*)

### Linear-Scaling Divide-and-Conquer Correlation Theory for Treating Large Systems

“Divide each of the difficulties under examination into as many parts as possible, and as might be necessary for its adequate solution.” This quote is from René Descartes, the famous French philosopher regarded as a founder of modern philosophy, in his “Discourse on Method.” This phrase is none other than the first statement of the divide-and-conquer (DC) approach. The importance of this philosophy has been universal among almost all sciences, especially computer science. The conventional correlation calculation posed difficulties with large systems due to its unfavorable scaling of computational costs. Nakai *et al.* have presented a breakthrough in correlation calculations by combining the DC method with energy density analysis (EDA). The DC-correlation method is capable of achieving linear scaling of CPU times with respect to system size. This success will open new vistas for computational chemistry across a wide range of scientific and technological fields, nanomaterials and biosystems among them.



Visiting Professor  
**TANIMURA, Yoshitaka** (*from Kyoto University*)

### Modeling, Calculating, and Analyzing Multidimensional Spectroscopies

Spectral line shapes in a condensed phase contain information from various dynamic processes that modulate the transition energy, such as microscopic dynamics, inter- and intra-molecular couplings, and solvent dynamics. In multidimensional spectroscopy, the nonlinear response functions of a molecular dipole or polarizability are measured using ultra-short pulses to monitor inter- and intra-molecular vibrational motions. Because complex profile of such signal depends on the many dynamic and structural aspects of molecular system, researchers would like to have a theoretical understanding of these phenomena. We explore and describe the roles of different physical phenomena that arise from the peculiarities of the system-bath coupling in multidimensional spectra. Using the hierarchy formalism, we precisely calculate multi-dimensional spectra for a single and multi-mode anharmonic system for inter- and intra-molecular vibrational modes.



Visiting Associate Professor  
**NISHIYAMA, Katsura** (*from Shimane University*)

### Elucidation of Primary Photochemical Processes of Nanoscaled Luminescent Devices

We have synthesized nanoscaled structures likewise nanorods, nanotubes, and nanowires with a skeleton of rare earth elements. To drive luminescent functions from nanostructures produced in our group, we introduce “light-harvesting antennas” having organic/rare earth hybridized structures into the nano skeleton. Along with the experimental projects, our group has also carried out theoretical studies for the elucidation of primary photochemical processes in the condensed phase. For instance, the RISM framework incorporated with theories describing time evolution of the system has been employed to obtain molecular view of solvation dynamics. Recently we undertake to describe initial luminescent processes using the RISM theory together with quantum chemical approaches.





# RESEARCH ACTIVITIES

## Photo-Molecular Science

We study the interaction between molecules and optical fields with its possible applications to active control of molecular functionality and reactivity. We also develop novel light sources to promote those studies. Two research facilities, the Laser Research Center for Molecular Science and the UVSOR, closely collaborate with the Department.

The core topics of the Department include ultrahigh-precision coherent control of gas- and condensed-phase molecules, high-resolution optical microscopy applied to nanomaterials, synchrotron-based spectroscopy of core-excited molecules and solid-state materials, vacuum-UV photochemistry, and the development of novel laser- and synchrotron-radiation sources.

# Development of Advanced Near-Field Spectroscopy and Application to Nanometric Systems

Department of Photo-Molecular Science  
Division of Photo-Molecular Science I



OKAMOTO, Hiromi  
NARUSHIMA, Tetsuya  
JIANG, Yuqiang  
HARADA, Yosuke  
LIM, Jong Kuk  
WU, Huijun  
NOMURA, Emiko

Professor  
Assistant Professor  
Post-Doctoral Fellow  
Post-Doctoral Fellow  
Post-Doctoral Fellow  
Graduate Student  
Secretary

There is much demand for the study of local optical properties of molecular assemblies and materials, to understand mesoscopic phenomena and/or to construct optoelectronic devices in the nanometric scale. Scanning near-field optical microscopy (SNOM) is an imaging method that enables spatial resolution beyond the diffraction limit of light. Combination of this technique with various advanced spectroscopic methods may offer a direct probe of dynamical processes in nano-materials. It may provide essential and basic knowledge for analyzing origins of characteristic features and functionalities of the nanometric systems. We have constructed apparatuses of near-field spectroscopy for excited-state studies of nano-materials, with the feasibilities of nonlinear and time-resolved measurements. They enable near-field measurements of two-photon induced emission and femtosecond transient transmission, in addition to conventional transmission, emission, and Raman-scattering. Based on these methods, we are investigating the characteristic spatiotemporal behaviors of various metal-nanoparticle systems and molecular assemblies.

## 1. Visualization of Plasmon Wavefunctions and Enhanced Optical Fields Induced in Metal Nanoparticles

We recently reported that wavefunctions of localized plasmon resonances of chemically synthesized metal (Au and Ag) nanoparticles are visualized by near-field transmission or two-photon excitation measurements.<sup>1,2)</sup> Figure 1(a) shows a typical near-field two-photon excitation image of the longitudinal plasmon mode on a Au nanorod, which correspond to the square modulus of the plasmon wavefunction. We also visualized optical fields in Au nanoparticle assemblies by the near-field two-photon excitation imaging method, as shown in Figure 1(b).<sup>1,3)</sup> It was revealed for the dimers that highly localized optical field is generated at the interstitial sites between the particles. In many-particle assemblies, the localized fields were especially intensified at the rim parts of the

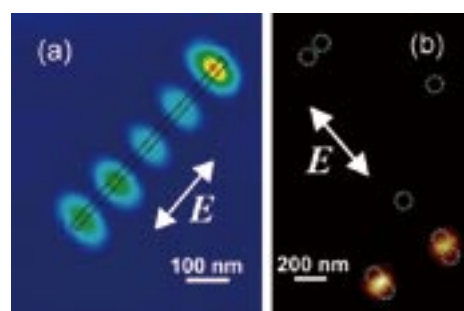


**Figure 1.** Near-field two-photon excitation images of (a) a Au nanorod (diameter 20 nm, length 540 nm), at 780 nm and (b) assembled Au spherical nanoparticles (diameter 100 nm).

assemblies.

We are now extending the studies to metal nanostructures manufactured by the electron-beam lithography technique, in collaboration with researchers of other institution, or other top-down fabrication techniques. Unique nano-optical characteristics, such as anomalous transmission enhancement through metal nanodisks, were found, and characteristic plasmon waves were observed for some metal nanostructures. Near-field properties of nano-void structures, opened on thin gold metallic films on glass substrates, have also been characterized, and the field distributions in the vicinities of the voids have been visualized. In circular void chain structures, we found that confined optical fields were generated in the interstitial sites between voids. The field distributions were analyzed based on the electromagnetic theories and calculations. Special attention has been paid for comparison of field distributions of complementary nanostructures, nanoparticle assembly and nano-void assembly, for instance, in relation to Babinet's principle in optics. Such a study is essential as a basis for designing unique optical properties and functions of metal nanostructures, and their applications to highly sensitive spectroscopic methods and exotic photochemical fields, as well as to nanoscale optical waveguides.

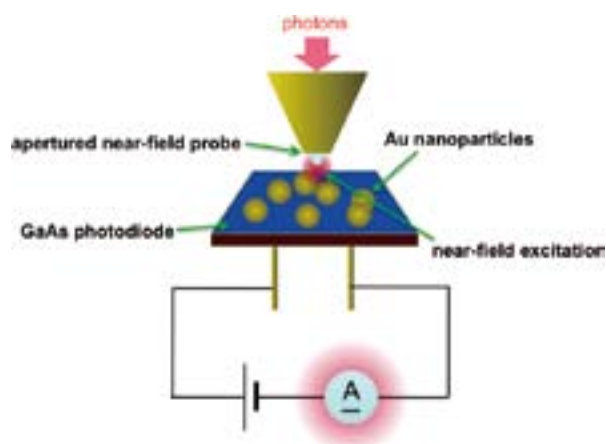


**Figure 2.** Schematic diagram of near-field photocurrent imaging measurement.

## 2. Studies of Metal-Nanostructure Modified Photovoltaic Cells by Near-Field Excited Site-Specific Photocurrent Detection

It has been known that metal nanoparticles and their assemblies collect photon energies to give confined and enhanced optical fields in the vicinities of the particles due to plasmon resonances, under suitably arranged conditions. Recently, it has been reported by a number of researchers that efficiencies of photoenergy conversion systems can be improved by the use of noble metal nanostructures. The photoenergy conversion system ranges from wet-type and solid-state photo-current conversion cells to photo-chemical conversion systems. To reveal the mechanism of the photoenergy conversion process and design more efficient conversion systems, studies of detailed nanostructures and site-dependence of photoirradiation effects are essential.

We applied SNOM to clarify effects of surface plasmon resonance on photo-current conversion in inorganic semiconductor photovoltaic cells modified with metal nanoparticles, where the photocurrent is reported to be enhanced compared with unmodified cells based on macroscopic measurements. The spatial characteristics of photocurrent for GaAs photodiodes with gold nanoparticles (nanospheres and nanorods) dispersed on the active surfaces were investigated by photocurrent imaging using a SNOM (Figure 2). In the case of gold nanospheres (diameter 100 nm), near-infrared light irradiation (785 nm) gave rise to the enhancement of photocurrent, resulted from re-radiation of photons *via* plasmon resonance on the gold nanosphere into the photovoltaic area, while photons in shorter wavelengths did not show enhanced photocurrent. In the case of gold nanorod, characteristic spatial oscillation of photocurrent caused by the longitudinal plasmon mode of the rod was observed. We are now analyzing the results obtained based on the near-field optical characteristics of the metal nanoparticles.

### Award

HARADA, Yosuke; Nano Optics Award, 19<sup>th</sup> Research Symposium of Nano Optics Group, Optical Society of Japan.

## 3. Construction of Apparatuses for Nonlinear and Ultrafast Near-Field Spectroscopy

In previous studies we achieved ultrafast near-field imaging with a time resolution of  $\sim 100$  fs.<sup>2,4)</sup> To further extend the dynamical studies of plasmons, we are now developing basic technologies to achieve near-field time-resolved measurements with  $< 20$  fs time resolution. We are also constructing an apparatus for near-field/far-field microscopic nonlinear optical measurements based on the technique of atomic-force microscope.

## 4. Near-Field Imaging of Organic Molecular Assemblies and Hybrid Systems

We are studying nanometric structures and optical properties of organic molecular assemblies such as carbon nanotubes embedded in sugar polymer chains, LB films of functional conjugated molecules, and hybrid systems consist of metal nanoparticles and organic functional materials, mainly as collaborations with other research groups.

## 5. Nonlinear Effects in Optical Trapping

The optical trapping technique has been widely used in various areas to manipulate particles, cells, and so forth. The principle of trapping is based on the interaction between optical electric fields and induced linear polarizations. In the course of the studies on behavior of gold nanoparticles under pulsed laser fields, we have found a novel phenomenon of optical trapping of spherical gold nanoparticles arising from nonlinear polarization when we trap the nanoparticles by ultrashort near-infrared laser pulses. That is, the stable trap site (usually appears in the center of the focused beam) is split into two equivalent positions, and the split trap positions are aligned along the direction of the incident laser polarization. The split distance depends on the trapping-laser power and wavelength. We have found that the results were successfully interpreted in terms of the nonlinear polarization caused by the femtosecond pulses.

### References

- 1) H. Okamoto and K. Imura, *Prog. Surf. Sci.* **84**, 199–229 (2009).
- 2) K. Imura, T. Nagahara and H. Okamoto, *J. Phys. Chem. B* **108**, 16344–16347 (2004).
- 3) K. Imura, H. Okamoto, M. K. Hossain and M. Kitajima, *Nano Lett.* **6**, 2173–2176 (2006).
- 4) K. Imura and H. Okamoto, *Phys. Rev. B* **77**, 041401(R) (4 pages) (2008).

# Quantum-State Manipulation of Molecular Motions

Department of Photo-Molecular Science  
Division of Photo-Molecular Science I



OHSIMA, Yasuhiro  
HASEGAWA, Hirokazu  
BAEK, Dae Yul  
HAYASHI, Masato  
KITANO, Kenta  
MIYAKE, Shinichiro  
INAGAKI, Itsuko

Professor  
Assistant Professor\*  
IMS Fellow†  
Post-Doctoral Fellow  
Graduate Student‡  
Graduate Student  
Secretary

Molecules in gas phase undergo translational, rotational and vibrational motions in a random manner, and the total molecular system is a statistical ensemble that contains a number of molecules in many different states of motions. This research group aims to establish methods to manipulate the quantum-state distribution pertinent to molecular motions, by utilizing the coherent interaction with laser lights. Here lasers with ultimate resolution in time and energy domains are employed complementally and cooperatively for manipulation of molecular motions.

## 1. Nonadiabatic Rotational Excitation of Molecules by Nonresonant Intense Femtosecond Laser Fields

When gaseous molecules are irradiated by an intense nonresonant ultrafast laser pulse, rotation of molecules is coherently excited via the interaction with the molecular anisotropic polarizability, to create a rotational quantum wave packet (WP). We have developed a method for exploring such a nonadiabatic rotational excitation (NAREX) process in a quantum-state resolved manner, and reported rotational-state distributions after the impulsive excitation with a fundamental output of a femtosecond (fs) Ti:Sapphire laser.<sup>1,2)</sup> Such a state-resolved investigation has afforded details concerning the excitation process during exposure to laser fields, and in a favorable case, full characterization of a rotational WP itself.<sup>3)</sup> In addition, frequency-domain studies can directly assess ultrafast control of the rotational-state distribution via the WP manipulation.<sup>4)</sup>

## 2. Ultrafast Angular-Momentum Orientation by Linearly Polarized Laser Fields<sup>5)</sup>

The anisotropy of molecular system is represented as a non-uniform distribution of projections,  $M$ , of angular momentum onto a space-fixed ( $Z$ ) axis. In particular, the system is designated as being *oriented* when the populations for  $+M$  and

$-M$  are different. In previous studies for the realization of orientation, circularly polarized radiation had been exclusively adopted, because it is regarded as the only way to induce the required helical interaction that breaks the right/left-handed symmetry around the  $Z$  axis. Recently, we show that a pair of linearly-polarized intense ultrafast pulses creates molecular ensembles with oriented rotational angular momentum in ultrafast time scale, when the delay and the mutual polarization between the pulses are appropriately arranged. The experimental result that demonstrates such an angular momentum orientation is shown in Figure 1.

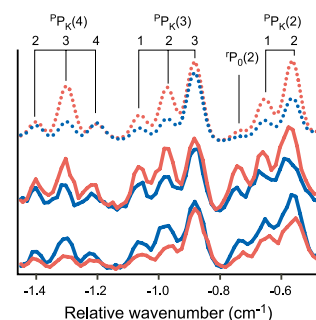


**Figure 1.** Excitation spectra of the  $S_1 \leftarrow S_0 6_0^1$  band of  $C_6H_6$  after fs double-pulse excitation. Blue and red lines correspond to right- and left-handed polarized probe pulses, respectively. The middle and lower panels are experimental ones for the mutual polarization angle of  $-\pi/4$  and  $\pi/4$ , while the upper is simulated one for  $-\pi/4$ .

## 3. Coherent Correlation between Nonadiabatic Rotational Excitation and Angle-Dependent Ionization of NO in Intense Laser Fields<sup>6)</sup>

When the intensity of the nonresonant ultrafast pulse is increased, the irradiated molecules are ionized as well as being rotationally excited. The coherent correlation between NAREX and the strong-field ionization in NO has been studied in the state-resolved manner. When the molecule is partly ionized in intense laser fields, a hole in the rotational WP of the remain-



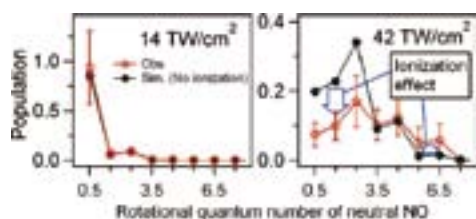


**Figure 2.** Rotational-state distribution of NO recorded after the excitation by a fs pulse at low (left) and high (right) intensity.

ing neutral NO is created by the ionization, whose rate depends on the alignment angle of the molecular axis with respect to the laser polarization direction. Rotational-state distributions of NO are observed and the characteristic feature that the population at higher  $J$  levels is increased by the ionization is identified, as shown in Figure 2. Numerical calculation for solving time-dependent Schrödinger equations including the effect of the ionization is carried out. The results suggest that the molecules aligned perpendicular to the laser polarization direction are dominantly ionized at the peak intensity of  $I_0 = 42 \text{ TW/cm}^2$ , where the multiphoton ionization is preferred rather than the tunneling ionization.

#### 4. Nonadiabatic Vibrational Excitation of Molecular Clusters by Nonresonant Intense Femtosecond Laser Fields

Nonadiabatic interactions with a nonresonant ultrafast laser field can coherently excite molecular vibration. The quantum-state resolved approach with ns probe pulses will also contribute to the study of nonadiabatic excitation of molecular vibration. The best candidates are van der Waals (vdW) clusters, since the librations of constituent molecules in

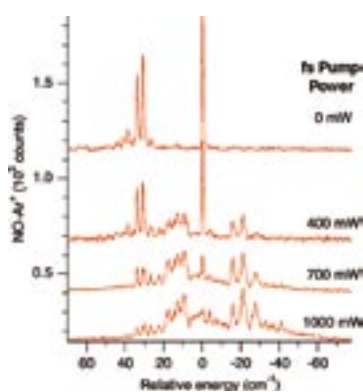


**Figure 3.** Excitation spectra of the A←X (0,0) band of NO-Ar after fs pulse excitation.

#### Award

KITANO, Kenta; Best Presentation Awards at the Annual Meeting of Japan Society for Molecular Science, 2009.

\* Present Address; The University of Tokyo, Graduate School of Arts and Sciences, Department of Basic Science, Tokyo 153-8902

† Present Address; University of Electro-Communications, Institute for Laser Science, Tokyo 182-8585

‡ Present Address; The University of Tokyo, Institute for Solid State Physics, Chiba 277-8581

vdW clusters have wide amplitudes and such intermolecular motions are inherently associated with large modulation of polarizability, yielding to strong Raman activities. We have indeed observed nonadiabatic vibrational excitation for the NO-Ar cluster. After the excitation with an intense fs pulse, several hot bands came to appear, as shown in Figure 3.

#### 5. High-Resolution Laser Spectroscopy of Benzene Clusters with He Atoms

Electronic spectra of benzene-(He)<sub>1,2</sub> clusters have been recorded via two-color resonant two-photon ionization with a single-mode ns-pulsed light source, consisting a dye amplifier injection-seeded by the CW output from a Ti:Sapphire laser. Owing to the narrow band width (~250 MHz) of the laser system and the efficient rotational cooling down to 0.3 K by implementing a high-pressure pulsed valve, rotational fine structures have been fully resolved in the observed spectra, as shown in Figure 4. Several vibronic bands associated to excitation of intermolecular vibrations have also been observed with rotational resolution. Their positions are reasonably matched with the prediction based on a high-level *ab initio* calculation.

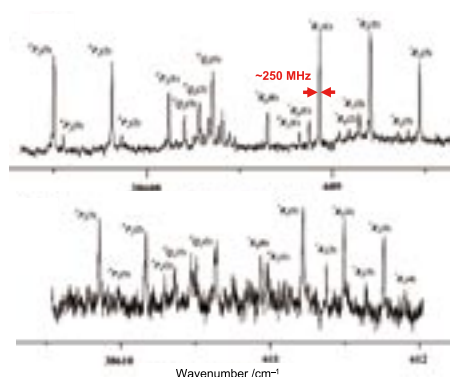


**Figure 4.** High-resolution excitation spectra of the  $S_1 \leftarrow S_0 6_0^1$  band of  $C_6H_6-He$  (top) and  $C_6H_6-(He)_2$  (bottom).

#### References

- 1) H. Hasegawa and Y. Ohshima, *Phys. Rev. A* **74**, 061401 (2006).
- 2) H. Hasegawa and Y. Ohshima, *Chem. Phys. Lett.* **454**, 148 (2008).
- 3) H. Hasegawa and Y. Ohshima, *Phys. Rev. Lett.* **101**, 053002 (2008).
- 4) Y. Ohshima and H. Hasegawa, *Int. Rev. Phys. Chem.* **29**, 619 (2010).
- 5) K. Kitano, H. Hasegawa and Y. Ohshima, *Phys. Rev. Lett.* **103**, 223002 (2009).
- 6) R. Itakura, H. Hasegawa, Y. Kurosaki, A. Yokoyama and Y. Ohshima, *J. Phys. Chem. A* **114**, 11202 (2010).

# Development of High-Precision Coherent Control and Its Applications

Department of Photo-Molecular Science  
Division of Photo-Molecular Science II



OHMORI, Kenji  
KATSUKI, Hiroyuki  
TAKEI, Nobuyuki  
VESHAPIDZE, Giorgi  
IBRAHIM, Heide  
GOTO, Haruka  
NAKAGAWA, Yoshihiro  
INAGAKI, Itsuko

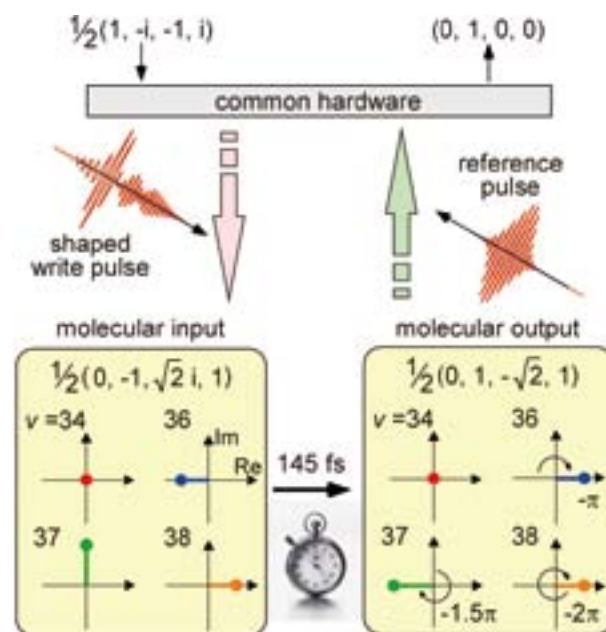
Professor  
Assistant Professor  
Assistant Professor  
Visiting Scientist; JSPS Post-Doctoral Fellow  
Visiting Scientist; JSPS Post-Doctoral Fellow  
Graduate Student  
Graduate Student  
Secretary

Coherent control is based on manipulation of quantum phases of wave functions. It is a basic scheme of controlling a variety of quantum systems from simple atoms to nanostructures with possible applications to novel quantum technologies such as bond-selective chemistry and quantum computation. Coherent control is thus currently one of the principal subjects of various fields of science and technology such as atomic and molecular physics, solid-state physics, quantum electronics, and information science and technology. One promising strategy to carry out coherent control is to use coherent light to modulate a matter wave with its optical phase. We have so far developed a high-precision wave-packet interferometry by stabilizing the relative quantum phase of the two molecular wave packets generated by a pair of femto-second laser pulses on the attosecond time scale. We will apply our high-precision quantum interferometry to gas, liquid, solid, and surface systems to explore and control various quantum phenomena.

## 1. Ultrafast Fourier Transform with a Femtosecond Laser Driven Molecule<sup>1)</sup>

Wave functions of electrically neutral systems can be used as information carriers to replace real charges in the present Si-based circuit, whose further integration will result in a possible disaster where current-leakage is unavoidable with insulators thinned to atomic levels. We have experimentally demonstrated a new logic gate based on the temporal evolution of a wave function. An optically tailored vibrational wave-

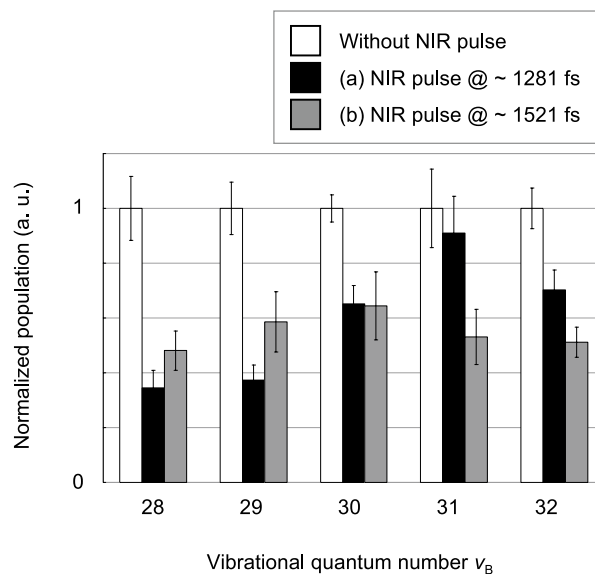
packet in the iodine molecule implements 4- and 8-element discrete Fourier-transform with arbitrary real and imaginary inputs. The evolution time is 145 fs, which is shorter than the typical clock period of the current fastest Si-based computers by three orders of magnitudes.



**Figure 1.** Schematic of the present discrete Fourier transform with an example:  $\frac{1}{2}(1, -i, -1, i) \rightarrow (0, 1, 0, 0)$ . The common transform matrices  $w_4$  and  $w_4^{-1}$  are operated for any arbitrary inputs and outputs, respectively, by the indicated hardware.




## 2. Optical Modification of the Vibrational Distribution of the Iodine Molecule<sup>2)</sup>

We have demonstrated previously that one can read and write information in a diatomic molecule as the population distribution which referred to as a “population code” [*Phys. Rev. Lett.* **104** (2010) 180501; *Phys. Rev. Lett.* **96** (2006) 093002; *Phys. Rev. A* **76** (2007) 013403]. As a next step to this read and write process, modification of the population code is necessary to develop logic gates. Here we demonstrate that the population code in the iodine molecule can be modified by near-infrared femtosecond laser pulses.



**Figure 2.** The vibrational distribution of the iodine molecule has been modified with a near-infrared femtosecond laser pulse.

### References

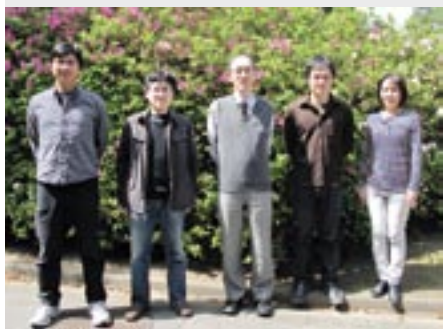
- 1) K. Hosaka, H. Shimada, H. Chiba, H. Katsuki, Y. Teranishi and K. Ohmori, *Phys. Rev. Lett.* **104**, 180501 (2010).  
 Selected for “Editors’ Suggestions” in PRL.  
 Covered by Physics **3**, 38 (2010).  
 Covered by Nature **465**, 138–139 (2010).
- 2) H. Goto, H. Katsuki and K. Ohmori, *Chem. Phys. Lett.* **493**, 170–172 (2010).

### Award

OHMORI, Kenji; Fellow of the American Physical Society.

# Molecular Inner-Shell Spectroscopy: Local Electronic Structure and Intermolecular Interaction

Department of Photo-Molecular Science  
Division of Photo-Molecular Science III



KOSUGI, Nobuhiro  
YAMANE, Hiroyuki  
NAGASAKA, Masanari  
NAKANE, Junko

Professor  
Assistant Professor  
Assistant Professor  
Secretary

In order to reveal local electronic structures and weak intermolecular interactions in molecular solids, liquids, and clusters, we are developing and improving several kinds of soft X-ray spectroscopic techniques such as XPS, XAS, RAS, XES, RXES, and RIXS at UVSOR in-vacuum undulator beamlines BL-3U and BL-6U with some international collaboration programs, and also an original *ab initio* quantum chemical program package GSCF, which is optimized to calculation of molecular inner-shell processes.

## 1. Inner-Shell Spectroscopy and Exchange Interaction of Rydberg Electrons Bound by Singly and Doubly Charged Kr and Xe Atoms in Small Clusters<sup>1)</sup>

Surface-site resolved Kr  $3d_{5/2}$  and Xe  $4d_{5/2}$  ionized states and Kr  $3d_{5/2}^{-1}5p$  and  $3d_{5/2}^{-1}6p$  and Xe  $4d_{5/2}^{-1}6p$  and  $4d_{5/2}^{-1}7p$  Rydberg excited states in small van der Waals Kr and Xe clusters with a mean size of  $\langle N \rangle = 15$  are investigated by X-ray photoelectron spectroscopy (XPS) and X-ray absorption spectroscopy (XAS). Furthermore, surface-site resolved Kr  $4s^{-2}5p$ ,  $4s^{-2}6p$ , and  $4s^{-1}4p^{-1}5p$  shakeup-like Rydberg states in small Kr clusters are investigated by resonant Auger electron spectroscopy (RAS). As shown in Figure 1, the exchange interaction (EX) of the Rydberg electron with the surrounding atoms and the induced polarization (iPL) of the surrounding atoms in the singly and doubly ionized atoms are deduced from the experimental spectra to analyze different surface site contributions in small clusters. The induced polarization and exchange repulsion energies are almost proportional to the number of the nearest neighbor atoms. The present analysis indicates that small Kr and Xe clusters with  $\langle N \rangle = 15$  have an average or mixture structure between the fcc-like cubic and icosahedron-like spherical structures.

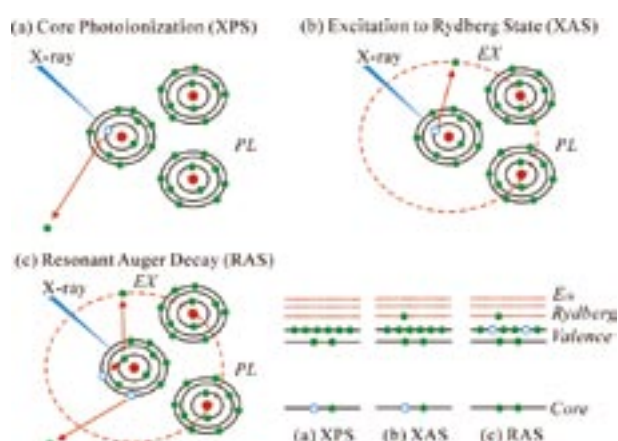


**Figure 1.** The final state in (a) XPS is stabilized by the induced polarization in clusters. The final states in (b) XAS and (c) spectator-like RAS are also stabilized by the induced polarization but are destabilized by the exchange interaction of the Rydberg electron with the surrounding atoms.

## 2. Vibrational Scattering Anisotropy Generated by Multichannel Quantum Interference in C1s- $\pi^*$ Resonance Auger Spectra of Acetylene<sup>2)</sup>

We measured the Fe 2p X-ray absorption spectra of decamethane. Based on angularly and vibrationally resolved electron spectroscopy measurements in acetylene, we report the first observation of anomalously strong vibrational anisotropy of RAS via the C1s- $\pi^*$  excited state with the strong Renner-Teller effect. We provide a model explaining this new phenomenon by three coexisting interference effects: (i) interference between resonant and direct photoionization channels, (ii) interference of the scattering channels through the core-

excited bending states with orthogonal orientation of the molecular orbitals, (iii) scattering through two wells of the double-well bending mode potential. The interplay of nuclear and electronic motions offers in this case a new type of nuclear wave packet interferometry sensitive to the anisotropy of nuclear dynamics: Whether which-path information is available or not depends on the final vibrational state serving for path selection.

### 3. Electric Field Effect on Electronic States in Organic Thin Films Studied by Fluorescence-Yield Soft X-Ray Absorption<sup>3)</sup>

In order to detect *in situ* electronic states of organic field effect transistor (OFET) in operation, we have utilized X-ray absorption spectroscopy (XAS) in the fluorescence yield (FY) mode. FY-XAS is a promising bulk-sensitive method for detection of inner electronic states of organic devices. To our best of knowledge, this is the first successful FY-XAS study on characterization of the organic devices under operating condition. Poly- and oligo-thiophenes are known to show high p-type-like performance. We fabricated 17nm-thick  $\alpha,\omega$ -dihexylsexithiophene (DH6T) films on the 500 nm-thick SiO<sub>2</sub> pre-covered Si substrates (highly B-doped, 0.5 mm-thick), and confirmed clear step-and-terrace morphology on the films by atomic force microscope. For the measurements of bias dependence, full-covered top-contact 25 nm-thick Au electrode was deposited on the DH6T thin films with cooling the substrate below 20 °C. The applied retarding bias exceeded -1 kV to shut out the photoelectrons excited by not only the fundamental X-rays but also the false second-order X-rays generated from gratings.

### 4. Site-Specific Intermolecular Interaction in $\alpha$ -Crystalline Films of Phthalocyanines Studied by Soft X-Ray Emission<sup>4)</sup>

The local electronic structures of crystalline and amorphous films of zinc phthalocyanine (ZnPc, C<sub>32</sub>H<sub>16</sub>N<sub>8</sub>Zn) and metal-free phthalocyanine (H<sub>2</sub>Pc, C<sub>32</sub>H<sub>18</sub>N<sub>8</sub>) have been studied using photon-in-photon-out type resonant X-ray emission spectroscopy (RXES) with a novel optical design based on a Wolter type I mirror, a transmission grating, and a back-illuminated charge couples device detector, which enables a high light-gathering capability without sacrificing the energy resolution. We found a clear crystalline structure dependence of the elastic-peak lineshape in RXES. As shown in Figure 2, the elastic peak observed for the crystalline films of ZnPc and H<sub>2</sub>Pc shows an asymmetric lineshape with resonant inelastic scattering (RIXS) structures, which cannot be observed for the amorphous films. The observed structure can be ascribed to the interplay of the intermolecular charge transfer excitation and the vibronic excitation that accompanies a direct recombination emission due to the Raman-active intermolecular interaction in crystalline phthalocyanine films.

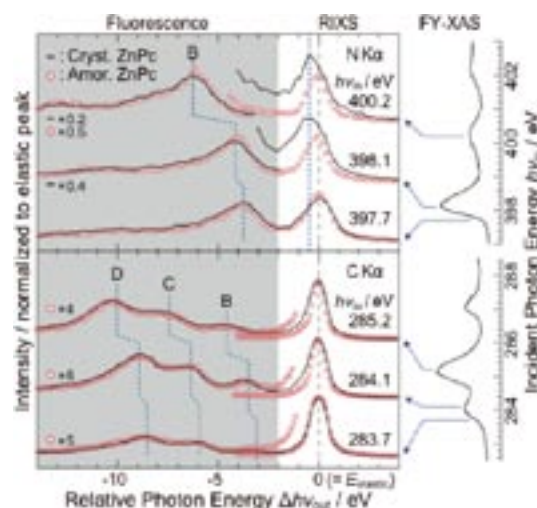


**Figure 2.** C and N K $\alpha$  RXES and RIXS spectra for the crystalline and amorphous ZnPc films. The abscissa is the energy difference between emitted and incident photons  $\Delta h\nu_{out}$  ( $= h\nu_{out} - h\nu_{in}$ ). All the spectra are normalized to the elastic peak intensity. The spectra for the crystalline and amorphous ZnPc films are shown using solid curves (black) and opened circles (red), respectively. The C and N K-edge FY-XAS spectra for the crystalline ZnPc film are shown in the right panel.

### 5. Orientation of *n*-Alkane in Thin Films on Graphite (0001) Studied by Soft X-Ray Absorption<sup>5)</sup>

We observed soft X-ray absorption spectra at the carbon K-edge of *n*-C<sub>12</sub>H<sub>26</sub> films grown on graphite (0001). The C1s-to- $\sigma^*_{CH}$ +Rydberg resonance directed along the CH bond was observed at 286.9 eV for the first layer of the *n*-C<sub>12</sub>H<sub>26</sub> film on graphite. This indicates that the CCC plane of the molecule is parallel to the surface (flat-on orientation). As the film thickness increases, the C1s-to- $\sigma^*_{CH}$ +Rydberg resonance directed perpendicular to the CH bond grows at 288.0 eV, suggesting an increase in the number of molecules with the CCC plane perpendicular to the surface in a multilayer film.

#### References

- 1) M. Nagasaka, T. Hatsui, H. Setoyama, E. Rühl and N. Kosugi, *J. Electron Spectrosc. Relat. Phenom.* (2010), in press.
- 2) C. Miron, V. Kimberg, P. Morin, C. Nicolas, N. Kosugi, S. Gavriluk and F. Gel'mukhanov, *Phys. Rev. Lett.* **105**, 093002 (2010).
- 3) H. S. Kato, H. Yamane, N. Kosugi and M. Kawai, to be published.
- 4) H. Yamane, T. Hatsui, K. Iketaki, T. Kaji, M. Hiramoto and N. Kosugi, to be published.
- 5) O. Endo, H. Ozaki, R. Sumii, K. Amemiya, M. Nakamura and N. Kosugi, to be published.

# Photoabsorption and Photoionization Studies of Fullerenes and Development of High-Efficiency Organic Solar Cells

Department of Photo-Molecular Science  
Division of Photo-Molecular Science III



MITSUKE, Koichiro	Associate Professor
KATAYANAGI, Hideki	Assistant Professor
PRODHAN, Md. Serajul Islam	Post-Doctoral Fellow
BASHYAL, Deepak	Graduate Student
ASARI, Chie	Technical Fellow
FUKUDA, Tatsuya	Technical Fellow

As the first topic, we have observed the formation of singly- and multiply-charged photoions from gaseous fullerenes irradiated with synchrotron radiation at  $h\nu = 25$  to 200 eV. We thus studied the mechanisms and kinetics of consecutive  $C_2$ -release reactions on the basis of (i) the yield curves for the fragments  $C_{60(70)-2n}^{z+}$  ( $n \geq 1$ ,  $z = 1-3$ ) as a function of the primary internal energy of the parent  $C_{60(70)}^{z+}$  and (ii) the three dimensional velocity distributions of the fragment carbon clusters.

In the second topic we have fabricated dye-sensitized solar cells (DSSC) containing ruthenium dye and iodide electrolyte and measured their short current and the intensity of the transmitted light to estimate the wavelength dependence of the incidence photon-to-current conversion efficiency (IPCE) and photoabsorbance (ABS) in the range of 300 to 1000 nm. In addition, we evaluated the quantum yield (APCE) of DSSCs for the electron injection from the excited orbital of Ru dye to the conduction band of  $TiO_2$  nano particles. Our final goal is to develop DSSCs with high performance and long lifetime by improving ABS and APCE mainly in the near infrared region.

## 1. Feasibility Study on the Mass-Selected Velocity Map Imaging of Polyatomic Molecules and Fullerenes<sup>1)</sup>

A photoionization spectrometer for velocity map imaging (VMI) has been developed for measuring the scattering distribution of fragment ions from polyatomic molecules. The spectrometer contains a mass gate and an ion reflector which can discriminate ions with a particular mass-to-charge ratio  $m/z$ . The basic functions and feasibility of these devices were tested experimentally and theoretically. First, the photoions from Kr and  $C_{60}$  were extracted into a time-of-flight (TOF) mass spectrometer by pulsed or continuous electrostatic fields. When the pulse-application timing on the mass gate was tuned to a specific  $m/z$ , the peak of the selected ions alone was present on a TOF spectrum. Second, the performance of the

mass gate in the VMI spectrometer was investigated by the computer simulations of the ion trajectories of fragments from  $C_{60}$ . The initial three-dimensional velocity distribution of  $C_{58}^+$  was projected onto the image plane with an energy resolution better than 10 meV. The  $C_{58}^+$  image was free from the contamination of other ions, e.g.  $C_{60}^+$  and  $C_{56}^+$ .

## 2. Mass-Analyzed Velocity Map Imaging of Thermal Photofragments from $C_{60}$ <sup>2)</sup>

The velocity distributions of the fragments produced by dissociative photoionization of  $C_{60}$  have been measured in the extreme UV region for the first time (see Figure 1), by using a flight-time resolved velocity map imaging technique combined with a high-temperature molecular beam and synchrotron radiation. Values of the average kinetic energy release were estimated at 6 different photon energies with respect to five reaction steps of sequential  $C_2$  ejection, starting from  $C_{60}^{2+} \rightarrow C_{58}^{2+} + C_2$  to  $C_{52}^{2+} \rightarrow C_{50}^{2+} + C_2$ . The translational temperatures of the fragment ions were found to be lower than those obtained by laser multiphoton absorption of  $C_{60}$ . The kinetic energies released in the first to fourth steps increase with increasing  $h\nu$  and reach 0.35–0.5 eV at  $h\nu = 102$  eV, reflecting statistical redistribution of the excess energy in the transition state, whereas that in the fifth step leading to  $C_{50}^{2+}$  was exceptionally small.

## 3. Mass-Analyzed Velocity Map Imaging of Thermal Photofragments from $C_{70}$

When  $C_{70}$  fullerenes absorb extreme UV photons of synchrotron radiation, primary parent ions undergo stepwise  $C_2$  ejection to produce fragment ions containing even-numbered carbon atoms. We have measured (1) the yield curves of the  $C_{70-2n}^{2+}$  fragments ( $1 \leq n \leq 6$ ) from  $C_{70}$  by TOF mass spectrometry and (2) their translational temperatures by velocity

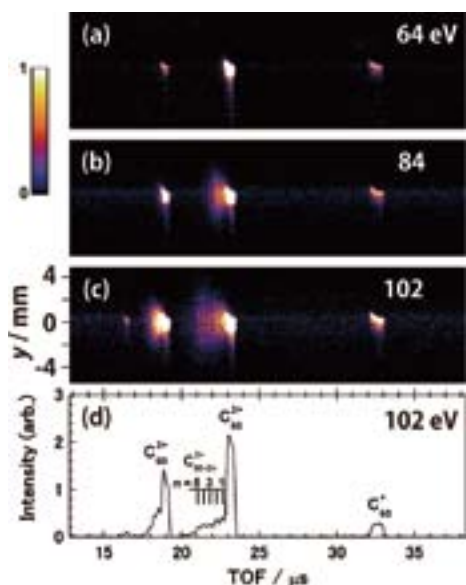


**Figure 1.** (a-c)  $y$ - $t$  maps of the photoions from  $C_{60}$  on which their counts are represented as a function of their arrival time  $t$  and the  $y$  coordinate of their incidence position on the PSD. The list-mode data at three  $h\nu$  positions are integrated over the whole  $x$  range. The  $y$  coordinate is proportional to the  $y$  component of the ion velocity. (d) TOF spectra of the photoions at  $h\nu = 102$  eV obtained by integrating the signal counts of (c) over the whole  $y$  range.

map imaging technique. The yield curve and translational temperature showed marked anomalies at  $n = 5$ , which may arise from exceptional stability of the  $C_{60}^{2+}$  fragments that have an icosahedral structure similarly to isolated  $C_{60}$  fullerene.

#### 4. Preparation and Evaluation of High Efficiency DSSCs<sup>3)</sup>

The high efficiency DSSCs were fabricated by using a screen-printing technique and a wet process. A  $TiO_2$  anode was immersed for 3 days in the acetonitrile solution of Ru complex compound (N719). The mixture of  $I_2$ , iodide salt, acetonitrile, etc. was used as a redox electrolyte. The counter electrode was covered with thin platinum film. The  $I$ - $V$  characteristics of DSSCs were recorded under simulated sun light (power density =  $100 \text{ mW cm}^{-2}$ ). The highest overall energy conversion efficiency was *ca.*  $\sim 8\%$ . The IPCE was calculated from the short current density and radiation power density as a function of the wavelength. The IPCE curve showed a peak of 0.73 at 535 nm. The performance and long-term stability of the DSSCs were studied by changing the thickness of the  $TiO_2$  film, the deposition method of the Pt film, and the compositions of the redox electrolyte.

#### 5. Azo Dyes as Photosensitizers for Organic Solar Cells<sup>4)</sup>

Fabrication and performance tests are reported on DSSCs containing azo dyes as photosensitizers. Fundamental properties of the DSSCs were obtained on the energy conversion

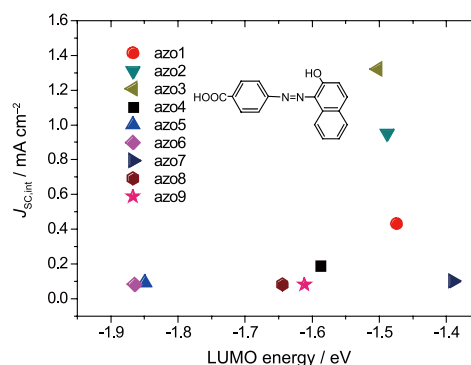


**Figure 2.** Correlation between the experimental data of the short current density of DSSCs and the theoretical energy levels of the LUMO of the solitary azo dyes.

efficiency  $\eta$ , short current and photoabsorbance in the wavelength range of 300 to 800 nm. Various azo dyes were synthesized in such a way that the positions and numbers of carboxylate and hydroxy groups differ from one dye to another. The carboxylate groups are considered to form strong linkages with the surface of  $TiO_2$  nanoparticles to promote rapid electron injection from dye molecules to the conduction band of  $TiO_2$ . We could demonstrate a remarkable correlation between the performance of the DSSCs and the energy level of the lowest unoccupied molecular orbital (LUMO) of the azo dye: no dye whose LUMO energy is lower than  $-1.5 \text{ eV}$  could allow us to make DSSCs with  $\eta > 0.1\%$  (see Figure 2). This finding is consistent with the necessary condition for the DSSC that the LUMO level should be higher than the lower bound of the conduction band of  $TiO_2$ .

#### 6. Transient Fluorescence Spectroscopy of DSSCs Using Picosecond Laser

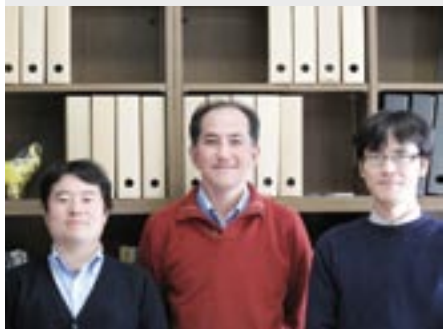
Observation was made on luminescence decay by time-resolved single photon counting using a picosecond laser  $\sim 470$  nm or free electron laser of  $\sim 580$  nm which operates at a repetition rate of 45 or 11.3 MHz, respectively. The apparent luminescence lifetime of the DSSC exposed to the air is longer than that preserved in vacuum, due to unwanted aggregation of the dye molecules at the surface of  $TiO_2$  of the former DSSC. The kinetics of electron injection will be discussed on the basis of the luminescence lifetime of various DSSCs and photo-voltaic electrodes

#### References

- 1) H. Katayanagi, B. P. Kafle, C. Huang, Md. S. I. Prodhon, H. Yagi and K. Mitsuke, *Proc. Pure and Applied Chemistry International Conference PACCON2010*, 941 (2010).
- 2) H. Katayanagi and K. Mitsuke, *J. Chem. Phys.* **133**, 081101 (2010).
- 3) Y. Poo-arporn, V. Vailikhit, D. Bashyal, K. Nakajima, P. Songsiririthikul and K. Mitsuke, *Proc. Pure and Applied Chemistry International Conference PACCON2010*, 424 (2010).
- 4) K. Nakajima, K. Ohta, H. Katayanagi and K. Mitsuke, *Proc. Pure and Applied Chemistry International Conference PACCON2010*, 967 (2010).

# Dynamics of Atoms & Molecules in Intense Laser Fields

Department of Photo-Molecular Science  
Division of Photo-Molecular Science III



HISHIKAWA, Akiyoshi  
FUSHITANI, Mizuho  
TSENG, Chien-Ming  
MATSUDA, Akitaka  
NAKANE, Junko

Associate Professor  
Assistant Professor  
IMS Fellow  
Post-Doctoral Fellow  
Secretary

Intense laser fields, comparable in magnitude with the Coulomb field within atoms and molecules, can be generated by focussing high-energy and ultrashort laser pulses. When exposed to such a strongly perturbing field, molecules exhibit various exotic features that cannot be observed in weak laser fields. We are seeking a deeper understanding of the behavior of molecules in intense laser fields, to elucidate how molecules interact with light, as well as to apply the new features they exhibit to the real-time visualization of ultrafast chemical reactions and their control. In particular, we focus on the following research directions:

- (A) Understanding of atomic and molecular dynamics in intense laser fields and the control
- (B) Ultrafast reaction imaging by laser Coulomb explosion imaging
- (C) Generation and application of ultrashort soft-X-ray pulses by laser high-order harmonics.

## 1. Development of Novel Photoelectron–Photoelectron Coincidence Spectrometer

Molecules in intense laser fields show characteristic reaction processes, such as above-threshold dissociation (ATD), bond softening/hardening and deformation of the geometrical structures. Since these interesting phenomena are all associated with rearrangement of the electron distribution by the intense laser fields, photoelectrons should provide direct information on how these reactions are induced. Here we developed a novel electron–electron–ion coincidence spectrometer to detect a pair of photoelectrons emitted simultaneously from a single molecule to understand the electron correlation dynamics in intense laser fields.

The spectrometer is based on a magnetic bottle type photoelectron spectrometer (see Figure 1). A strong permanent magnet located close to the FEL focus point provides an inhomogeneous magnetic field, which serves as a magnetic mirror for photoelectrons. The reflected photoelectrons are hence guided by the weak magnetic field of a long solenoid

toward a microchannel plate (MCP) detector placed at the end of a 1.5 m flight pass. The high collection efficiency with a  $4\pi$ -sr detection angle and the long light pass enables us to detect pairs of electrons emitted from a single atom. In order to securely identify the counter part ion, a pulsed high voltage is applied to the permanent magnet and ion collection electrodes to guide the ions to the same MCP detector used for electrons. The spectrometer was applied to double ionization of  $\text{CS}_2$  in IR (1.030  $\mu\text{m}$ ) intense laser fields, to reveal the ejection of the two electrons mostly proceeds sequentially at a field intensity of  $2.8 \times 10^{13} \text{ W/cm}^2$ .

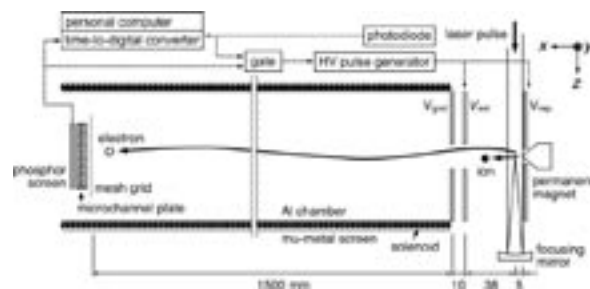


**Figure 1.** Schematic of photoelectron coincidence spectrometer equipped with collection electrodes for ion detection.

## 2. Visualization of Ultrafast Molecular Isomerization by Laser Coulomb Explosion Imaging

Novel features of molecules in intense laser fields can be utilized for new applications. Laser Coulomb explosion imaging is one such application, which provide a unique opportunity for real-time probing of large-scale structural changes in ultrafast chemical reactions.

Figure 2 shows the Newton diagram of three-body Coulomb explosion pathway of formaldehyde,  $\text{H}_2\text{CO}^{3+} \rightarrow \text{H}^+ + \text{H}^+ + \text{CO}^+$ . The diagram observed for the 7 fs case shows a clear and dense distribution of the  $\text{H}^+$  ion, located mostly in the first and fourth quadrant. The corresponding distribution for



the 35 fs case exhibits a significant broadening extending towards smaller momentum angle  $\theta_{\text{H-H}}$ . This finding shows that, when few-cycle intense laser pulses (7 fs) are used, the geometrical structure of the molecule is almost frozen along the H-C-H bending coordinate during the interaction with the laser pulse. On the other hand, significant deformation of the geometrical structure both along the C-H stretching and H-C-H bending coordinates is observed for the 35 fs laser pulses. The origin of the structural change can be understood in terms of the nuclear dynamics in the dication states populated in the rising edge of the laser pulse.

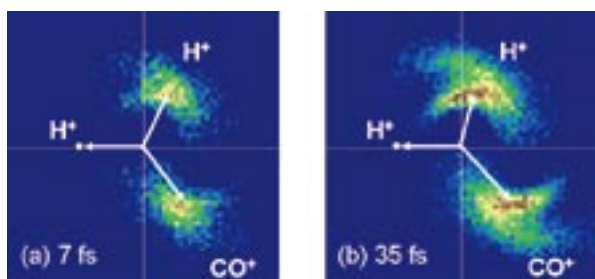


**Figure 2.** The Newton diagrams of  $\text{H}_2\text{CO}_3^+ \rightarrow \text{H}^+ + \text{H}^+ + \text{CO}^+$  in (a) 7 fs and (b) 35 fs intense laser fields, respectively. The amplitude of the linear momentum of the first  $\text{H}^+$  is normalized to unity and the normalized vector is placed on the negative  $x$ -axis.

### 3. Multiphoton Double Ionization of Ar in Intense Extreme Ultraviolet Laser Fields Studied by Shot-by-Shot Photoelectron Spectroscopy<sup>1)</sup>

Non-linear optical processes in extreme ultraviolet (EUV) and X-ray laser fields have attracted increasing attention after the advent of intense ultrashort free electron lasers (FEL), for their importance in a variety of applications, such as the creation of warm dense matter, optical switching and imaging of single bio-molecules. In addition to experiments on bulk materials, a number of experimental studies are devoted to clarify non-linear responses of isolated atoms, as they serve as an ideal benchmark for basic understanding on the non-linear EUV process in which both valence and core electrons can participate. We demonstrate that the shot-by-shot spectral monitoring of SASE FEL pulses and photoelectrons provides a clear understanding on the atomic responses to the intense EUV field. We have applied this technique to the multi-photon multiple ionization of Ar irradiated with SASE FEL pulses of mean photon energies around 21 eV. The sequential two-step double ionization due to three-photon absorption, (i)  $\text{Ar} + h\nu \rightarrow \text{Ar}^+ + e^-$  and (ii)  $\text{Ar}^+ + 2h\nu \rightarrow \text{Ar}^{2+} + e^-$ , is unambiguously identified as the dominant multiphoton pathway in a laser field of  $\sim 5 \text{ TW/cm}^2$ . Moreover, the shot-by-shot monitoring of the mean photon energies of the fluctuating FEL spectra clearly uncovered the effect of resonances in the sequential double ionization.

The  $\text{Ar}^{2+} 3p^{-2}$  structures shown in Figure 3 clearly show that both the peak intensities and profiles sensitively depend on the photon energy. This observation manifests the presence

of intermediate resonances in the two-photon ionization of  $\text{Ar}^{2+}$ . In fact, excited  $\text{Ar}^+$  states of the  $[3p^{-2}(^1D)]3d$  configuration lie close to the photoabsorption from  $\text{Ar}^+ 3p^{-1}$  as shown in Figure 3, and these  $\text{Ar}^{+*}$  states can generate resonances in the two-photon ionization of  $\text{Ar}^+$ . The intensity evolutions are dependent on the final  $\text{Ar}^{2+}$  levels, which implies that  $\text{Ar}^{+*}$  resonances are not common in the formations of these different  $\text{Ar}^{2+}$  levels.

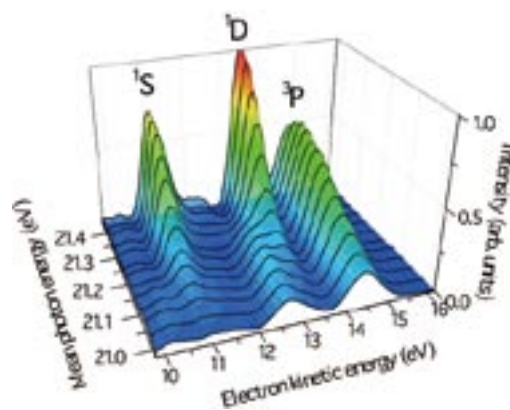


**Figure 3.** Photoelectron spectra in the range of the  $\text{Ar}^{2+} 3p^{-2}$  peaks, derived from a single-shot-basis analysis. In the analysis, the single-shot photoelectron spectra obtained at three different nominal FEL photon energies of 21.0, 21.2 and 21.4 eV were sorted by the mean photon energies determined from the  $\text{Ar}^+ 3p^{-1}$  peak energies, and then averaged within narrow photon energy ranges that divide the whole photon energy range into 13 segments.

### 4. Generation of Laser High-Order Harmonics and Application for Ultrafast Reaction Probing

Laser high-order harmonics have novel features such as i) photon energy higher than several 100 eV, ii) extremely short pulse duration in the sub-fs regime, iii) high-quality spatio-temporal coherence, iv) high photon flux comparable to synchrotron radiation and v) simple and precise synchronization with other laser light sources. Because of these aspects, the laser high-order harmonic pulses are of great interest as a potential light source for time-resolved spectroscopy of ultrafast dynamics that could not be elucidated in real time by conventional techniques. Preliminary pump-probe experiments on the photodissociation of  $\text{Br}_2$  show a steep rise ( $\sim 80$  fs) of the  $\text{Br}(^2P_{3/2})$  yields, reflecting a ultrashort pulse duration ( $< 20$  fs) of the 27th harmonic pulses used to probe the  $\text{Br}(^2P_{3/2})$  product. Full characterization of the temporal profile of the harmonic pulses and application to the time-resolved photoelectron imaging are in progress.

#### Reference

- 1) Y. Hikosaka, M. Fushitani, A. Matsuda, C.-M. Tseng, A. Hishikawa, E. Shigemasa, M. Nagasono, K. Tono, T. Togashi, H. Ohashi, H. Kimura, Y. Senba, M. Yabashi and T. Ishikawa, *Phys. Rev. Lett.* **105**, 133001 (2010).

# Light Source Developments by Using Relativistic Electron Beams

**UVSOR Facility**  
**Division of Advanced Accelerator Research**



KATO, Masahiro  
 ADACHI, Masahiro  
 ZEN, Heishun  
 TANIKAWA, Takanori  
 TAIRA, Yoshitaka  
 KIKUCHI, Yoshitaka

Professor  
 Assistant Professor  
 Assistant Professor  
 Graduate Student  
 Graduate Student\*  
 Graduate Student\*

This project involves researches and developments on synchrotron light source, free electron laser, beam physics and their related technologies. Most of these works are performed at the UVSOR-II electron storage ring and its injector.

## 1. Developments on UVSOR Accelerators

In these years, we have been preparing for a new injection method called top-up injection at UVSOR-II, which would remove the serious short beam lifetime problem caused by the small emittance and the low electron energy.<sup>1)</sup> In this operation scheme, electron beam is re-filled with a short interval, typically one minute, to keep the beam current almost constant.

In 2008, we have started test operation with the top-up injection on every Thursday night. Although the users experiments are greatly improved by the high and constant beam intensity, it was also found that, in some beam-lines, the instantaneous electron orbit movement during the injection affected the experimental data. We prepared a system to deliver beam injection timing signals to the beam-lines that enables the users to stop the data acquisition during the injection. We have also prepared a feedback system to stabilize the injection efficiency. In July 2010, we have started operating the machine with the top-up injection fully in the users beam time. A typical beam current history in a week is shown in Figure 1.

In spring 2010, we have reconstructed a part of the storage ring and the beam transport line to create a new 4 m straight section to install a new undulator which would be dedicated for light source developments. As shown in Figure 2, the beam transport line was extended, the injection pulse magnets, the RF cavity and some instruments for beam diagnostics were also moved. After the three month reconstruction work, the accelerator was successfully re-commissioned on schedule. An undulator system is under construction, which will be installed in the straight section in spring, 2011.

We are investigating some possibility of further upgrade of UVSOR-II as a future plan in near term. It was found that, by

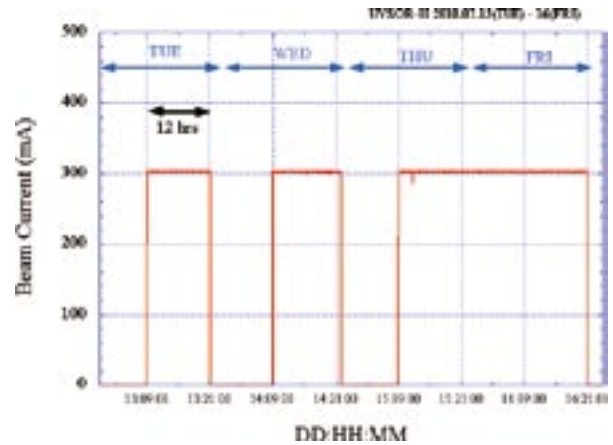


**Figure 1.** Beam current history in the top-up test operation in a week. The ring is operated for 12 hours on Tuesday and Wednesday, and 36 hours from Thursday to Friday in the top-up mode as keeping the beam current at 300mA.



**Figure 2.** A part of the storage ring and the beam transport line in spring 2010, before the reconstruction (left) and after (right). The beam transport line was extended and a new 4m straight section was created in the ring. The devices colored in blue are bending magnets.

introducing combined function bending magnets, the beam emittance could be reduced by a factor of 2. This upgrade would make UVSOR-II the world brightest low energy synchrotron light source. Other possibilities on the future plan are also under investigation, which include a ultra-low emittance storage ring, a linac-based free electron laser or an energy recovery linac.

## 2. Light Source Developments

A resonator-type free electron laser is operational at UVSOR. The wavelength is ranging from 800 nm to 199 nm and the average power exceeds 1W in visible and deep UV regions. In these years, it is used for users experiments<sup>2)</sup> and for basic researches on free electron laser physics. In the latter, coherent photon seeding was successfully demonstrated,<sup>3)</sup> in which a small fraction of the out-coupled laser light was re-injected to the optical cavity and the laser oscillation was drastically stabilized.

By utilizing the free electron laser optical cavity, we have developed a system to create micro-density structure on electron bunches circulating in the storage ring by using an external laser source.<sup>4)</sup> By controlling the laser pulse shape, we can create various density structures such as a short dip structure or a periodic structure. In the former case, broadband coherent terahertz radiation was produced<sup>4)</sup>. In the latter case, quasi-monochromatic coherent terahertz radiation was produced.<sup>5)</sup> Such a micro-density structure normally disappears very quickly after a few revolutions of the electron bunch in the storage ring, which is due to the synchrotron motion. Thus, the intense terahertz radiation also stops. To suppress this effect and maintain the terahertz radiation for a long period, we tried to operate the ring with a small momentum compaction factor. It was observed that the terahertz emission lasted for about ten revolutions. It was also observed that the THz intensity drastically changed revolution by revolution. This peculiar behavior could be explained by the coupling between the longitudinal motion and the transverse motion of the electrons.<sup>6)</sup>

Coherent harmonic generation is a method to produce coherent harmonics of laser light by using relativistic electron beam. The laser-electron interaction in an undulator produces density modulation of a period of the laser wavelength, which also contains harmonic components. Such an electron bunch radiates coherently at the harmonics of the injected laser. We have successfully observed the coherent harmonics of Ti:Sa laser in the VUV range, up to 9<sup>th</sup> harmonic.<sup>7)</sup>

The coherent radiation experiments using laser is supported by the Quantum Beam Technology Program of JST/MEXT. Under this support, a part of the storage ring was reconstructed as described above and a new undulator will be installed. The upgrade of the laser system was completed. Two new beam-lines dedicated to the coherent lights in the VUV range and in the THz range will be constructed.

Laser Compton scattering is a technique to produce a

quasi-monochromatic X-rays and gamma-rays by using a relativistic electron beam and laser. The laser photons are Compton back scattered by the high energy electrons and are converted to gamma-rays. We have successfully demonstrated that the energy of the gamma-rays could be changed continuously by changing the injection angle of the laser. It was expected that a femto-second gamma-ray pulses could be produced by injecting the laser from the vertical direction to the electron beam. The experiment is under going.

## 3. Developments of Accelerator Technologies

Beam diagnostic systems are important especially during the commissioning of a new storage ring or that just after a big reconstruction. In collaborating with Synchrotron Radiation Research Center in Nagoya University, we have developed a turn-by-turn beam position measurement system and a betatron tune measurement system. The former was to measure the beam position of the electron beam just after the injection. The electron orbit of each turn was successfully observed.<sup>8)</sup> In the latter, betatron tunes of the booster synchrotron during the acceleration was successfully measured. A suppression of the betatron motion due to the non-linear magnetic field was successfully observed.<sup>9)</sup>

### References

- 1) M. Katoh, M. Adachi, H. Zen, J. Yamazaki, K. Hayashi, A. Mochihashi, M. Shimada and M. Hosaka, presented at 10<sup>th</sup> Int. Conf. Synchrotron Rad. Instr. (Melbourne, 2009), to be published in *AIP Conf. Proc.*
- 2) J. Takahashi, H. Shinjima, M. Seyama, Y. Ueno, T. Kaneko, K. Kobayashi, H. Mita, M. Adachi, M. Hosaka and M. Katoh, *Int. J. Mol. Sci.* **10**, 3044–3064 (2009).
- 3) C. Evain, C. Szwaj, S. Bielawski, M. Hosaka, A. Mochihashi, M. Katoh and M.-E. Couprie, *Phys. Rev. Lett.* **102**, 134501 (2009).
- 4) M. Shimada, M. Katoh, S. Kimura, A. Mochihashi, M. Hosaka, Y. Takashima, T. Hara and T. Takahashi, *Jpn. J. Appl. Phys.* **46**, 7939–7944 (2007).
- 5) (in alphabetic order) S. Bielawski, C. Evain, T. Hara, M. Hosaka, M. Katoh, S. Kimura, A. Mochihashi, M. Shimada, C. Szwaj, T. Takahashi and Y. Takashima, *Nat. Phys.* **4**, 390–393 (2008).
- 6) M. Shimada, M. Katoh, M. Adachi, T. Tanikawa, S. Kimura, M. Hosaka, N. Yamamoto, Y. Takashima and T. Takahashi, *Phys. Rev. Lett.* **103**, 144802 (2009).
- 7) T. Tanikawa, M. Adachi, M. Katoh, J. Yamazaki, H. Zen, M. Hosaka, Y. Taira and N. Yamamoto, *Proc. 1<sup>st</sup> Int. Particle Acc. Conf.* 2206 (2010).
- 8) A. Nagatani, Y. Takashima, M. Hosaka, N. Yamamoto, K. Takami, M. Katoh, M. Adachi, H. Zen and K. Hayashi, *UVSOR Activity Report 2009* 34 (2010).
- 9) Y. Furui, M. Hosaka, N. Yamamoto, Y. Takashima, M. Adachi, H. Zen and M. Katoh, *UVSOR Activity Report 2009* 32 (2010).

\* carrying out graduate research on Cooperative Education Program of IMS with Nagoya University

# Synchrotron Radiation Spectroscopy on Strongly Correlated Electron Systems

UVSOR Facility  
Division of Advanced Solid State Physics



KIMURA, Shin-ichi	Associate Professor
MATSUNAMI, Masaharu	Assistant Professor
MIYAZAKI, Hidetoshi	IMS Fellow
MORI, Tatsuya	Post-Doctoral Fellow
NISHI, Tatsuhiko	Research Fellow*
MIZUNO, Takafumi	Graduate Student
IIZUKA, Takuya	Graduate Student
MITANI, Hiroyuki	Graduate Student†
HAJIRI, Tetsuya	Graduate Student‡

Solids with strong electron–electron interaction, so-called strongly correlated electron systems (SCES), have a various physical properties, such as non-BCS superconducting, colossal magneto-resistance, heavy fermion and so on, which cannot be predicted by first-principle band structure calculation. Due to the physical properties, the materials are the candidates of the next generation functional materials. We investigate the mechanism of the physical properties as well as the electronic structure of SCES, especially rare-earth compounds, organic superconductors and transition-metal compounds, by infrared/THz spectroscopy and angle-resolved photoemission spectroscopy based on synchrotron radiation. Since experimental techniques using synchrotron radiation are evolved rapidly, the development of the synchrotron radiation instruments is also one of our research subjects.

## 1. SAMRAI: A Variably Polarized Angle-Resolved Photoemission Beamline in the VUV Region at UVSOR-II<sup>1)</sup>

A novel variably polarized angle-resolved photoemission spectroscopy beamline in the vacuum-ultraviolet (VUV) region has been installed at the UVSOR-II 750 MeV synchrotron light source. The beamline is (shown in Figure 1) equipped with a 3 m-long APPLE-II type undulator with horizontally/vertically linear and right/left circular polarizations, a 10-m Wadsworth-type monochromator covering a photon energy range of 6–43 eV, and a 200 mm-radius hemispherical photoelectron analyzer with an electron lens of a  $\pm 18$ -degree acceptance angle. Due to the low emittance of the UVSOR-II storage ring, the light source is regarded as an entrance slit and the undulator light is directly led to a grating by two plane mirrors in the monochromator while maintaining a balance between high energy resolution and high photon flux. The energy resolving power ( $h\nu/\Delta h\nu$ ) and photon flux of the monochromator are typically  $1 \times 10^4$  and  $10^{12}$  photons/sec, respectively, with a

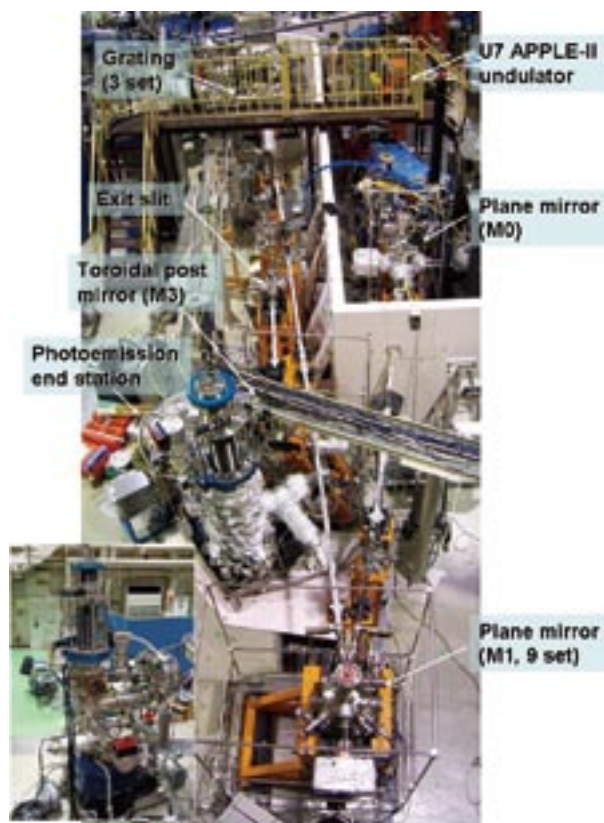


**Figure 1.** Photograph of the SAMRAI beamline consisting of the APPLE-II type undulator (U7), the modified Wadsworth type monochromator (M0–S), and the high-resolution photoemission analyzer at the focal point. The monochromator, mainly has five optical components: two plane mirrors (M0 and M1) with water cooling, one set of three spherical gratings (G), an exit slit (S), and one toroidal refocusing mirror (M3). The spherical gratings with a radius of 10 m are located 22 m from the center of the undulator. There is no entrance slit. S is located 6.47 m from G. A second branch for a VUV microscope end station is planned to be constructed after the plane mirror (M2) located between G and S.

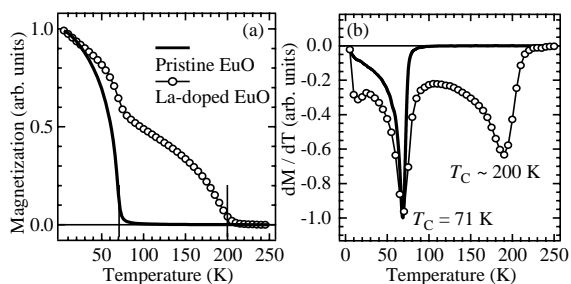


**Figure 2.** Temperature dependence of the normalized magnetization curves (a) and temperature derivative curves of the magnetization as a function of temperature (b) for fabricated La-doped EuO and pristine EuO thin films with a thickness of 100 nm on a SrTiO<sub>3</sub> substrate.

100- $\mu$ m exit slit. The beamline is used for angle-resolved photoemission spectroscopy with an energy resolution of a few meV covering the UV-to-VUV energy range.

## 2. La-Doped EuO: A Rare-Earth Ferromagnetic Semiconductor with the Highest Curie Temperature<sup>2)</sup>

We report the fabrication of single-crystalline La-doped EuO thin films with the highest Curie temperature ( $T_C$ ) of about 200 K among rare-earth compounds excluding transition metals. Due to a first-principle band calculation and an X-ray diffraction measurement, the observed increase of  $T_C$  cannot be explained only by the increase of the hybridization intensity due to the lattice shrinking and by the increase of the up-spin electrons in the Eu 5d state by the electron doping. The hybridization between the Eu 4f and donor states due to the La-substitution is a possible origin of the increases of  $T_C$ .

## 3. Design of Terahertz Pump–Photoemission Probe Spectroscopy Beamline at UVSOR-II<sup>3)</sup>

To elucidate the electronic structure relating to physical properties of solids by using selective excitations of low energy electronic and vibrational structure, a new beamline for novel pump-and-probe spectroscopy experiments combining terahertz coherent synchrotron radiation (THz-CSR) and vacuum-ultraviolet coherent harmonic generation (VUV-CHG) is designed. THz-CSR and VUV-CHG are generated from same electron bunches in the storage ring interacted with an amplitude-modulated pulse laser introduced from the outside of the storage ring. The designed schematic top view of the THz pump–PES probe beamline, BL1, is depicted in Figure 3. The amplitude-modulated Ti:Sa laser pulse (1 kHz, 10 mJ/

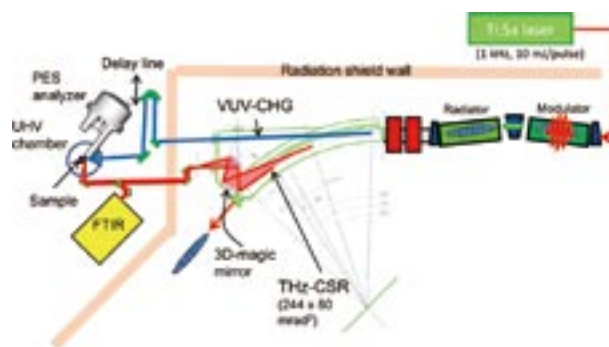


**Figure 3.** Schematic top view of the THz pump – photoemission (PES) probe spectroscopy beamline, BL1, at UVSOR-II. The light sources of PES and THz excitation are the VUV-CHG from “Radiator” and the quasi-monochromatic THz-CSR from the bending-magnet, respectively. For the THz pump – PES probe experiment, the time difference between the THz and VUV lights can be made by the delay line.

pulse) is introduced to the UVSOR-II electron storage ring. Then a periodic energy modulation is created on an electron bunch at one of two undulators, namely “Modulator,” located at the straight section. VUV-CHG is emitted from the modulated electron beam at the downstream undulator, namely “Radiator.” The modulated electron beam also produces the quasi-monochromatic THz-CSR at the bending magnet located at the downstream of the undulators. Since both THz-CSR and VUV-CHG are monochromatic lights, no monochromator for both lights is needed. However, the spectral feature of the THz-CSR must be confirmed by a Fourier transform interferometer (FTIR). Both VUV-CHG and THz-CSR are directed to the same position on a sample in an ultra-high vacuum chamber with a photoelectron analyzer located at the outside of the radiation shielding wall. The THz pump–PES probe experiment is performed as follows; At first, THz-CSR is irradiated to the sample. Just after that, VUV-CHG is irradiated to the sample and PES measured with the time delay. The time delay between the THz-CSR and VUV-CHG is made by the delay line in the optical pass of VUV-CHG. Since the expected 6-th higher harmonics ( $\sim 9$  eV) is not high photon energy, normal incident optics can be used for the delay line.

### References

- 1) S. Kimura, T. Ito, M. Sakai, E. Nakamura, N. Kondo, K. Hayashi, T. Horigome, M. Hosaka, M. Katoh, T. Goto, T. Ejima and K. Soda, *Rev. Sci. Instrum.* **81**, 053104 (2010).
- 2) H. Miyazaki, T. Ito, H. J. Im, K. Terashima, S. Yagi, M. Kato, K. Soda and S. Kimura, *Appl. Phys. Lett.* **96**, 232503 (2010).
- 3) S. Kimura, E. Nakamura, M. Hosaka, T. Takahashi and M. Katoh, *AIP Conf. Proc.* **1234**, 63 (2010).

\* from Chiba University

† Present Address; Fujifilm Corporation

‡ carrying out graduate research on Cooperative Education Program of IMS with Nagoya University

# Electronic Structure and Decay Dynamics in Atoms and Molecules Following Core Hole Creation

UVSOR Facility  
Division of Advanced Photochemistry



SHIGEMASA, Eiji                    Associate Professor  
HIKOSAKA, Yasumasa            Assistant Professor\*  
IWAYAMA, Hiroshi                Assistant Professor

The dynamics of the inner-shell photoexcitation, photoionization, and subsequent decay processes is much more complex, in comparison to outer-shell photo-processes. For instance, the inner-shell photoionization is concomitant with the excitation and ionization of valence electrons, which reveal themselves as shake-up and shake-off satellite structures in the corresponding photoelectron spectrum. The one-photon multi-electron processes, which are entirely due to the electron correlation in the system, are known to happen not only in the primary inner-shell hole creation processes, but also in their relaxation processes. Our research project is focused on elucidating the electronic structures and decay dynamics in core-excited atoms and molecules, by utilizing various spectroscopic techniques together with monochromatized synchrotron radiation in the soft x-ray region.

## 1. PCI Effects in Double Auger Decay Probed by Multi-Electron Coincidence Spectroscopy

An inner atomic vacancy created by photoionization can decay by emission of radiation or by Auger decay. For L shells, the Auger decay is generally more probable and can occur with emission of one electron (single Auger decay) or of a few electrons (multiple Auger decay). The probability of multiple Auger decay is usually lower than the probability of single Auger decay but can be high enough to allow experimental observations. Recent progress in coincidence measurements opened the path to a deeper search of the double Auger (DA) decays. DA implies that the filling of the inner-shell vacancy by an outer electron can cause the ejection of two electrons. This process is in its turn divided into the direct double Auger decay (DDA) when the two electrons are emitted simultaneously and cascade double Auger decay (CDA) when the electrons emission occurs in two steps through the creation and decay of an intermediate quasi stationary state.

PCI is known as a special kind of electron correlation associated to the interaction between the charged particles of a resonant process, through the creation and decay of an intermediate quasi stationary state. In the case of inner shell photoionization, PCI reduces to the interaction of the emitted photoelectron with the Auger electrons and with the ion field which varies during the Auger decay. PCI in single Auger decay following inner-shell photoionization is quite well documented both experimentally and theoretically, but PCI in the DA processes has been much less studied.

In the present study, we reveal and investigate the PCI effects in DA processes, using Ar 2p inner-shell ionization as an example.<sup>1)</sup> We present a systematic investigation of photoelectron spectra measured in coincidence with two Auger electrons. The PCI distortion of the photoelectron and Auger lines is shown to be important both for DDA and CDA processes. Our measurements are supported by calculations based on an eikonal approach of PCI. The results of calculations are in good agreement with the experimental data thus demonstrating the adequacy of the theoretical model to the phenomenon considered. The analysis of the experimental and theoretical results shows that the photoelectron line shape depends both on the variation of the ionic field and on the interaction with the slow Auger electron. Moreover since the line shapes for DDA and CDA processes are slightly different, their analysis allows us to extract properties of the associated DA decays.

## 2. Doppler Effect in Fragment Autoionization Following Core-to-Rydberg Excitations

The Doppler effect is known to occur when the source and observer are in motion relative to each other, leading to an apparent change in the observed frequency of the propagating wave. This effect has a wide variety of applications in many

fields, relating to the sensing of movement. In the research field of molecular physics, the sensing of nuclear motion has long been an important issue. Gel'mukhanov and co-workers predicted in 1997<sup>2)</sup> that the nuclear motion in 'ultrafast dissociation' following molecular core-level photoexcitation can be probed by the Doppler effect in emitted Auger electron. Ultrafast dissociation is a process in which the molecular dissociation at the core-excited state precedes the Auger decay and then an atomic fragment emits an Auger electron. The atomic Auger electron can possess the opposite Doppler shift depending on the direction approaching the detector or moving away from it.

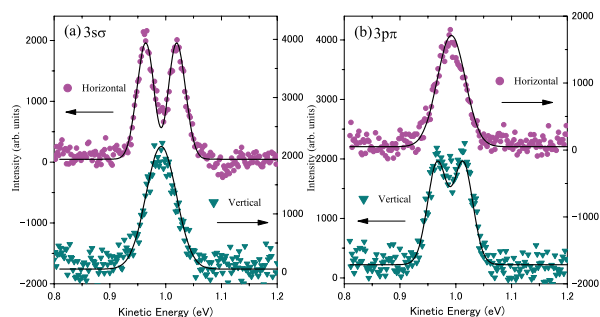


**Figure 1.** Doppler splitting observed in autoionizing electron spectra from an atomic nitrogen following the N1s to (a)  $3s\sigma$  and (b)  $3p\pi$  Rydberg excitations of  $N_2$ .

In the current work, it is demonstrated that the Doppler effect can be utilized as a new tool to study the molecular dynamics at singly-charged ion states produced by resonant Auger decay. Special attention is paid to detecting slow electrons. In cascade Auger decay, two electrons are ejected sequentially with distinct kinetic energies depending on the energy levels of the initial, intermediate, and final electronic states involved. One of the two emitted electrons is often slow (typically less than 5 eV). Singly-charged molecular ion states populated by the first electron emission can undergo competition between second electron emission and molecular dissociation. If one of the dissociating fragments is excited it may subsequently autoionize; the autoionizing atomic fragment can act as an electron emitter which can show Doppler splitting if the kinetic energy of the atomic fragment is sufficiently large and the initial photoabsorption anisotropy is substantially maintained in the angular distribution of fragments. Since anisotropic angular distributions of fragment-ions have clearly been observed in core-to-Rydberg excitations for simple linear molecules, the core-to-Rydberg excitations can be suitable precursors for observing Doppler shifts in the second step electron emissions.

As an example, the polarization dependences of the  $N^*(4d^2F^o)$  autoionization peak following the  $3s\sigma$  and  $3p\pi$  Rydberg excitations are shown in Figure 1. Clear Doppler profiles are observed in the atomic autoionization peaks, which also

display clear polarization dependences on the symmetries of the excited states. It is demonstrated that femtosecond dissociation dynamics of singly-charged ion states produced by resonant Auger decay can be deduced from the information obtained by analysis of the Doppler profiles.

### 3. Construction of a New Experimental Setup for Gas Phase Electron Spectroscopy on BL6U

Parallel to the construction program of BL6U, the installation of a new electron spectrometer for gas phase spectroscopy has been initiated. High-resolution electron spectroscopy is a powerful tool to investigate electronic structures of atoms and molecules, especially when high-resolution electron spectra and their polarization dependences are measured as a function of photon energy in high-resolution mode. The ability of this two dimensional (2D) electron spectroscopy has been demonstrated in our recent work at SPring-8,<sup>3)</sup> where a special attention is paid for detecting slow electrons following core excitations.

Figure 2 shows a photograph of the experimental setup, which is roughly composed of a vacuum chamber, a rotational mechanism, an MBS-A1 analyzer, a gas cell, and a double layer mu-metal screen. The analyzer is rotatable around the photon beam axis. The vacuum chamber and the rotational mechanism have been designed at UVSOR, and fabricated by TOYAMA Co., Ltd. The practical utilization of the new experimental setup has begun since October 2009.

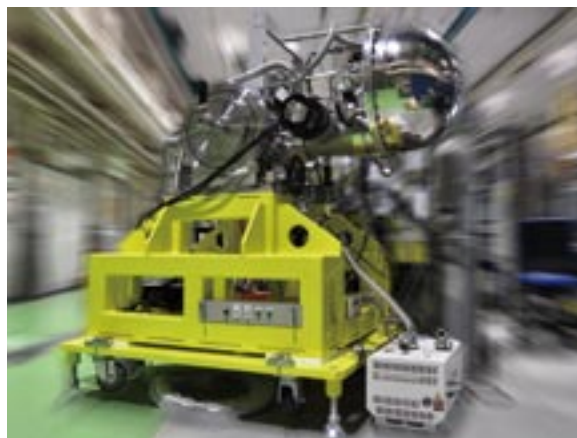


**Figure 2.** A side view of the newly constructed experimental setup for gas phase electron spectroscopy on BL6U.

#### References

- 1) S. Sheinerman *et al.*, *J. Phys. B* **43**, 115001 (9 pages) (2010).
- 2) F. Gel'mukhanov, H. Ågren and P. Salek, *Phys. Rev. A* **57**, 2511–2526 (1998).
- 3) E. Shigemasa *et al.*, *New J. Phys.* **12**, 063030 (9 pages) (2010).

\* Present Address; Department of Environmental Science, Niigata University, Niigata 950-2181

# Micro Solid-State Photonics

Laser Research Center for Molecular Science  
Division of Advanced Laser Development



TAIRA, Takunori  
LOISEAU, Pascal  
ISHIZUKI, Hideki  
AKIYAMA, Jun  
TSUNEKANE, Masaki  
PAVEL, Nicolaie  
SATO, Yoichi  
MATSUSHITA, Tomonori  
JOLY, Simon  
KONG, Weipeng  
ONO, Yoko  
INAGAKI, Yayoi

Associate Professor  
Visiting Associate Professor  
Assistant Professor  
IMS Research Assistant Professor  
Post-Doctoral Fellow  
Post-Doctoral Fellow  
Post-Doctoral Fellow  
Post-Doctoral Fellow  
Post-Doctoral Fellow  
Graduate Student  
Secretary  
Secretary

The artistic optical devices should be compact, reliable, efficient and high power light sources. With the approaches of domain structures and boundaries engineering, it is possible to bring the new interaction in their coherent radiation. The high-brightness nature of Yb or Nd doped single crystal or ceramic microchip lasers can realize efficient nonlinear wavelength conversion. In addition, designed nonlinear polarization under coherent length level allows us new function, such as the quasi phase matching (QPM). The development of “*Micro Solid-State Photonics*,” which is based on the micro domain structure and boundary controlled materials, opens new horizon in the laser science.

## 1. Diode Edge-Pumped, Composite Ceramic Nd:YAG/Sm:YAG Microchip Lasers

A diode edge-pump microchip laser has a unique pumping scheme for high power operation. Low thermal distorted, high power operation is possible. The configuration of the edge-pumped microchip laser is more flexible than the well-known, thin-disk laser because there is no need to keep free space in front of the active region for pumping. Then it is possible to arrange an optical switching element such as a Cr:YAG saturable absorber or a nonlinear material close to the core, and a very short laser cavity is possible. Figure 1 shows the schematic of the diode edge-pumped Nd:YAG/Sm:YAG composite all-ceramic microchip laser (active part). The central cylindrical core with a 2mm diameter is 1.5at% Nd doped ceramic YAG. To suppress the parasitic oscillation in the microchip, the core is surrounded by 5at% Sm doped ceramic YAG as an absorber at 1064 nm which is often used as an ASE absorber. The thickness of the microchip is 0.25 mm and bonded on a Cu-W heatsink. In free running operation, the microchip laser emitted 30 mJ at an absorbed pump power of 90 mJ using the output coupler (OC) with a concave curvature of 1 m and 90% reflectivity. In passively Q-switched operation, a pulse energy of 1.76 mJ with a pulse width of 1.5 ns was obtained at an absorbed pump power of 26 mJ by inserting a Cr:YAG saturable absorber with 80% initial transmission into the cavity. The cavity length is 6 mm and the repetition rate is 10 Hz.

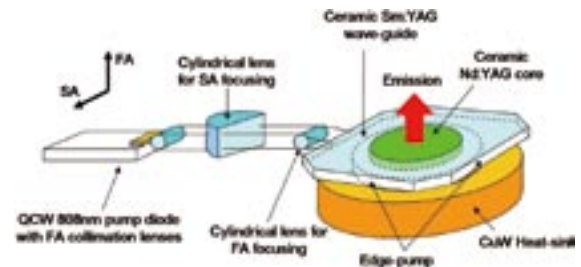


Figure 1. Diode edge-pumped Nd:YAG/Sm:YAG composite all-ceramic microchip laser.

## 2. Laser Oscillation of Nd<sup>3+</sup>-Doped Photo-Thermo-Refractive Glass under Diode Laser Pumping

The laser action of photo-thermo-refractive glass (PTR) that was the raw material of volume Bragg grating was demonstrated for the first time by introducing Nd<sup>3+</sup>. An uncoated Nd:PTR generated continuous-wave laser output of 124 mW with a slope efficiency of 25% by laser diode pumping. Nd:PTR has a wide bandwidth of 27.8 nm and 16.0 nm for emission and absorption, respectively. This enabled Nd:PTR to perform wide bandwidth laser action at 1053.9–1063.3 nm, and to hold off the decrease of pump-absorption efficiency below 30% even under 3.5-nm shift of pump wavelength from its absorption center.

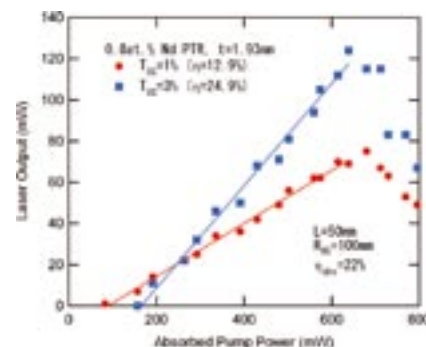
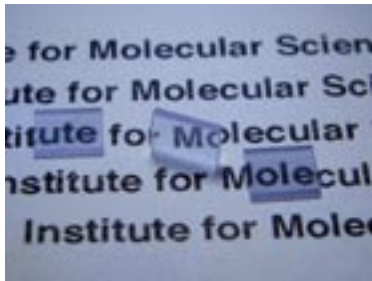


Figure 2. Laser performance of 0.8at.% Nd:PTR with output coupling of 1% and 3%.



### 3. Development of Anisotropic Transparent Ceramics for Laser Media

Trivalent-rare-earth-ion-doped ( $\text{RE}^{3+}$ -doped) transparent ceramic materials have attracted much attention as next-generation multifunctional, high-power laser gain media because they have excellent scalability and flexibility. However, fabrication of a laser-grade anisotropic (non-cubic) ceramic medium by the conventional sintering process is not possible because optical scattering occurs at randomly oriented grain boundaries. In this research, we developed a  $\text{RE}^{3+}$ -assisted magnetic orientation method and applied it for fabrication of ceramic Nd:FAP and Yb:FAP ( $\text{Ca}_{10}(\text{PO}_4)_6\text{F}_2$ , hexagonal) that have excellent optical properties such as high absorption efficiency, high emission cross-section and long emission lifetime. We successfully improved the transparency of anisotropic ceramics with loss coefficient  $<1.5 \text{ cm}^{-1}$  by optimization of material processing parameters.



**Figure 3.** Highly oriented  $\text{Nd}^{3+}$  doped fluorapatite transparent ceramics (0.5mm thickness) obtained by slip casting under 1.4T magnetic field and subsequent sintering process

### 4. High Energy Quasi-Phase Matched Optical Parametric Oscillation Using Mg-Doped Congruent $\text{LiTaO}_3$ Crystal

We report on high energy optical parametric oscillation of 118 mJ output with  $\sim 70\%$  slope efficiency in 10 ns duration of 30 Hz operation by using Mg-doped congruent composition  $\text{LiTaO}_3$  (MgLT). The periodically poled MgLT device with  $\sim 30 \mu\text{m}$  period for quasi-phase matching (QPM) in 5-mm-thick crystal are prepared. MgLT crystal could become a candidate for high-energy and higher durability material of QPM device, compared to conventional Mg-doped congruent composition  $\text{LiNbO}_3$ .

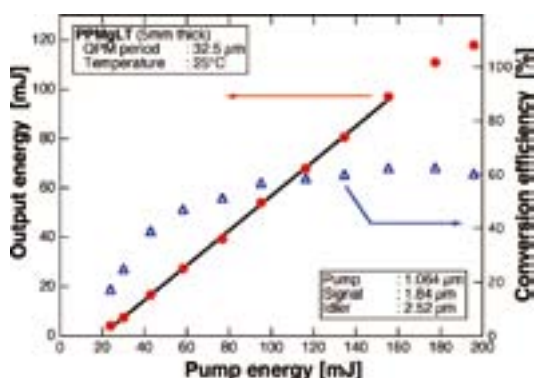


**Figure 4.** Dependence of total OPO output energy and conversion efficiency on input pump energy.

### 5. Passively Q-Switched Nd:YAG/ $\text{Cr}^{4+}$ :YAG Laser with Performances Controlled a Volume Bragg Grating

The large peak emission cross-section of Nd:YAG limits the maximum energy of a passively Q-switched Nd:YAG/ $\text{Cr}^{4+}$ :YAG laser equipped with a normal output coupler (OCM), which typically has a reduced wavelength selectivity. We demonstrated a diode end-pumped, high-peak power, passively Q-switched Nd:YAG/ $\text{Cr}^{4+}$ :YAG laser and controlled its performances with a volume Bragg grating (VBG). The laser pulse energy was increased significantly (by a factor of two or more) by elevating Nd:YAG temperature and locking the emission wavelength ( $\lambda_{\text{em}}$ ) with the VBG. Furthermore, wavelength  $\lambda_{\text{em}}$  was tuned by changing the VBG temperature, while maintaining ns-order short laser pulses of mJ-level energy.

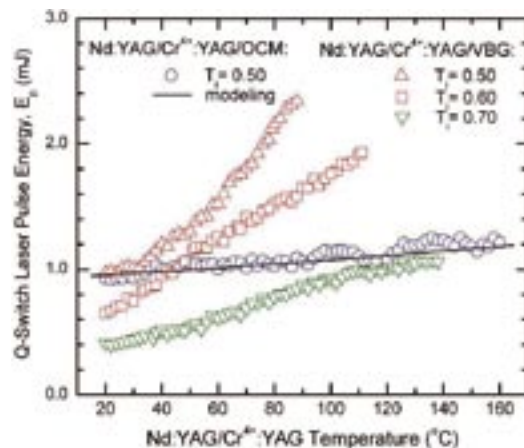


**Figure 5.** Q-switch laser pulse energy versus temperature of Nd:YAG/ $\text{Cr}^{4+}$ :YAG crystals.  $\text{Cr}^{4+}$ :YAG of various initial transmission  $T_i$ ; output coupling mirror with transmission  $T = 0.70$ ; VBG at  $20^\circ\text{C}$ .

### References

- 1) M. Tsunekane and T. Taira, *Tech. Digest of Europhoton 2010* WeP8 (2010).
- 2) Y. Sato, T. Taira, V. Smirnov, L. Glebova and L. Glebov, *Tech. Digest of Conf. on Lasers and Electro-Optics (CLEO2010)* CTuJ-4 (2010).
- 3) J. Akiyama and T. Taira, *OSA Topical Meeting on Advanced Solid-State Photonics 2010* AtuB3 (2010).
- 4) H. Ishizuki and T. Taira, *Opt. Express* **18**, 253–258 (2010).
- 5) N. Pavel, M. Tsunekane and T. Taira, *Opt. Lett.* **35**, 1617–1619 (2010).

# Ultrafast Laser Science

Laser Research Center for Molecular Science  
Division of Advanced Laser Development



FUJI, Takao  
MASUDA, Michiko

Associate Professor  
Secretary

Speed of ultrafast energy transfer from light to molecules (*i.e.* primary processes of photosynthesis, photoisomerization in visual pigments, *etc.*) is on the order of femtosecond ( $10^{-15}$  s). In our laboratory, we develop cutting edge lasers for such ultrafast molecular science, namely, femtosecond or attosecond ( $10^{-18}$  s) ultrashort pulse lasers.

For example, arbitrary waveform synthesis can be performed with simultaneous generation of femtosecond light pulses in various wavelength regions and superimposition of them with precisely controlled phases.

We would like to develop such advanced light control technology, which can push forward the research on ultrafast photochemical reactions.

I have just joined IMS since February 2010. Currently I am setting up my laboratory. In this review article, I introduce my previous works in RIKEN where I was working until the end of January 2010.

## 1. Experimental and Theoretical Investigation of a Multicolor Filament<sup>1)</sup>

Gas media, which are transparent and low dispersion in much wider range than solid media, are useful for frequency conversion of femtosecond pulses beyond the wavelength region from 0.4 to 2  $\mu\text{m}$  with keeping the pulse width short ( $<30$  fs). However, efficient frequency conversion was difficult since the nonlinearity of gas media is much smaller than that of solid media.

Recently, we have developed nonlinear frequency conversion scheme with the use of self-guiding effect of intense ultrashort pulses, namely, filamentation. By gently focusing second harmonic (400 nm,  $\omega_{\text{SHG}}$ , 0.5 mJ) and fundamental (800 nm,  $\omega_{\text{FUN}}$ , 0.5 mJ) of Ti:Sapphire laser pulses into gases, nondegenerate four-wave mixing  $\omega_{\text{SHG}} + \omega_{\text{SHG}} - \omega_{\text{FUN}} \rightarrow \omega_{\text{fwm}}$  and cascading  $\omega_{\text{fwm}} + \omega_{\text{SHG}} - \omega_{\text{FUN}} \rightarrow \omega_{\text{cas}}$  through filamentation occurred and resulted in an efficient frequency conversion to 260 nm ( $\omega_{\text{fwm}}$ , 16  $\mu\text{J}$ ) and 200 nm ( $\omega_{\text{cas}}$ , 4  $\mu\text{J}$ ). The pressure dependence of the conversion efficiency cannot be explained by a one-dimensional model, but calculation of multicolor filament by a three-dimensional model was suc-

cessful. The simulation result indicates a broad scalability of the scheme for frequency conversion of ultrashort pulses.

These two pulses were compressed by grating-based compressors sharing the same grating. The pulse widths were characterized to be 14 fs (260 nm, 4.7 eV) and 17 fs (200 nm, 6.3 eV) using a dispersion-free transient-grating frequency-resolved optical gating (TG-FROG). The results are shown in Figure 1. The energies of 260 and 200 nm pulses after the compression were 2.5  $\mu\text{J}$  and 0.5  $\mu\text{J}$ , respectively.

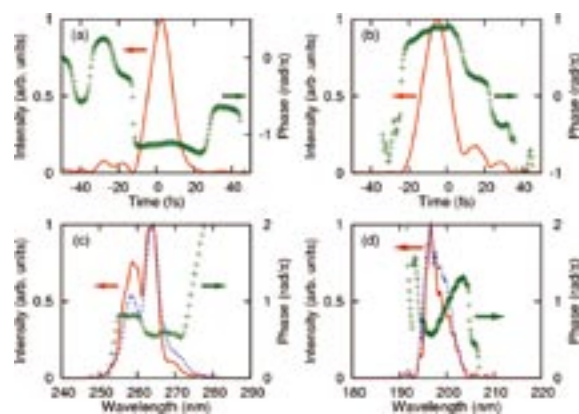


**Figure 1.** The retrieved 260 nm and 200 nm pulses obtained with TG-FROG. (a) 260 nm; time domain. (b) 200 nm; time domain. (c) 260 nm; frequency domain. (d) 200 nm; frequency domain. Solid lines show intensities and cross dots show phases. Dotted lines in the frequency-domain figures are the spectra measured by a spectrometer directly.

## 2. Time-Resolved Photoelectron Imaging of Ultrafast Internal Conversion through Conical Intersection in Pyrazine<sup>2)</sup>

The ultrashort UV pulses generated by using four-wave mixing through filamentation were used for time-resolved photoelectron imaging spectroscopy. The experimental setup is shown in Figure 2. The time resolution of the experiment was determined to be 22 fs by cross correlation of the pump and probe pulses in situ. By using the pump-probe photoelectron

imaging apparatus, a nonadiabatic electronic transition through a conical intersection in the benchmark polyatomic molecule of pyrazine was studied. The lifetimes of the  $S_2$  and  $S_3$  states of pyrazine were determined to be  $22 \pm 3$  fs and  $41 \pm 2$  fs, respectively, by the global fitting of the time-energy maps of photoelectron kinetic energy (PKE) distributions. Quantum beat with an approximately 50 fs period was observed after the  $S_2 \rightarrow S_1$  internal conversion, which was attributed to the totally symmetric vibration  $\nu_{6a}$  in  $S_1$  (see Figure 3).

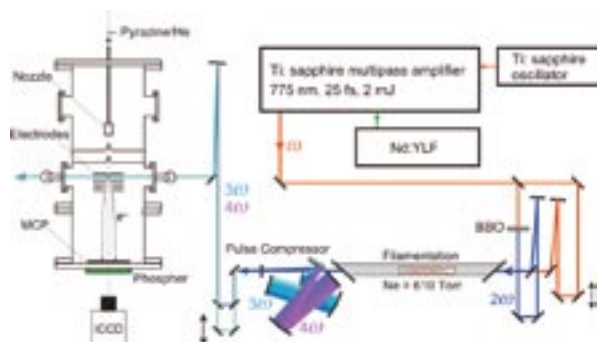


Figure 2. Schematic of the experimental setup.

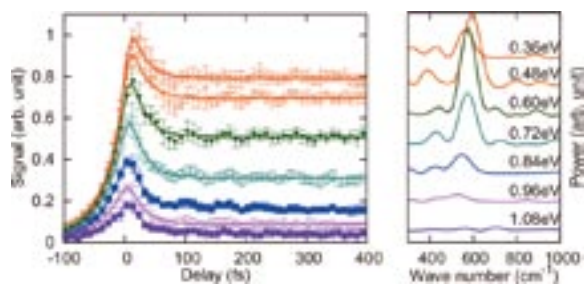


Figure 3. Time evolutions of photoelectron intensities at selected PKE subsections of pyrazine. The oscillatory features are due to the vibrational wave-packet motion along  $Q_{6a}$ . The solid lines show the results of the global fitting. Fourier power spectra of oscillatory components of photoelectron signal intensities after a delay time of 70 fs are also shown on the right panel.

### 3. Spectral Phase Transfer to Ultrashort UV Pulses through Four-Wave Mixing<sup>3)</sup>

It is very meaningful to have ultrashort VUV pulses at photoelectron spectroscopy for molecules since deactivation processes to the ground state can be explored by a probe pulse with high photon energy. Replacing the fundamental pulse in the previous scheme to output of a near infrared optical parametric amplifier, we attempted to generate pulses with shorter wavelength ( $<200$  nm). Second harmonic of Ti:Sapphire laser output (400 nm,  $\omega_{\text{SHG}}$ , 0.35 mJ) and near infrared pulses (1200 nm,  $\omega_{\text{NIR}}$ , 0.2 mJ) from a noncollinear optical parametric amplifier were gently focused into neon gas, and ultrashort pulses with the center wavelengths of 237 nm ( $\omega_{\text{fwm}}$ ) and 167 nm ( $\omega_{\text{cas}}$ ) were produced by four-wave mixing processes,  $\omega_{\text{SHG}} + \omega_{\text{SHG}} - \omega_{\text{NIR}} \rightarrow \omega_{\text{fwm}}$  and  $\omega_{\text{fwm}} + \omega_{\text{SHG}} - \omega_{\text{NIR}} \rightarrow \omega_{\text{cas}}$ , respectively. The spectra of the generated pulses are shown in Figure 4. The energy of the generated 237 nm

pulse was approximately 1.5  $\mu\text{J}$  whereas that of the 167 nm pulse were estimated to be less than 100 nJ. The reason for the lower efficiency than the previous scheme would be mode quality of NOPA output and/or phase matching condition of the nonlinear mixing. Coherence length of the phase matching ( $1/\Delta k$ ) is half of the previous four-wave mixing process.

Transfer of spectral phase from the near infrared ultrashort pulses to the UV pulses through the four-wave mixing process was also demonstrated. Assuming monochromatic second harmonic, the even order spectral phase of the near infrared pulse is transferred to the UV pulse with the opposite sign, whereas the odd order spectral phase is transferred with the same sign in principle. We controlled the spectral phase of the NIR pulses by prism insertion of a SF10 prism compressor, and measured spectral phases of the NIR pulses and the generated UV pulses by using FROG. The experimental results are shown in Figure 5. The convexities (up or down) of the spectral phase at the main part of the spectrum are opposite with each other suggesting chirp directions of the pulses are opposite with each other. Concerning the TOD, high frequency components present larger concavity compared with low frequency components in both cases. Therefore, the sign of the TOD was kept the same. A positively chirped near infrared pulse was used for generating a negatively chirped UV pulse, which was compressed down to 25 fs by a magnesium fluoride window. In principle, the spectral phase transfer scheme can also be applied to the chirp control of the generated VUV pulses.

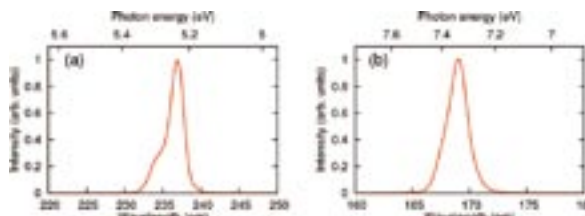


Figure 4. Typical spectra of (a) UV and (b) VUV pulses generated through the four-wave mixing and the cascaded process, respectively.

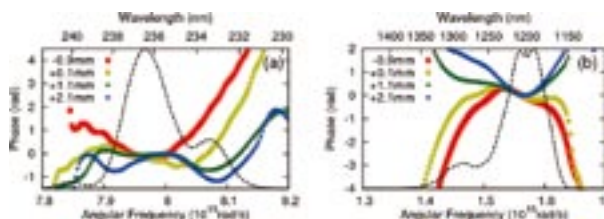


Figure 5. Spectral phases of (a) UV and (b) corresponding NIR pulses at each prism insertion. Intensity of each pulse is also shown as a dashed curve.

### References

- 1) T. Fuji, T. Suzuki, E. E. Serebryannikov and A. Zheltikov, *Phys. Rev. A* **80**, 063822 (2009).
- 2) Y.-I. Suzuki, T. Fuji, T. Horio and T. Suzuki, *J. Chem. Phys.* **132**, 174302 (2010).
- 3) P. Zuo, T. Fuji and T. Suzuki, *Opt. Express* **18**, 16183 (2010).

# Visiting Professors



Visiting Professor  
**KODAMA, Ryosuke** (from *Osaka University*)

### High Energy Density Sciences

Now it is relatively easy to realize high energy density states with high power lasers. The states would have a variety of attractive fields of sciences and technologies such as particle acceleration, laboratory astrophysics, and material science, nuclear science including medical applications and laser fusion, which is "High Energy Density Science: HEDS." One of the advantages of the HED states is its energy density, which is much higher than that of the solid state matter. He is now exploring high energy density sciences in methods of introducing a Plasma Photonics concept to control intense light and high energy charged particles with high energy density plasmas. Applying the novel geometry with plasma photonic devices, theoretical approach is being made on nonlinear optics in vacuum with super ultra-intense laser light as an extreme condition of the high energy density sciences. As his other important topics, he is interested in creation of high pressure condensed matter such as metallic solid hydrogen with high power lasers. Freezing of a higher energy density state or metallic Si have been already realized, extending the new scheme to more number of materials to have novel materials in hand, which have never seen on the earth.



Visiting Associate Professor  
**KERA, Satoshi** (from *Chiba University*)

### Electronic Structure of $\pi$ -Conjugated Organic Thin Film by Photoelectron Spectroscopy

To clarify the charge transport and injection mechanism in weakly-interacting organic molecular solids, ultraviolet photoelectron spectroscopy (UPS) is considered a conventional and novel powerful technique. Hole-vibronic coupling as well as intermolecular energy-band dispersion is important fundamental properties to reveal mysterious electric properties of organic molecular solids. Moreover, a quantitative analysis of the photoelectron angular distribution in angle-resolved UPS using photoelectron scattering theory gives us information on the molecular orbital character as well as bonding nature, leading important aspects on intermolecular and molecule-substrate interaction to electronic/spin configuration. Photoemission process related phenomena, *e.g.* scattering, interference and lifetime effect of photogenerated hole on a discrete and delocalized state of molecular orbital, are hot issue.



Visiting Associate Professor  
**UENO, Kosei** (from *Hokkaido University*)

### Nano-Imaging of Photocurrent Generation Locally Enhanced Optical Near-Fields

The development of a high-efficiency solar cell is critical in order to create a future realizing low-carbon society. To produce a solar cell with high photoelectric conversion efficiency, we need to develop a system that responds to wide spectrum of solar light, from visible to near-infrared wavelength. Nanoparticles of noble metals exhibit localized surface plasmons (LSPs) associated with enhancement of an electromagnetic field due to its localization in nanometric domains at the surface of nanoparticles. Recently, we demonstrated the plasmonic photoelectric conversion from visible to near-infrared wavelength without deteriorating photoelectric conversion by using electrodes in which gold nanorods are elaborately arrayed on the surface of TiO<sub>2</sub> single crystal. IQE measurements allowed us to elucidate the photo induced electron transfer from gold nanorods to TiO<sub>2</sub> resulting from the excitation of the LSPs is nonlinearly induced not only by optical antenna effects but also by electromagnetic field enhancement effects. To study the effect in detail, it is important to pursue where the photocurrent generation is locally enhanced at the gold nanoblocks. We are trying to measure a high-resolution image of the photocurrent generation using near field light as a local excitation source, which is obtained from an optical probe working on a near-field optical microscope.



Visiting Associate Professor  
**TAKAHASHI, Toshiharu** (from *Kyoto University*)

### Development of New Spectroscopic Methods Using THz Coherent Synchrotron Radiation

We are developing new spectroscopic techniques using a brilliant light source in the THz-wave region, *i.e.*, coherent synchrotron radiation (CSR) from short bunches of relativistic electrons. One is the technique of the scanning near-field transmission and reflection microscopy in the THz-wave region, where the high special resolution below the diffraction limit is available. On the other hand, the method of the THz pump-photoemission probe spectroscopy (PES) is also developing. Since the VUV radiation by the coherent harmonic generation (CHG) can be emitted using the laser pulse in UVSOR, the jitter-free pump-probe spectroscopy is possible with the THz-CSR. In order to perform these spectroscopic techniques, we are constructing a new CSR beamline in UVSOR.



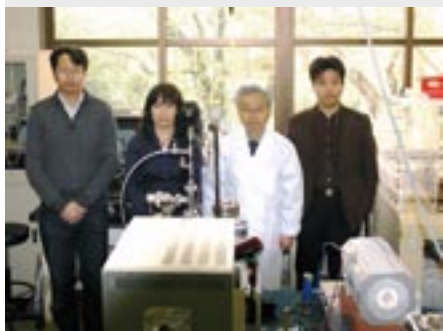
## RESEARCH ACTIVITIES

### Materials Molecular Science

Extensive development of new molecules, molecular systems and their higher-order assemblies is being conducted in the four divisions and in the research center for molecular scale nanoscience. Their electronic, optical and magnetic properties as well as reactivities and catalytic activities are being examined in an attempt to discover new phenomena and useful functions.

# Graphene-Walled Alveolate Carbon & Structures and Functions of Metal–Carbon Nano-Systems Made from Metal-Acetylides

Department of Materials Molecular Science  
Division of Electronic Structure



NISHI, Nobuyuki  
JUDAI, Ken  
NISHIJO, Junichi  
USUI, Chika

Professor  
Assistant Professor  
Assistant Professor  
Technical Fellow & Secretary

Metal acetylides or metal ethynyl molecules are made of the  $M^+-C^-$  ionic bonds. However, the ionic states of the acetylides are essentially metastable resulting in the segregation into metal-carbon or metal-organic polymer nanophases. Following to the invention of graphene-singlewalled Mesoporous Carbon Nano Dendrites (MCND) by evaporating silver from dendroid silver acetylide crystals, we have invented Graphene-multiwalled Alveolate Carbon (GAC), this time, and also 3D nanonets with GAC. These highly electron-conductive materials can be used for the electrodes of various next generation batteries.

## 1. Invention of Graphene-Multiwalled Alveolate Carbon for Novel Battery Electrodes

As demonstrated by the invention of graphene-walled Mesoporous Carbon Nano-Dendrites (MCND), metal-acetylides are well suited for generating nanostructured conductive materials. In contrast to silver acetylide, copper acetylide or methylethynyl copper normally produces wire-type crystals. Copper methylacetylide ( $Cu-C\equiv C-CH_3$ ) also produces wire type crystals bigger and longer than those of copper acetylide. Following to the thermal activation at 230 °C under hydrogen atmosphere, the wire crystals filled in a 300 mL beaker suddenly exhibit the violent segregation reaction producing copper nanocrystals in carbon and a gas mixture of methane and ethylene. A part of copper nanoparticles is removed by the treatment with nitric acid and the residual copper particles are removed at a temperature higher than 1150 °C. The density of the remaining carbon material is 2.07 g/cm<sup>3</sup> that is 4.2% smaller than that of graphite (2.16 g/cm<sup>3</sup>). Thermogravimetric Analysis showed a burning temperature as high as 682 °C: A little higher than that of MCND. The small angle X-ray scattering (SAXS) studies suggest that there are three types of the pores; the main part (69% in volume) has empty cores (an average size of 6 nm) surrounded with the shells of 0.83 nm

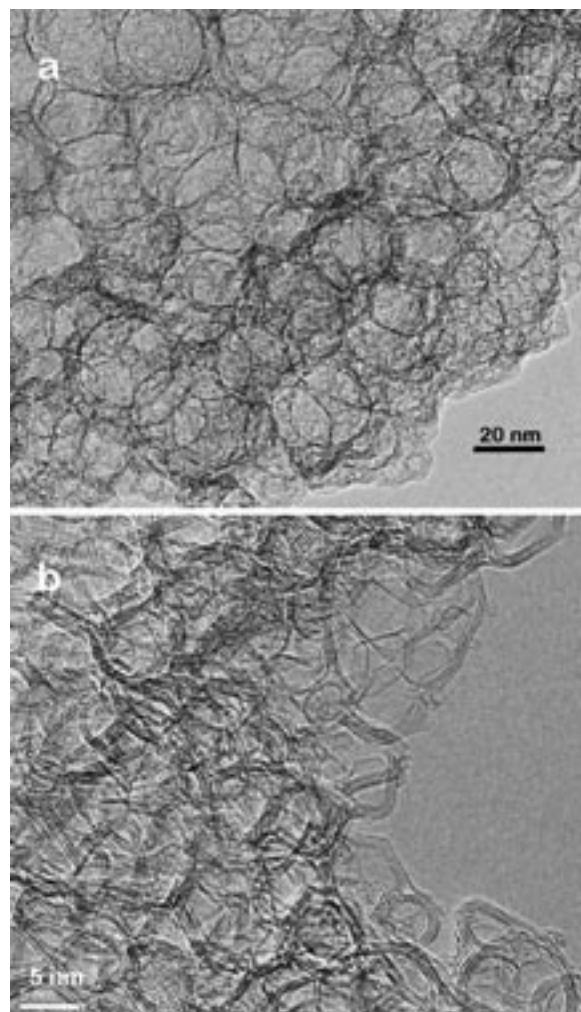


**Figure 1.** TEM images of a plate-type GAC treated at 1000 °C(a), and 1400 °C(b).

thickness on average, the second one has nearly the same core radii but much thicker shells (17 nm av.), and the third one has

an average pore size of 40 nm: Each of them is located in the edge area of plate type alveolates, branch-type alveolate rods, and in the middle of big plates, respectively. TEM images of the carbon are shown in Figure 1. Figures 1-a and 1-b show the main component of the plate-type GAC, and the TEM image of the second component showed graphene-multiwalled rod-like alveolate carbon. According to these morphology and various properties, we call this carbon “Graphene-multiwalled Alveolate Carbon (GAC).”

The escape pathways of copper allow other atoms or molecules to be stored in the pores. Thus we have succeeded to store Sn and Si nanocrystals in the pores. Lithium ion batteries with these materials as negative electrodes have exhibited electric capacities as high as 1200–1400 mAh/cm<sup>3</sup> and almost flat charge/discharge cycle performance.

## 2. In Situ Preparation and Catalytic Activation Method for Copper Nano-Particles from Acetylide Molecules

Metallic surface is too reactive to keep its original structure under usual atmosphere. In order to avoid oxidation and inactivation, we propose a facile preparation method for catalysts of metal nano-particles in situ. Copper acetylide (C<sub>2</sub>Cu<sub>2</sub>) molecules and copper methyl-acetylide (CuCC–CH<sub>3</sub>) molecules can be used as precursors of copper nano-particles. Figure 2 shows a High Resolution (HR)TEM image of which the nano-particle, atomically resolved lattice pattern was clearly observed. The space fringes detected in the HRTEM image are well matched with the *d* value (0.208 nm) of copper. The Cu nano-particle was covered with amorphous parts. The amorphous carbon layers can function as protection group for oxidation. Actually the metallic copper lattice could be observed even if the TEM specimen was exposed to air during transfer into the TEM apparatus. This means that the outer amorphous carbon could protect the reactive copper nano-particle from oxidizing by air.

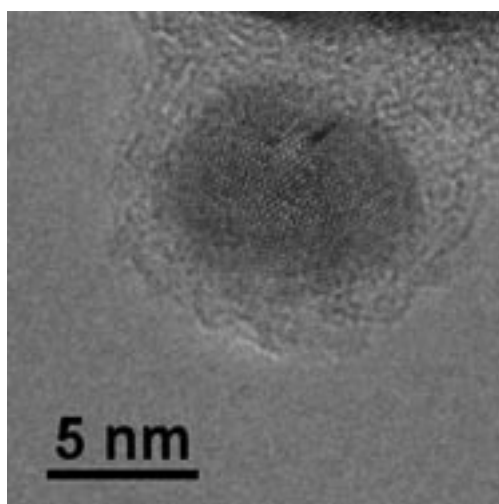


**Figure 2.** High-resolution transmission electron microscopic (HRTEM) image of annealed CuCC–CH<sub>3</sub> acetylide molecules.

## 3. Strong Intermolecular Interaction via Acetylide Ligands

Transition metal acetylide complex is the isoelectronic carbon analogue of a nitrile complex that is one of the representative building blocks of magnetic materials. In the previous work, we succeeded in constructing the first transition metal acetylide based magnets. However, in those cases, the acetylide ligand itself plays only a subsidiary role in the intermolecular spin–spin interactions because the ligand is placed too far from adjacent molecules to interact. That is, the appropriateness of an acetylide ligand for constructing a molecule based magnet remains unclear.

To evaluate the aptitude of an acetylide ligand for a magnetic material, we tried to construct new molecule-based magnetic materials based on [CrCyclam(C≡C–NaphOMe)<sub>2</sub>]<sup>+</sup> and TCNQ<sup>−</sup> (Figure 3a), where the Coulomb repulsion between a negatively charged acetylide ligand and an anion is weakened due to the large  $\pi$  orbital of a naphthyl group and the strong electron affinity of a TCNQ molecule. In consequence, a short contact between an acetylide ligand and a TCNQ anion is expected. The metathesis of [CrCyclam(C≡C–NaphOMe)<sub>2</sub>]OTf and Bu<sub>4</sub>N<sup>+</sup>TCNQ<sup>−</sup> in 1,2-dichloroethane (DCE) gives [CrCyclam(C≡C–NaphOMe)<sub>2</sub>](TCNQ)(DCE) (**1**), while the coexistence of a neutral TCNQ gives [CrCyclam(C≡C–NaphOMe)<sub>2</sub>](TCNQ)<sub>2</sub>(DCE) (**2**). The crystal structures of both salts are characterized by the one dimensional alternate stacking of cations and anions (TCNQ<sup>−</sup> for **1** or TCNQ<sub>2</sub><sup>−</sup> for **2**) as shown in Figure 3b, where naphthyl groups and TCNQ molecules are stacked face-to-face. The magnetic susceptibilities of the salts show good agreement with one dimensional  $S = [1/2, 3/2]$  ferrimagnetic model with the intra-chain interaction  $2J$  of −19.7 and −4.7 K for **1** and **2**, respectively. These strong interaction via an acetylide ligand evidence the usefulness of transition metal acetylides for a building block of molecule-based magnets.

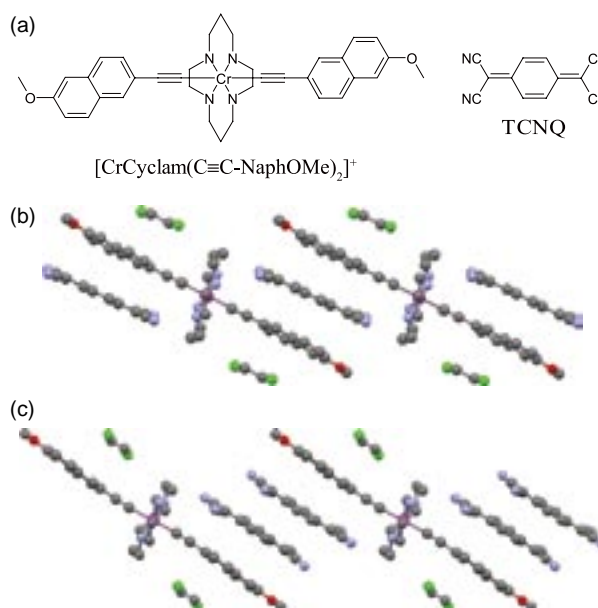


**Figure 3.** (a): Molecular structures, (b): Crystal structure of **1**, and (c): That of **2**.

# Characterization of Magnetic Ultrathin Films by Novel Spectroscopic Methods

Department of Materials Molecular Science  
Division of Electronic Structure



YOKOYAMA, Toshihiko  
NAKAGAWA, Takeshi  
TAKAGI, Yasumasa  
YAMAMOTO, Isamu  
ISAMI, Kyohei  
EGUCHI, Keitaro  
FUNAKI, Yumiko  
IWATA, Yumi

Professor  
Assistant Professor  
Assistant Professor  
Post-Doctoral Fellow  
Graduate Student  
Graduate Student  
Secretary  
Secretary

Novel properties of magnetic metal ultrathin films have been attractive both from fundamental interest and from technological requirements. We are especially interested in drastic modification of metal thin films by surface chemical treatment such as adsorption-induced spin transitions and morphological changes. The magnetic properties are characterized by means of several kinds of spectroscopic methods like MOKE (Magneto-Optical Kerr Effect) using UV-visible lasers and XMCD (X-ray Magnetic Circular Dichroism) using synchrotron radiation soft X-rays.

Moreover, we have been exploiting new techniques based on UV photoemission magnetic circular dichroism (MCD) such as ultrafast time resolved UV MCD photoelectron emission microscopy (PEEM) for spatiotemporal magnetic imaging.

## 1. Two Opposite Spin Reorientation Transitions in Fe-Covered Ni/Pd(111)<sup>1)</sup>

Magnetic anisotropy has widely been investigated in last decades, and especially perpendicular magnetic anisotropy has attracted much interest because of practical applications to high density recording media. We discovered two opposite spin reorientation transitions (SRTs) in Fe-covered Ni/Pd(111) magnetic films and investigated the origins of the two SRTs.

Pure Ni/Pd(111) films always show in-plane magnetization, irrespective of Ni thickness. Deposition of Fe 1 monolayer (ML) on Ni(6 ML)/Pd(111) causes a transition to perpendicular magnetization, and further Fe 3 ML deposition leads to a return to in-plane magnetization. The first SRT from in-plane to perpendicular magnetization is attributed to a large perpendicular orbital magnetic moment of a single Fe layer, which gives a significant impact on the Fe–Ni interface that stabilizes perpendicular magnetic anisotropy. The second SRT coincides with the structural change in the Fe film from the *fcc* to *bcc* phase, where the reduction in the orbital magnetic moment along the perpendicular direction suppresses the perpendicular magnetic anisotropy stability. It can be proposed that the origin of the second SRT to in-plane magnetization is attributed to

cooperative contributions of the structural transformation of the Fe film and the enhanced demagnetizing field.

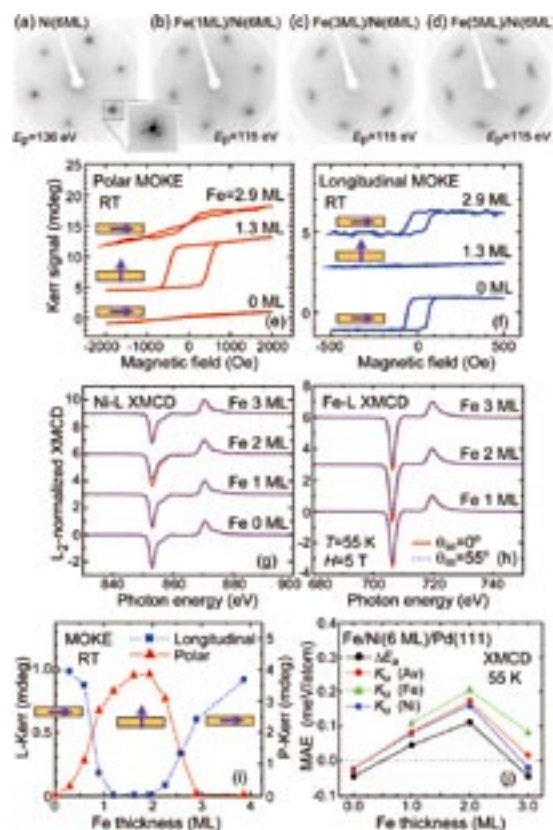


**Figure 1.** (a-d) Variation of LEED patterns of Fe/Ni(6ML)/Pd(111) during Fe deposition up to 5 ML. The structure of Fe changes to *bcc* around 3 ML. (e, f) Typical perpendicular (e) and in-plane (f) magnetization curves of Fe/Ni(6ML)/Pd(111) recorded by polar and longitudinal MOKE, respectively. (g, h) Ni (g) and Fe (h) L-edge XMCD spectra of Fe/Ni(6ML)/Pd(111). (i) Polar and longitudinal MOKE intensities of Fe/Ni(6ML)/Pd(111) as a function of Fe thickness. Two opposite SRTs occur at Fe 1 and 3 ML. (j) Magnetic anisotropy energies estimated by XMCD. The perpendicular magnetic anisotropy is maximized at Fe 2 ML.



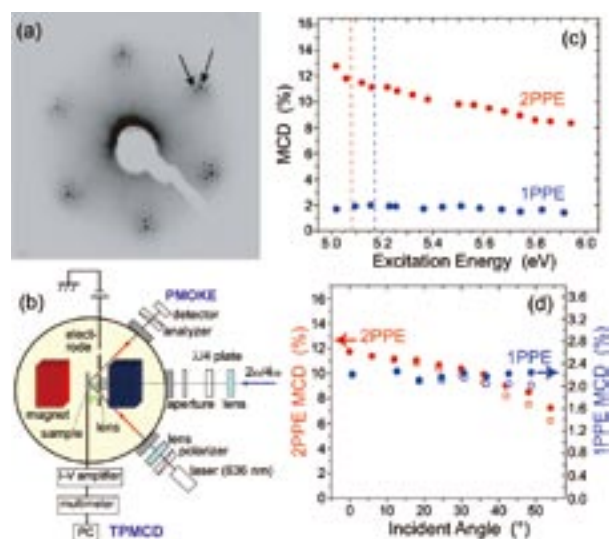
Figures 1(a-d) show low energy electron diffraction (LEED) patterns of Ni(6ML)/Pd(111) during Fe deposition. In Ni(6ML)/Pd(111), Moiré spots are clearly visible, implying that Ni is found to grow epitaxially but not pseudo-morphically on Pd(111) with maintaining the inherent Ni–Ni distance. For more than 3 ML Fe deposition, the fundamental spots are elongated, indicating the formation of *bcc* Fe. The structural transformation is concluded to take place around 3 ML Fe.

Figure 1(i) plots the polar and longitudinal MOKE (magneto-optical Kerr effect) intensities at room temperature. It is clearly found that two opposite SRTs occur at Fe 1 and 3 ML, between which the perpendicular magnetization is stabilized. Figures 1(g) and 1(h) exhibit Ni and Fe L-edge XMCD (X-ray magnetic circular dichroism) spectra, which provide spin and orbital magnetic moments and also the microscopic magnetic anisotropy constants as Figure 1(j). The perpendicular magnetic anisotropy is maximized at Fe 2 ML and is subsequently reduced at higher Fe coverage. The second SRT around 3 ML Fe can thus be ascribed to the structural transition to the *bcc* Fe phase, cooperated with the increase in the demagnetization field (shape anisotropy).

## 2. Observation of One- and Two Photon Photoemission Magnetic Circular Dichroism of Perpendicularly Magnetized Co/Pt(111)

In 2006, we discovered surprising enhancement of the UV-visible photoemission magnetic circular dichroism (MCD) from ultrathin Ni films on Cu(001) when the photon energy was tuned to the work function threshold.<sup>2)</sup> Based on this discovery, we succeeded in the first observation of UV MCD PEEM images of ultrathin magnetic films.<sup>3)</sup> This method allows us to perform in-laboratory MCD PEEM measurements instead of the usage of third-generation synchrotron radiation XMCD PEEM. Moreover, ultrafast UV MCD PEEM images were successfully obtained by using ultrashort pulsed lasers and a pump-and-probe technique.<sup>4)</sup> In 2009, we observed two-photon photoemission (2PPE) MCD and also 2PPE MCD PEEM images from Ni/Cu(001).<sup>5)</sup> The 2PPE technique is essentially important for the excitation of deeper valence levels such as semiconductors. In this work, we have exemplified noticeable superiority in 2PPE MCD compared to 1PPE MCD in another example of perpendicularly magnetized Co/Pt(111). This work has been performed under IMS international collaboration program with K. Hild, G. Schönhense and H. J. Elmers (Mainz Johannes Gutenberg-Universität, Germany), and with K. Tarafder and P. M. Oppeneer (Uppsala University, Sweden).

Figure 2(a) shows the LEED pattern of 4.5 ML Co grown on Pt(111). Additional spots can clearly be seen around the fundamental Pt(111) ( $1\times 1$ ) spots, which are ascribed to the Moiré patterns from the Co lattice. The Co film is thus found to grow epitaxially but not pseudomorphically on Pt(111). Figure 1(b) depicts the experimental setup. We employed a mode-locked tunable Ti:Sapphire laser (80 MHz, 2.5 W, 680–1020 nm, 100 fs) with the third and fourth-order harmonic



**Figure 2.** (a) LEED patterns of Co(4.5ML)/Pt(111). (b) 1PPE and 2PPE MCD measurement setup. (c,d) 1PPE and 2PPE MCD asymmetries of Co(4.5ML)/Pt(111) as functions of (c) excitation energy ( $h\nu$  and  $2h\nu$  for 1PPE and 2PPE, respectively) and (d) the laser incidence angle. The blue and red vertical lines are the work function thresholds, which are slightly different from each other, depending on the sample preparation.

generators. The photoemission from the sample was collected by the anode and the drain sample current was recorded. The sample Co(4.5ML)/Pd(111) shows perpendicular magnetic anisotropy with a coercive field of  $\sim 580$  Oe.

Figure 1(c) shows the 1PPE and 2PPE MCD asymmetries as a function of the excitation energy. At the work function threshold we obtain maximum values of 1.90% for 1PPE and 11.7% in the case of 2PPE, the latter being as much as 6.2 times larger, elucidating the efficiency of the 2PPE MCD. Figure 1(d) exhibits laser incidence angle dependence of the 1PPE and 2PPE MCD asymmetries. The 2PPE MCD asymmetry is found to be gradually reduced with the increase in the incidence angle, while for 1PPE there is almost no angle dependence observable. These behaviors are significantly different from those of Ni/Cu(001).<sup>5)</sup> The measured MCD asymmetries are discussed in two excitation models as well as on the basis of spin-polarized energy-band calculations. The ab initio calculated and measured 1PPE MCD responses are in good agreement. An explanation of the large 2PPE MCD signal is provided in terms of specific inter-band excitations.

## References

- 1) I. Yamamoto, T. Nakagawa, Y. Takagi and T. Yokoyama, *Phys. Rev. B* **81**, 214442 (2010).
- 2) T. Nakagawa and T. Yokoyama, *Phys. Rev. Lett.* **96**, 237402 (2006).
- 3) T. Nakagawa, T. Yokoyama, M. Hosaka and M. Katoh, *Rev. Sci. Instrum.* **78**, 023907 (2007).
- 4) T. Nakagawa, K. Watanabe, Y. Matsumoto and T. Yokoyama, *J. Phys.: Condens. Matter* **21**, 314010 (2009).
- 5) T. Nakagawa, I. Yamamoto, Y. Takagi, K. Watanabe, Y. Matsumoto and T. Yokoyama, *Phys. Rev. B* **79**, 172404 (2009).

# Advanced Design and In-Situ Characterization of Heterogeneous Catalyst Surfaces

Department of Materials Molecular Science  
Division of Electronic Structure



TADA, Mizuki  
MURATSUGU, Satoshi  
NAGAMATSU, Shin-ichi  
YANG, Yong  
WENG, Zhihuan  
MAITY, Niladri  
ISHIGURO, Nozomu  
KUSHIDA, Yuko  
WANG, Fei  
FUKUTOMI, Yukiyo  
UBAHARA, Wakana

Associate Professor  
Assistant Professor  
IMS Research Assistant Professor  
Post-Doctoral Fellow  
Post-Doctoral Fellow  
Post-Doctoral Fellow  
Graduate Student\*  
Graduate Student\*  
Technical Fellow  
Technical Fellow  
Secretary

## 1. Surface Structure and Catalytic Oxidation Mechanism of SiO<sub>2</sub>-Supported Ru Complex Catalyst

Chemical construction of heterogeneous catalyst surfaces on a molecular level toward selective catalysis has been still developing, and the attachment of metal complexes to oxide surfaces is one of the promising ways to create regulated metal structures grafted on oxide surfaces with unique catalytic properties. Stepwise structural transformations of supported metal complexes at surfaces, for instances, chemical grafting, selective ligand elimination, site isolation, surface functionalization, often produce molecularly regulated metal structures efficient for various catalytic reactions. In particular, chemical bonding between metal complexes and support surfaces is one of key issues to create novel metal structures, which are hard to obtain in homogeneous solutions, and anchoring metal complexes to support surfaces also prevents from catalyst deactivation through unfavorable aggregation of metal species under catalytic reaction conditions.

We have prepared a SiO<sub>2</sub>-supported Ru-monomer complex coordinating with a *p*-cymene ligand and found that the coordinating *p*-cymene ligand selectively released by an exothermic reaction using a reactant for oxidation reaction (isobutyraldehyde).<sup>1-3)</sup> The selective elimination of the *p*-cymene ligand produced a coordinatively unsaturated Ru center, whose structure is presented in Figure 1. The coordinatively unsaturated Ru complex supported on SiO<sub>2</sub> exhibited high activity for aldehyde oxidation and alkene epoxidation.<sup>2)</sup>

The SiO<sub>2</sub>-supported Ru-monomer complex achieved tremendous TONs (turnover numbers) for the selective oxidation of various aldehydes to corresponding carboxylic acids and alkenes to corresponding epoxides with good conversion and selectivity at ambient temperature, while the homogeneous Ru-precursor complex did not show good catalytic activity for both oxidation reactions. For examples, the TON of 38,800,000

for selective isobutyraldehyde (IBA) oxidation was achieved with the selectivity of 94% and the TON of 2,100,000 for *trans*-stilbene epoxidation using IBA/O<sub>2</sub> was achieved with the selectivity of 90%. Furthermore, the SiO<sub>2</sub>-supported Ru catalyst could be recycled by simple filtration and both conversion and selectivity were still constant for several runs. Ru K-edge EXAFS analysis after the selective oxidation reactions indicated the high stability of the SiO<sub>2</sub>-supported Ru complex catalyst under the catalytic oxidation conditions.

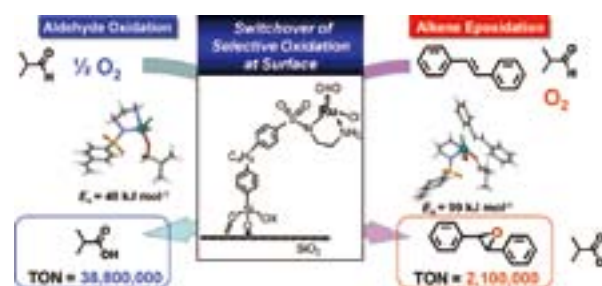


**Figure 1.** Switchover of selective catalytic oxidation reactions on the SiO<sub>2</sub>-supported Ru complex catalyst.

We also found that the IBA sole oxidation with O<sub>2</sub>, whose activation energy was 48 kJ mol<sup>-1</sup> and was much smaller than that of the *trans*-stilbene epoxidation using IBA and O<sub>2</sub> (99 kJ mol<sup>-1</sup>), was suppressed by the coexistence of *trans*-stilbene. During the catalytic epoxidation of *trans*-stilbene, co-existing IBA was stoichiometrically consumed for the epoxidation, and the facile IBA sole oxidation was found to be negligible. The switchover of the selective oxidation pathways from the IBA sole oxidation to the *trans*-stilbene epoxidation using IBA was explained in terms of energy profiles for the alternative selective oxidation pathways calculated by DFT, suggesting the preferential coordination of *trans*-stilbene to the active Ru complex at the surface.

## 2. Preparation, Characterization, and Shape-Selective Catalytic Performances of Molecularly Imprinted Ru-Complex Catalysts

Molecular imprinting of a supported metal complex whose ligand serves as a prescribed template is devoted to the design of shape-selective reaction space with a similar shape to the template. A molecularly imprinted cavity memorized the shape and coordination environment of the template ligand can be prepared on an unsaturated active metal center behind the template from the supported metal complex. We have designed and prepared a molecularly imprinted Ru-complex catalyst on SiO<sub>2</sub> and succeeded in regulating the regio- and shape-selective epoxidation of limonene.

A molecularly imprinted Ru-complex catalyst was prepared by step-by-step procedures: (1) the attachment of a Ru complex on SiO<sub>2</sub>, (2) the coordination of limonen-10-ol (template), which possesses a similar shape to an intermediate of terminal C=C bond epoxidation of limonene, (3) stacking of surface SiO<sub>2</sub>-matrix overlayers, and (4) the removal of the template ligand from the Ru site. The structures of the supported and molecularly imprinted Ru catalysts were characterized by solid-state NMR, FT-IR, XRD, XRF, UV/vis, BET, and Ru K-edge XAFS.

We found that the molecularly imprinted Ru catalyst designed for the terminal C=C bond epoxidation of limonene exhibited fine shape selectivity discriminating a methyl group of alkene reactants and high regioselectivity for the limonene epoxidation. Internal epoxide (62% selectivity) was preferably obtained on the supported Ru catalyst, while the molecularly imprinted Ru catalyst produced terminal epoxide of limonene with 63% selectivity. We found that the selectivity for the terminal epoxide increased to 90% and that for the internal epoxide decreased to 9% when SiO<sub>2</sub>-matrix overlayers were prepared by the addition of 1.0 wt% 3-(2-imidazolin-1-yl)propyltriethoxysilane to Si(OCH<sub>3</sub>)<sub>4</sub> (TMOS). The basic compound was suggested to promote the hydrolysis-polymerization of TMOS, as a result, fine imprinted cavity for the limonene epoxidation was suggested to be prepared.

We have also designed novel molecularly imprinted Ru catalysts for the asymmetric transfer hydrogenation of ketones. An NH<sub>2</sub> binding site was spatially arranged on the wall of

molecularly imprinted matrix overlayers as shown in Figure 2. A template ligand (**B**) with a carbamate moiety was coordinated to a SiO<sub>2</sub>-supported Ru complex (**A**). (**B**) is composed of three parts: (**a**) *o*-hydroxybenzhydrol moiety, which is a molecularly imprinted structure and has a similar shape to the product of *o*-fluorobenzophenone (*o*-F-BP), (**b**) a carbamate moiety (–NHCOO–), and (**c**) a 3-triethoxysilylpropyl (–Si(OC<sub>2</sub>H<sub>5</sub>)<sub>3</sub>) branch. Then, SiO<sub>2</sub>-matrix overlayers were stacked by the chemical vapour deposition and during the subsequent hydrolysis- polymerization of TMOS, the branch ((**B**)-(c)) was taken in the wall of the SiO<sub>2</sub>-matrix overlayers. Finally, the carbamate moiety ((**B**)-(b)) was broken to –NH<sub>2</sub>, CO<sub>2</sub>, and –OH, and then the coordination of (**B**)-(a) was removed to prepare the molecularly-imprinted Ru catalyst (**C**). The NH<sub>2</sub> binding site originally coordinated to the imprinted template (**B**)-(a) was fixed on the wall of the SiO<sub>2</sub>-matrix overlayers and is regarded to be coordinated to the F-substituent of *o*-F-BP by hydrogen bonding. The molecularly imprinted cavity acted as an efficient reaction space for the shape-selective transfer hydrogenation of *o*-F-BP.

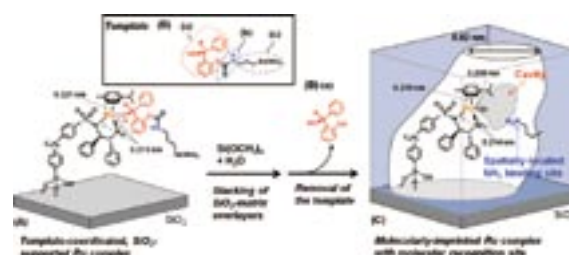


**Figure 2.** Design of a molecularly imprinted Ru-complex catalyst with a molecular binding site for asymmetric transfer hydrogenation of *o*-F-BP.

### References

- 1) M. Tada, Y. Akatsuka, Y. Yang, T. Sasaki, M. Kinoshita, K. Motokura and Y. Iwasawa, *Angew. Chem., Int. Ed.* **47**, 9252–9255 (2008).
- 2) M. Tada, S. Muratsugu, M. Kinoshita, T. Sasaki and Y. Iwasawa, *J. Am. Chem. Soc.* **132**, 713–724 (2010).
- 3) M. Tada, *Bull. Chem. Soc. Jpn.* **83**, 855–876 (2010) (Award Accounts).

### Awards

TADA, Mizuki; Presentation Award for Young Researcher (Catalysis Society of Japan).

TADA, Mizuki; 2010 The Young Scientist's Prize of The Commendation for Science and Technology by the Minister of Education, Culture, Sports, Science and Technology, Japan.

MURATSUGU, Satoshi; The 26<sup>th</sup> Inoue Research Award for Young Scientists (Inoue Foundation for Science).

MURATSUGU, Satoshi; CSJ Presentation Award 2010 (The Chemical Society of Japan).

MURATSUGU, Satoshi; The Royal Society of Chemistry Poster Prize (Japan-UK Symposium: Catalysis for a Sustainable World).

# Optical Studies of Charge Ordering in Organic Conductors

Department of Materials Molecular Science  
Division of Electronic Properties



YAKUSHI, Kyuya  
YAMAMOTO, Kaoru  
URUICHI, Miki  
YUE, Yue  
ABE, Hitomi

Professor  
Assistant Professor  
Technical Associate  
Post-Doctoral Fellow  
Secretary

In organic conductors, kinetic energy is comparable with on-site and inter-site Coulomb energy. Due to this reason, many organic conductors are located in a boundary area between metallic and localized states, and thus various organic charge-transfer compounds show metal–insulator phase transition. Recently, charge-ordered (CO) state originated from Coulomb interaction is widely found in organic conductors, and the electronic phase diagrams of typical organic conductors are re-considered taking CO into account. The CO state attracts much attention, first because charge-mediated superconductivity is theoretically predicted in superconducting compounds neighbored on CO phase, second because some compounds in CO phase show ferroelectricity through the crystallization of conduction electrons. We have investigated the CO state and metallic state near CO employing infrared and Raman, and reflection spectroscopy.

## 1. Nonuniform Site-Charge Distribution and Fluctuations of Charge Order in the Metallic State of $\alpha$ -(BEDT-TTF) $_2$ I $_3$ <sup>1</sup>

Among a variety of organic conductors, the  $\alpha$ -(BEDT-TTF) $_2$ I $_3$  shows rich properties such as charge order, superconductivity, zero-gap state, persistent photoconductivity, photo-induced phase transition, and non-linear optical response. This compound exhibits a first-order metal–insulator (MI) phase transition at  $T_{MI} = 135$  K. The MI transition is considered to be driven mainly by on-site and intersite Coulomb interaction. Based on theoretical,  $^{13}$ C-NMR, Raman, and x-ray studies, the insulating phase is regarded as a charge-ordered state involving a moderate structural change. First, we have quantitatively examined the amplitude of charge order below  $T_{MI}$  based on the rational assignment of the charge-sensitive C=C stretching modes. Compared with the insulating phase, the metallic phase of  $\alpha$ -(ET) $_2$ I $_3$  has not been thoroughly investigated, although the electronic structure of the metallic phase is related to the superconductivity under uniaxial strain, zero-gap state under hydrostatic pressure, and the excited state

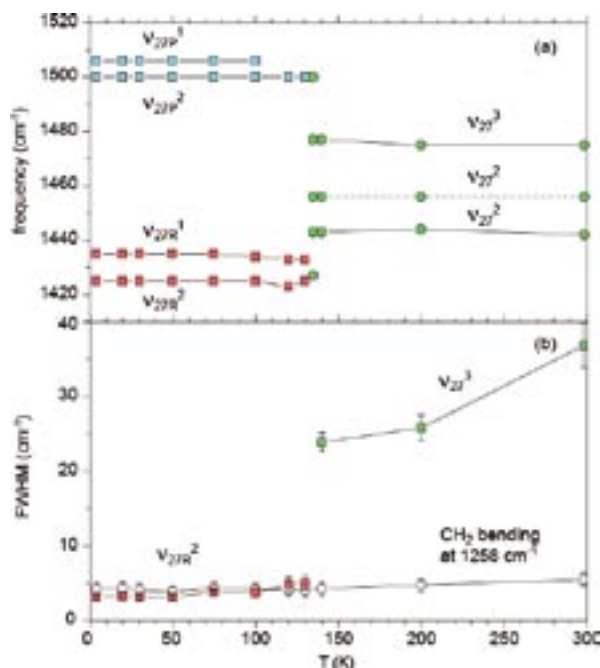


**Figure 1.** (a) Frequencies of  $v_{27}$  modes (C=C stretching) plotted against temperature. The three  $v_{27}$  mode largely split into two groups (charge-rich and charge-poor sites) (b) Temperature dependence of the linewidth (FWHM) of the  $v_{27}^3$  (green square) mode, which involves weak  $v_{27}^2$ , and  $v_{27R}^2$  (orange square) modes. The temperature dependence of the CH<sub>2</sub> bending mode (open circle) at 1258 cm<sup>-1</sup>, the frequency of which is insensitive to site charge, is shown for comparison.

of the photo-induced metal–insulator transition. Second, we have analyzed the linewidth of the charge-sensitive C=C stretching mode, and found a thermally activated short-range charge order in the metallic phase above  $T_{MI}$ .

Figure 1 shows the splitting and linewidth of the infrared-active charge-sensitive mode,  $v_{27}$ . Below  $T_{MI}$ , these modes are largely split into two groups, which correspond to the two charge-rich and two charge-poor sites. From the relationship

between the frequency and site charge, the site charge is deduced to be (0.8<sub>1</sub>, 0.7<sub>4</sub>, 0.2<sub>6</sub>, and 0.2<sub>3</sub>). The linewidth of these modes is narrow ( $\sim 4 \text{ cm}^{-1}$ ) as shown in Figure 1b. The large amplitude and narrow linewidth below  $T_{\text{MI}}$  unambiguously indicates the charge-ordered state with long-range order. In the metallic phase above  $T_{\text{MI}}$ , this mode is split into three. The site-charge is deduced to be (0.6<sub>8</sub>,  $\sim 0.6$ , and 0.4<sub>4</sub>). We interpret this small amplitude of site-charge distribution is caused by the distribution of transfer integrals. The most important difference between metallic and charge ordered phases is the linewidth as shown in Figure 1b. We interpret the very broad linewidth as the fluctuation of site charge. Assuming the Gaussian process for the fluctuation, the fluctuation rate was estimated to be  $1\text{--}25 \text{ cm}^{-1}$ . This slow fluctuation rate suggests a collective motion of short-range ordered charge-ordering stripe. We propose that several short-range ordered charge-ordering stripes are thermally activated in the metallic phase. This idea is consistent with the entropy driven first order MI phase transition. The optical conductivity in the metallic phase obtained from the analysis of reflectivity shows no Drude response, which may be associated with this fluctuation of charge order. According to the high-pressure experiment, this charge-ordering fluctuation is well suppressed.

## 2. Vibronic Activation of Vibrational Overtone in the Infrared Spectrum of Charge-Ordered Organic Conductors<sup>2)</sup>

Infrared spectrum provides us important knowledge on the valence states in strongly correlated systems. However, there is substantial difficulty in the analysis of the spectrum, because the valence electrons in these systems are affected by various interactions such as electron–electron or electron–phonons, complicating the interpretation of the spectral signals. For instance, even a phonon signal, which has the chemically defined frequency, is difficult to assign unambiguously because of large frequency-shift due to strong vibronic coupling.

In the study, we focused on the identification of the dip-shaped anomaly appearing in the infrared spectrum of a group of organic conductors (the highlighted region in Figure 2). The anomaly appears at approximately the same frequency (*ca.*  $2700 \text{ cm}^{-1}$ ), irrespective of the substances when they transform to charge-ordered phase. By the isotope-shift measurement performed for  $\theta\text{-(BEDT-TTF)}_2\text{RbZn(SCN)}_4$ , we found that there is a relevance of the anomaly to the overtone of a C=C stretching mode of BEDT-TTF molecule. From the fact that the dip is observed exclusively for the materials showing charge ordering, it is suggested that the anharmonicity activating the overtone does not exist in the potential of individual molecules; instead we suppose, which should be in the electronic potential formed by intermolecular vibronic interactions.

For organic conductors, the electronic potential depends strongly on molecular vibrations *via* the vibronic interaction called electron–molecular vibration (e–mv) coupling. The vibronic phenomenon has been explained within the frame-

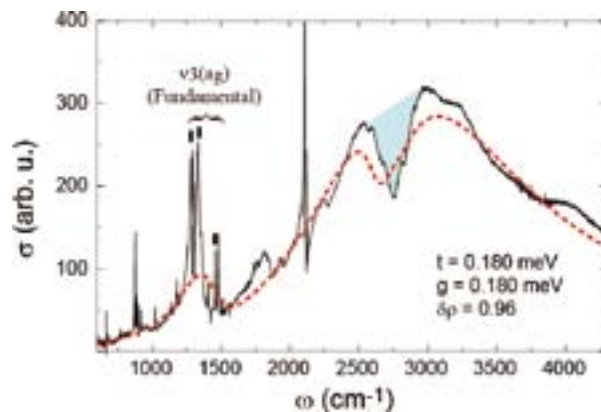


**Figure 2.** The comparison of the numerical result (dotted line) to the experimentally obtained optical conductivity of  $\theta\text{-(BEDT-TTF)}_2\text{RbZn(SCN)}_4$  [ $E//a$ ,  $T = 6 \text{ K}$ ] (solid line). (The parameters used in the calculations:  $\omega_{\text{neutral}} = 1494 \text{ cm}^{-1}$ ,  $\omega_{\text{cation}} = 1407 \text{ cm}^{-1}$ , line-width of molecular mode:  $100 \text{ cm}^{-1}$ , linewidth of electronic transition:  $1000 \text{ cm}^{-1}$ ,  $t = 180 \text{ meV}$ , e–mv coupling constant:  $180 \text{ meV}$ ) The highlighted region denotes the dip-shape anomaly, whereas the sharp peaks labeled by the ticks are the fundamental signals of  $\nu_3(a_g)$ .<sup>3)</sup>

work of a linear-coupling theory, in which the coupling effect is treated as an energy shift of the valence level. The aim of the present study is to extend the linear-coupling theory to explain the activation mechanism of the overtone of a vibrational mode that behaves otherwise a harmonic oscillator.

We calculated the corrections of the adiabatic electron potential due to the vibronic coupling to higher-ordered terms using a diatomic molecular dimer model. Additionally, the dynamic susceptibility was calculated using the same model. The main arguments derived from the study are summarized: (1) In the energy corrections, there appear two cubic terms—the lowest-order anharmonicity—in terms of the molecular coordinates. (2) One of them is connected with charge separation between the two molecules, which term presumably induces the anharmonicity activating the overtone. (3) The vibronically induced anharmonicity arises from the non-linearity in the adiabatic mixing of the electronic levels in accordance with charge separation. (4) Essential features of the experimentally obtained spectrum were reproduced by the numerical calculation of the dynamical susceptibility based on the cluster mode (Figure 2). (5) There is an intimate relationship between the activation of the overtone and nonlinear electric susceptibility; actually we have demonstrated that an organic conductor  $\alpha\text{-(BEDT-TTF)}_2\text{I}_3$ , which shows the overtone signal along with charge ordering, generates strong second-order optical nonlinearity.<sup>4)</sup>

## References

- 1) Y. Yue, *et al.*, *Phys. Rev. B* **82**, 075134 (2010).
- 2) K. Yamamoto, *et al.*, submitted.
- 3) K. Yamamoto *et al.*, *Phys. Rev. B* **65**, 085110 (2002).
- 4) K. Yamamoto, *et al.*, *J. Phys. Soc. Jpn.* **77**, 074709 (2008).

# Magnetic Resonance Studies for Molecular-Based Conductors

Department of Materials Molecular Science  
Division of Electronic Properties



NAKAMURA, Toshikazu	Associate Professor
FURUKAWA, Ko	Assistant Professor
IWASE, Fumitatsu	IMS Fellow
SUGIURA, Koichi	Graduate Student
ABE, Hitomi	Secretary

Magnetic resonance measurements are advantageous for studying fundamental electronic properties and for understanding the detailed electronic structures of molecular based compounds. Developing an understanding of the electronic phases and functionality of these materials enables us to perform systematic investigations of low-dimensional, highly-correlated electron systems and functional materials. Competition between the electronic phases in molecular-based conductors has attracted much attention. The investigations of such electronic phases by magnetic resonance measurements are important to understanding unsolved fundamental problems in the field of solid state physics, and to explore novel functionalities in the field of material science.

In this study, we performed broad-line NMR and ESR measurements on molecular-based conductors to understand electron spin dynamics and functionality in low-temperature electronic phases.

## 1. Anomalous Temperature Dependence of $g$ -Tensor in Organic Conductor, $(\text{TMTTF})_2\text{X}$ ( $\text{X} = \text{Br}, \text{PF}_6$ and $\text{SbF}_6$ )

The magnetic properties of organic conductor  $(\text{TMTTF})_2\text{X}$  ( $\text{X} = \text{Br}, \text{PF}_6$  and  $\text{SbF}_6$ ), where TMTTF is tetramethyltetrafulvalene, were examined by electron spin resonance (ESR) spectroscopy, X-ray diffraction (XRD) of the single crystals, and quantum-chemical calculation of the  $g$ -tensor. In the case of salts with bulky counter anions such as the  $\text{PF}_6$  and  $\text{SbF}_6$ , an anomalous temperature dependence of the  $g$ -tensor was observed in the temperature range from 20 K to 296 K. This anomalous behavior of the  $g$ -tensor signifies the rotation of the principal axes as well as the shift of the principal values. The  $g$ -tensor of the Br salt is, however, temperature independent. No remarkable change in the intra-molecular structure as a function of temperature was observed for all salts. On the other hand, the distance between TMTTF and counter-anion molecules obviously decreases as the temperature decreases for the  $\text{PF}_6$  and the  $\text{SbF}_6$  salts, while thermal contraction is not remarkable for the Br salt. In order to clarify the origin of the

anomalous behavior of the  $g$ -tensor, we investigated the possibility of deformation of the wave-function by the counter-anion potentials using a quantum-chemical calculation for the actual crystal structures measured at low-temperatures. In this paper, we describe the first direct observation of the deformation of the frontier orbital by the counter anion potential for organic conductors. The intra-molecular spin-distribution as a function of temperature also is discussed from the microscopic point of view.

## 2. Electronic Properties of a TMTTF-Family Salt, $(\text{TMTTF})_2\text{TaF}_6$ : New Member Located on the Modified Generalized Phase-Diagrams

A new TMTTF-family salt,  $(\text{TMTTF})_2\text{TaF}_6$ , which has the largest octahedral (Oh) symmetry counter anion among the various salts in the TMTTF family, was prepared. X-ray, static magnetic susceptibility, Electron Spin Resonance (ESR) and Nuclear Magnetic Resonance (NMR) measurements were carried out in order to investigate the electronic state of  $(\text{TMTTF})_2\text{TaF}_6$ . The unit-cell volume of  $(\text{TMTTF})_2\text{TaF}_6$  is larger than that of  $(\text{TMTTF})_2\text{MF}_6$  ( $M = \text{P}, \text{As}$  and  $\text{Sb}$ ).  $(\text{TMTTF})_2\text{TaF}_6$  shows the highest charge-ordering phase transition temperature ( $T_{\text{CO}} \sim 175$  K) among TMTTF salts with the Oh-symmetry counter anion. These facts indicate that  $(\text{TMTTF})_2\text{TaF}_6$  is located on the most negative side in the generalized phase-diagram for TMTCF family salts.  $(\text{TMTTF})_2\text{TaF}_6$  undergoes an antiferromagnetic transition around 9 K. It turned out the phase diagram needs to be modified.

## 3. Spin-Dynamics in Vicinity of Phase Transition for Organic Conductor $(\text{TMTTF})_2\text{X}$

The spin dynamics in the vicinity of the spin-gap phase transition for the organic conductor  $(\text{TMTTF})_2\text{PF}_6$  were examined by pulsed-ESR spectroscopy. An anomaly in the

relaxation time was observed in the intermediate region between the ground state and the high-temperature phase and was associated with the charge re-orientation originating in the transverse magnetic interaction. The calculation of the overlap integrals implied considerable inter-chain interactions. The transverse magnetic interaction plays an important role of the spin-gap phase transition in  $(\text{TMTTF})_2\text{PF}_6$ .

#### 4. Novel Type of Carrier Generated System: Magnetic Investigations of TTF-Based Self-Doped Hydrogen-Bonding Conductor

Magnetic investigations, including static magnetic susceptibility and high-field Electron Spin Resonance (ESR) measurements, were carried out for an organic conductor,  $(\text{TTF}^+\text{COO})[(\text{NH}_4^+)_{1-x}(\text{NH}_3)_x]$ . Anisotropic ESR parameters were determined for powder samples using a high-frequency W-band (93.9817 GHz) ESR spectrometer. The observed principal values of the  $g$ -tensor and quantum chemical calculation results indicate that the observed spin is distributed on quasi-hole-like TTF skeletons, and that the TTFCOO main-frame partially becomes a neutral radical. The temperature dependence of the spin susceptibility is well fitted with a Curie-Weiss term and an activation-type term, with the activation-type term dominant at high temperatures. The high absolute value of the spin susceptibility and the extremely small activation energy,  $\Delta$ , indicate that a quasi-degenerate (metallic) state is stabilized in  $(\text{TTF}^+\text{COO})[(\text{NH}_4^+)_{1-x}(\text{NH}_3)_x]$ , although the weakly temperature-dependent ESR linewidth indicates a localized characteristic. A novel type of carrier generation, self-doping, was discussed.

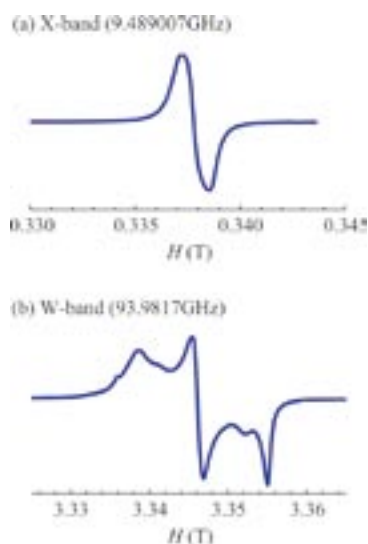


**Figure 1.** Typical ESR spectra for powder  $(\text{TTF}^+\text{COO})[(\text{NH}_4^+)_{1-x}(\text{NH}_3)_x]$  at 100 K using the (a) X-band (93.9817 GHz), and (b) W-band (93.9817 GHz), frequency regions.

#### Award

SUGIURA, Koichi; Tokai-Branch, Chemical Society of Japan Award.

#### 5. The Ground States and Critical Behavior in the Quasi-One-Dimensional Complexes $(\text{TMTTF})_2[(\text{AsF}_6)_x(\text{SbF}_6)_{1-x}]$

$^{13}\text{C}$  NMR measurements were carried out to understand the chemical pressure effect on the ground state in quasi-one-dimensional (1D) organic complexes using the alloy system  $(\text{TMTTF})_2[(\text{AsF}_6)_x(\text{SbF}_6)_{1-x}]$  ( $x \sim 0.3, 0.5, 0.67$ ). The temperature of the charge-ordering transition decreases with the concentration of  $\text{AsF}_6$ . Additional line splitting and the rapid increase in the spin-lattice relaxation rate,  $1/T_1$ , on cooling for the salt of  $x \sim 0.3$  indicates that the ground state of the salt is antiferromagnetic. In the  $x \sim 0.67$  alloy, the spin gap opens without antiferromagnetic spin correlations. The intermediate salt of  $x \sim 0.5$  is located in the vicinity of the quantum critical region between two phases at low temperatures. The quasi-1D correlation and antiferromagnetic critical behavior are discussed in terms of the power-law behavior of  $1/T_1$ .

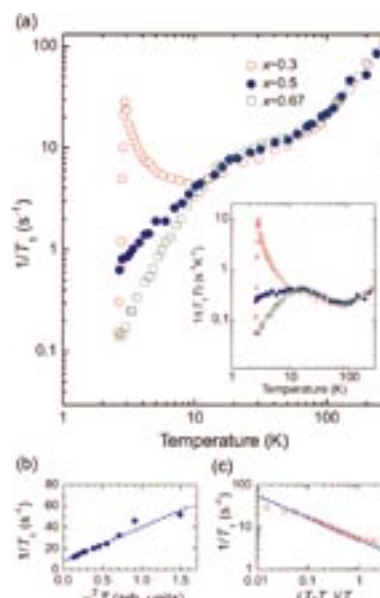


**Figure 2.** a) Temperature dependence of  $1/T_1$ . The inset shows the temperature dependence of  $1/(T_1T)$ . (b)  $1/T_1$  as a function of  $\chi_S^2 T$  for the alloy of  $x \sim 0.5$ . (c) Power-law behavior of  $1/T_1$  for the alloy of  $x \sim 0.3$  on approaching  $T_N$  by lowering temperature.

#### References

- 1) K. Furukawa, T. Hara and T. Nakamura, *J. Phys. Soc. Jpn.* **78**, 104713 (6 pages) (2009).
- 2) F. Iwase, K. Sugiura, K. Furukawa and T. Nakamura, *J. Phys. Soc. Jpn.* **78**, 104717 (7 pages) (2009).
- 3) K. Furukawa, T. Hara and T. Nakamura, *J. Phys. Soc. Jpn.* **79**, 043702 (4 pages) (2010).
- 4) K. Furukawa, T. Nakamura, Y. Kobayashi and T. Ogura, *J. Phys. Soc. Jpn.* **79**, 053701 (4 pages) (2010).
- 5) F. Iwase, K. Sugiura, K. Furukawa and T. Nakamura, *Phys. Rev. B* **81**, 245126 (6 pages) (2010).

# Conjugated Microporous Polymers— A New Class of Porous Frameworks for Function Design

Department of Materials Molecular Science  
Division of Molecular Functions



JIANG, Donglin  
KOU, Yan  
CHEN, Long  
XU, Yanhong  
DING, Xuesong  
FENG, Xiao  
SUZUKI, Hiroko

Associate Professor  
Post-Doctoral Fellow  
Post-Doctoral Fellow  
Graduate Student  
Graduate Student  
Graduate Student\*  
Secretary

Conjugated microporous polymers (CMPs) are a new class of porous materials with amorphous three-dimensional organic framework. Unlike other porous materials, CMPs are unique in that they enable the elaborate integration of  $\pi$ -electronic components to the covalent framework while retaining a permanent porous structure. Most studies on CMPs to date have focused on the development of synthetic approaches for the control of pore size and surface area. However, the functions of CMPs, apart from gas storage, have not yet been well explored. We have focused on the development of functional CMPs via molecular design of the CMP skeletons.

## 1. Light-Harvesting Conjugated Microporous Polymers: Rapid and Highly Efficient Flow of Light Energy with a Porous Polyphenylene Framework as Antenna

The molecular design of light-harvesting antennae requires not only the segregation of a large number of chromophore units in a confined nanospace but also the cooperation of these units in achieving highly efficient energy transduction. We have focused on the development of photofunctional CMPs with the expectation that the energy-donating CMPs with dense  $\pi$ -electronic components could serve as antennae for the collection of photons, while inherent pores within the framework could spatially confine energy-accepting counterparts, thus leading to the creation of an unprecedented donor-acceptor system for energy transduction mediated by the three-dimensional porous framework.

Here we report the synthesis and functions of a polyphenylene-based conjugated microporous polymer (Figure 1, PP-CMP). PP-CMP was recently designed and synthesized by Suzuki polycondensation reaction and used as antenna for the noncovalent construction of light-harvesting system. In contrast to linear polyphenylene, PP-CMP consists of conjugated three-dimensional polyphenylene scaffolds and holds inherent

porous structure with uniform pore size (1.56 nm) and large surface area ( $1083 \text{ m}^2 \text{ g}^{-1}$ ). It emits blue photoluminescence, is capable of excitation energy migration over the framework, and enables rapid transportation of charge carrier with intrinsic

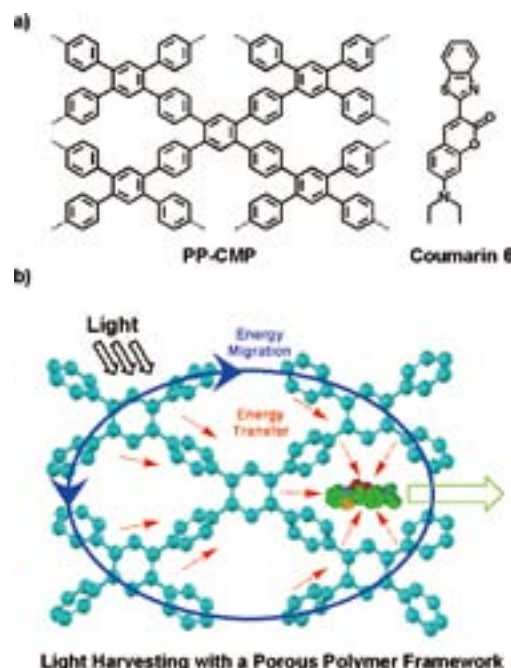


**Figure 1.** Schematic representations of (a) the synthesis and (b) the framework of PP-CMP (Structure is based on quantum calculation and crystal lattice parameters; Red: B, White: O, Blue: Pyrene; H atoms are omitted for clarity).

mobility as high as  $0.04 \text{ cm}^2 \text{ V}^{-1} \text{ s}^{-1}$ . The microporous structure of PP-CMP allows for the spatial confinement of energy-accepting coumarin 6 molecules in the pores and makes the high throughput synthesis of light-harvesting systems with designable donor-acceptor compositions possible. Excitation of PP-CMP skeleton leads to brilliant green emission from



coumarin 6, whose intensity is 21 fold as high as that upon direct excitation of coumarin 6 itself; while the fluorescence from PP-CMP itself is wholly quenched, as a result of energy transfer from the light-harvesting PP-CMP framework to coumarin 6. PP-CMP skeleton is highly cooperative with averagely 176 phenylene units working together to channel the excitation energy to one coumarin 6 molecule and features the energy transfer process with quick, efficient and vectorial character. These unique characteristics clearly originate from the conjugated porous structure and demonstrate the usefulness of CMPs in the exploration of  $\pi$ -electronic functions, in addition to their gas adsorption properties thus far reported. The light-harvesting antennae based on CMPs constitutes an important step for molecular optoelectronics based on porous polymeric materials.

## 2. CMPs as Scaffolds for Constructing Porous Catalytic Frameworks: A Built-In Heterogeneous Catalyst with High Activity and Selectivity Based on Nanoporous Metalloporphyrin Polymers

Recently, CMPs have been developed to load metal nanoclusters for the synthesis of heterogeneous catalysts. Because the polymer skeleton does not incorporate any catalytic sites, post treatment of CMPs via noncovalent interactions is a prerequisite for loading catalysts in the pores. In contrast to this approach, we are interested in the exploration of covalently built-in catalysis systems based on CMPs. If catalytic functionalities could be integrated into the skeleton of CMPs, one would have a chance to create a novel porous polymer in which the skeleton itself serves as the catalysts and the pores provide spaces for the transformation. Here we report a strategy for the synthesis of a new type CMP-based heterogeneous catalyst that consists of an inherent porous framework with built-in catalytic sites in the skeleton (Figure 2, FeP-CMP).

FeP-CMP was newly synthesized *via* a Suzuki polycondensation reaction and was developed as a heterogeneous catalyst for the activation of molecular oxygen to convert sulfide to sulfoxide under ambient temperature and pressure. FeP-CMP is intriguing because the polymer skeleton itself is built from catalytic moieties and serves as built-in catalysts, bears inherent open nanometer-scale pores that are accessible for substrates, and possesses high surface areas ( $1270 \text{ m}^2 \text{ g}^{-1}$ ) that facilitate the transformation reaction. It is highly efficient with high conversion (up to 99%) and large turnover number ( $\text{TON} = 97,320$ ), is widely applicable to various sulfides covering from aromatic to alkyl and cyclic substrates, displays high selectivity (up to 99%) to form corresponding sulfoxides, and is highly chemoselective for the oxidation of sulfide group even in the co-existence of other oxidative functionalities. Owing to the covalent linkages between catalytic sites in the frameworks, FeP-CMP can be recycled with good retention of its porous structure and allows for large-scale transformation. These unique characteristics clearly originate from the covalent

porous catalytic framework structure and demonstrate the usefulness of CMPs in the exploration of built-in heterogeneous catalysts, a new potential of these materials that have thus far been reported to exhibit noteworthy gas adsorption functions.

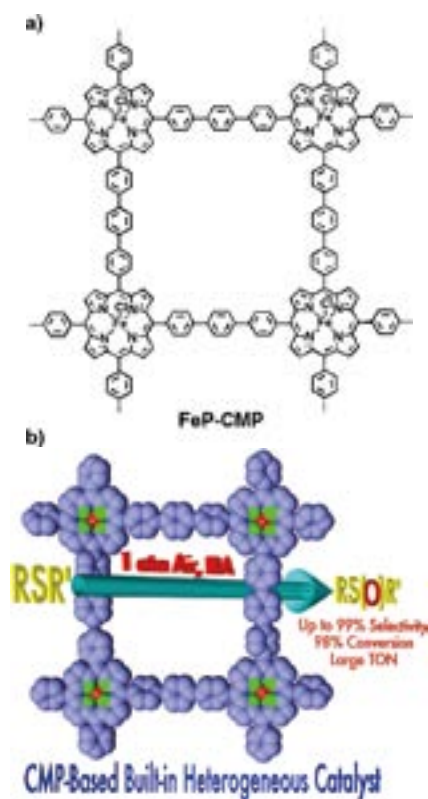


**Figure 2.** a) Schematic representation of the nanoporous polymer with metalloporphyrin built-in skeleton (FeP-CMP). b) Schematic representation of the transformation of sulfides to sulfoxides catalyzed by FeP-CMP.

Exploration of conjugated microporous polymers has a high probability of leading to the development of new functional materials. In summary, we developed a novel strategy for the construction of built-in catalysts based on CMPs architecture and demonstrated the utility of a newly synthesized FeP-CMP as a heterogeneous catalyst. A clear future potential for CMPs is to develop photocatalyst in which multiple functions including light-harvesting, energy transfer and catalytic processes can be seamlessly merged in one polymer skeleton. Therefore, the CMPs-based built-in catalyst constitutes a new step for the molecular design of heterogeneous catalyst systems.

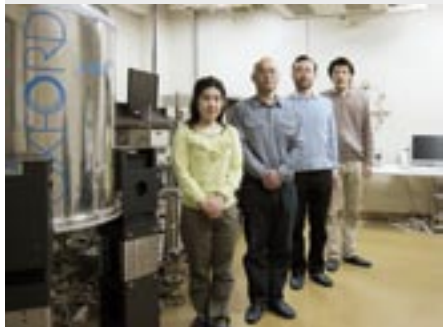
### References

- 1) L. Chen, Y. Honsho, S. Seki and D. Jiang, *J. Am. Chem. Soc.* **132**, 6742–6748 (2010).
- 2) L. Chen, Y. Yang and D. Jiang, *J. Am. Chem. Soc.* **132**, 9138–9143 (2010).

\* from Beijing Institute of Technology

# Structural Biology Based on Solid State NMR Spectroscopy

Department of Materials Molecular Science  
Division of Molecular Functions



NISHIMURA, Katsuyuki Associate Professor  
IIJIMA, Takahiro Assistant Professor  
TANIO, Michikazu IMS Research Assistant Professor

Solid state NMR is one of the useful tools to characterize dynamics and structures of molecules on amorphous condition without specific limitations. We are working on methodology developments of solid state NMR for structural biology and material science. Especially, we are focusing on elucidation of functions and dynamic structure of peripheral membrane protein bound to lipid bilayer surface based on solid state NMR. In the following, we show the new lipid sample system enabling magnetically aligned planer lipid bilayers useful for structural characterization of peripheral membrane proteins. In addition, a study of molybdenum compounds was reported.

## 1. Bicelle: Magnetically Aligned Planer Lipid Bilayers at Room Temperature for Structural Characterization of Membrane Bound Proteins by Solid State NMR

The properly hydrated mixture of saturated lipids possessing short and long acyl-chains at proper composition forms planer lipid bilayer so called bicelle which can be magnetically aligned under static magnetic field at temperature from 30 to 40 °C and widely used in solid state NMR for structural characterization of membrane associated proteins. Last year, we reported that addition of proper amount of phosphatidylinositol 4, 5-bisphosphate (PIP<sub>2</sub>) into bicelle significantly enhances the stability of magnetic alignment and increases its temperature range of magnetic alignment. Those effects were demonstrated for the bicelle proposed by Triba *et al.*, enabling magnetic alignment at room temperature. This bicelle composes mixture of saturated lipid 1,2-dimyristoyl-*sn*-glycero-3-phosphocholine (DMPC) and unsaturated lipid 1-palmitoyl-2-oleoyl-*sn*-glycero-3-phosphocholine (POPC) for long acyl chain, and 1,2-dihexanoyl-*sn*-glycero-3-phosphocholine (DHPC) for short acyl chain lipid, respectively.

In this study, we have identified the origin of enhancement of magnetic alignment due to addition of PIP<sub>2</sub> into bicelle.

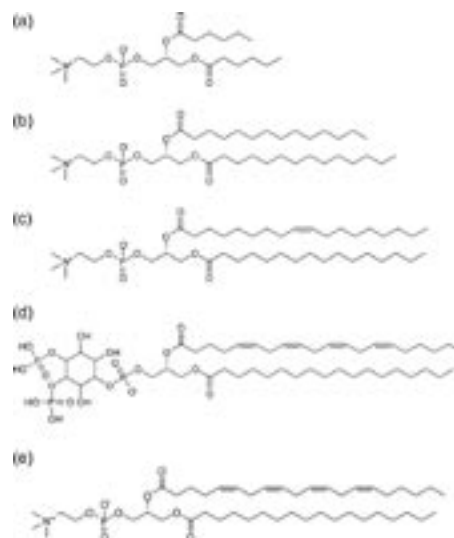


**Figure 1.** Molecular structures for (a) DHPC, (b) DMPC, (c) POPC, (d) PIP<sub>2</sub>, and (e) SACP, respectively.

Oriental properties of bicelles prepared from the different composition of lipids were verified based on <sup>31</sup>P-NMR. 1-stearoyl-2-arachidonoyl-*sn*-glycero-3-phosphocholine (SACP) has the polar head and the acyl chains as same molecular structure as those for DMPC and PIP<sub>2</sub>, respectively. The bicelle composing SACP instead of PIP<sub>2</sub> at same molar ratio was prepared in order to identify either polar head group or acyl-chains of PIP<sub>2</sub> contributing to the enhancement of magnetic alignment of bicelle. Figure 1 shows the <sup>31</sup>P-NMR spectra for the bicelle prepared from (a) PIP<sub>2</sub>/POPC/DMPC/DHPC, (b) POPC/DMPC/DHPC, and (c) SACP/POPC/DMPC/DHPC for the temperature range from 12 to 22 °C. The peaks around -3 and -11 ppm are originated from DHPC and POPC/DMPC mixture, respectively. The peak around -15.5 ppm is  $\delta_{\perp}$  edge of axially symmetric powder pattern of <sup>31</sup>P chemical shift anisotropy from multi lamella vesicles (MLVs). PIP<sub>2</sub>/

POPC/DMPC/DHPC-bicelle was magnetically aligned stably from 14 to 20 °C. In contrast, POPC/DMPC/DHPC-bicelle was magnetically aligned only at 16 °C. At 18 °C,  $\delta_{\perp}$  edge of axially symmetric powder pattern of  $^{31}\text{P}$  chemical shift anisotropy from MLVs was appeared. SAPC/POPC/DMPC/DHPC-bicelle exhibited insufficient magnetic alignment over measured temperature range.

From the comparison of  $^{31}\text{P}$ -NMR spectra for those bicelles, it is obvious that addition of SAPC into POPC/DMPC/DHPC-bicelle dose not enhance magnetic alignment. Thus we concluded that inositol 4, 5-bisphosphate residue in  $\text{PIP}_2$  may contribute to the enhancement of magnetic alignment of bicelle. Our results may give the way to design new reagents to enhance magnetic alignment of bicelle.

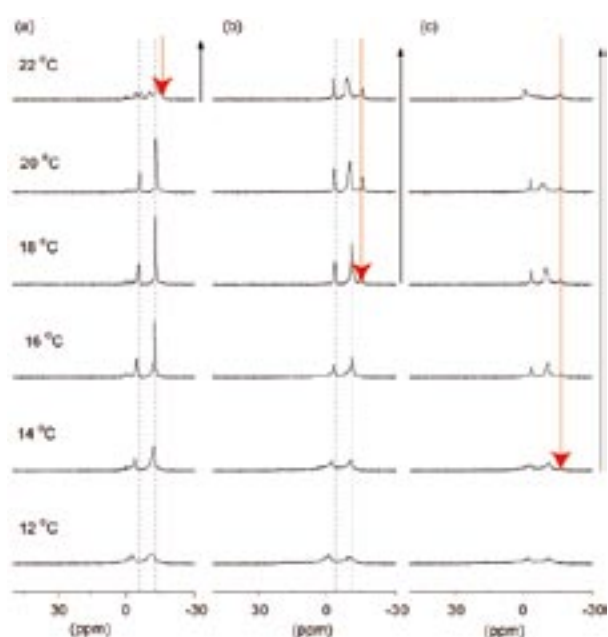


**Figure 2.**  $^{31}\text{P}$ -NMR spectra of magnetically aligned bicelle prepared from (a)  $\text{PIP}_2/\text{POPC}/\text{DMPC}/\text{PIP}_2/\text{DHPC}$ , (b)  $\text{POPC}/\text{DMPC}/\text{PIP}_2/\text{DHPC}$  and (c)  $\text{SAPC}/\text{POPC}/\text{DMPC}/\text{PIP}_2/\text{DHPC}$ , respectively. The red arrows indicate  $\delta_{\perp}$  edges of axially symmetric powder pattern spectra of  $^{31}\text{P}$  chemical shift anisotropy due to the formation of MLVs. Thus black arrows indicate the temperature range of the samples containing mixture of bicelle and MLVs.

## 2. Solid-State $^{95}\text{Mo}$ NMR of Polyoxomolybdates (V, VI) with $\epsilon$ -Keggin Structure

For molybdenum with the oxidation number of  $\text{Mo}^{0-}$ – $\text{Mo}^{\text{VI}}$ , solution-state  $^{95}\text{Mo}$  NMR has accessed all of integer oxidation number so far. In particular,  $^{95}\text{Mo}$  NMR of  $\text{Mo}^0$ ,  $\text{Mo}^{\text{II}}$  and  $\text{Mo}^{\text{VI}}$  has been widely used for study in the field of

coordination chemistry and reactivity. On the contrary, investigation of solid-state  $^{95}\text{Mo}$  NMR have been limited, because the spectra are broadened owing to the second-order quadrupole interaction. Recently, we have reported solid-state  $^{95}\text{Mo}$  NMR of  $\text{Mo}^{\text{V}}$  species for the first time by measuring high-field  $^{95}\text{Mo}$  NMR of mixed-valence polyoxomolybdates(V, VI) with localized or delocalized  $d^1$  electrons. It has been shown that the chemical shift of  $^{95}\text{Mo}$  NMR of  $\text{Mo}^{\text{V}}$  species exhibits a larger value than that of  $\text{Mo}^{\text{VI}}$ , and anisotropy of chemical shift depends on localization of  $d^1$  electrons.

In this work, we investigated molecular and electron structures by solid-state  $^{95}\text{Mo}$  and DFT calculation for a polyoxomolybdate crystal of  $[\text{PMo}_{12}\text{O}_{36}(\text{OH})_4\{\text{La}(\text{H}_2\text{O})_{2.75}\text{Cl}_{1.25}\}_4]27\text{H}_2\text{O}$  (abbreviated as  $\{\text{Mo}_{12}(\text{La})\}$ ), where a  $\{\text{Mo}_{12}\}$  core with the  $\epsilon$ -Keggin structure is capped with four  $\text{La}(\text{H}_2\text{O})_{2.75}\text{Cl}_{1.25}$ . Decimal fraction appears because of a disorder structure of  $\text{H}_2\text{O}$  and  $\text{Cl}$  coordinated to  $\text{La}^{\text{III}}$ . While potentiometric titration experiments have suggested that molybdenum is also disordered, only single Mo site was reported from analysis of X-ray diffraction. As shown in Figure 3,  $^{95}\text{Mo}$  static NMR spectra of  $\{\text{Mo}_{12}(\text{La})\}$  were measured under moderate (9.4 T) and ultrahigh magnetic fields (21.8 T). By simulation of the NMR spectra and density functional theory (DFT) calculation for isolated anions, NMR parameters for two molybdenum sites within the crystals were obtained. It was found that the  $d^1$  electrons in  $\{\text{Mo}_{12}(\text{La})\}$  are localized and used to form four  $\text{Mo}^{\text{V}}\text{--}\text{Mo}^{\text{V}}$  bonds.

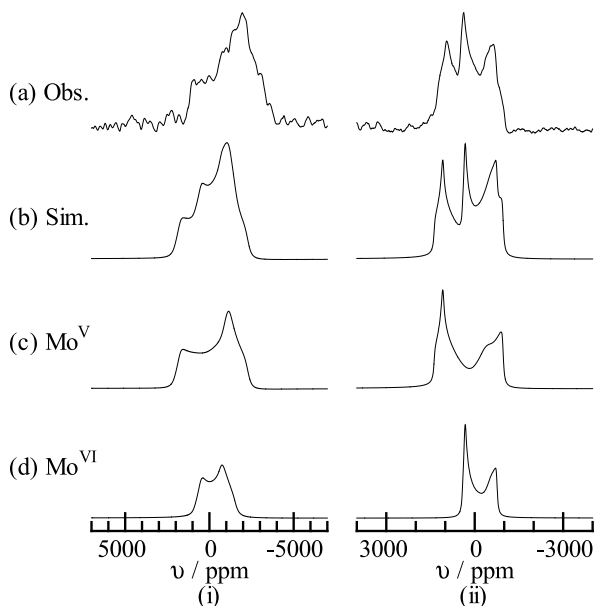
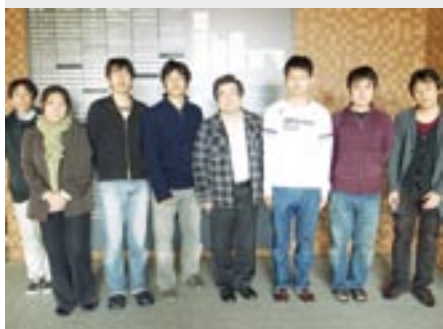


**Figure 3.**  $^{95}\text{Mo}$  NMR spectra of  $[\epsilon\text{-PMo}_{12}\text{O}_{36}(\text{OH})_4\{\text{La}(\text{H}_2\text{O})_{2.75}\text{Cl}_{1.25}\}_4]27\text{H}_2\text{O}$  under (i) 9.4 and (ii) 21.8 T. (a) and (b) show the observed and simulated spectra, respectively. (c) and (d) denote spectral components consisting of the spectrum (b).

# Organic Solar Cells

Research Center for Molecular Scale Nanoscience  
Division of Molecular Nanoscience



HIRAMOTO, Masahiro	Professor
KAJI, Toshihiko	Assistant Professor
IKETAKI, Kai	IMS Fellow
NAKAO, Satoru	Post-Doctoral Fellow
SHINMURA, Yusuke	Research Fellow
KUBO, Masayuki	Research Fellow
YOKOYAMA, Kazuya	Research Fellow
ISHIYAMA, Norihiro	Graduate Student
ANNEN, Sayuri	Secretary
MIYAWAKI, Makiko	Secretary

Organic solar cell is recognized as a future 3rd generation solar cell. Last year, we started CREST Project; “Bandgap Science for Organic Solar Cells.” Target of this project is 15% efficiency of organic solar cells by establishing bandgap science for organic semiconductors, which is equivalent to that for silicon semiconductor.

## 1. Carrier Concentration Determination for Organic Semiconductors by AC Hall Effect

We accomplished the world record conversion efficiency of 5.3% by using seven-nines (7N, 0.1 ppm, 99.99999%) purified fullerene.<sup>1,2</sup> Taking this result into consideration, determination technique of ppm-level concentrations of impurities in organic semiconductors is very important.

Hall effect measurement is well established for inorganic semiconductors. However, for high resistant organic semiconductors, reproducible results of Hall voltage of the order of  $\mu\text{V}$  has not been reported. In this study, we applied the AC

Hall effect technique to metal-free phthalocyanine ( $\text{H}_2\text{Pc}$ ) film and succeeded to obtain the first reproducible results.

$\text{H}_2\text{Pc}$  was purified by single-crystal formed sublimation 3 times (Figure 1). The van der Pauw type Au electrodes were formed on the 1  $\mu\text{m}$ -thick  $\text{H}_2\text{Pc}$  film (Figure 2). AC Hall measurement system (Toyo Technica, Resitest 8300) was used. AC magnetic field (0.1 Hz, 0.3 T at max.) was applied perpendicular to the film surface and Hall voltage of about  $10^{-6}$  V was precisely detected by the lock-in technique.

Carrier type was determined to p-type. Values of carrier concentration and hole mobility were determined to  $3.5 \times 10^{14} / \text{cm}^3$  and  $0.03 \text{ cm}^2/\text{Vs}$ , respectively. Very small value of carrier concentration of  $10^{14} / \text{cm}^3$  suggests that the purity of  $\text{H}_2\text{Pc}$  film is seven nines (7N) at least.

Purification and doping technique are crucially important to realize 15% efficient organic solar cells. The present AC Hall measurement is revealed to be a powerful tool to evaluate the purity and doping concentration in organic semiconductor films.

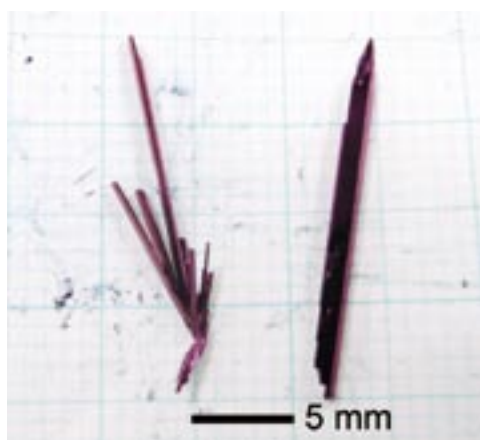


Figure 1. Photograph of single crystals of  $\text{H}_2\text{Pc}$ .

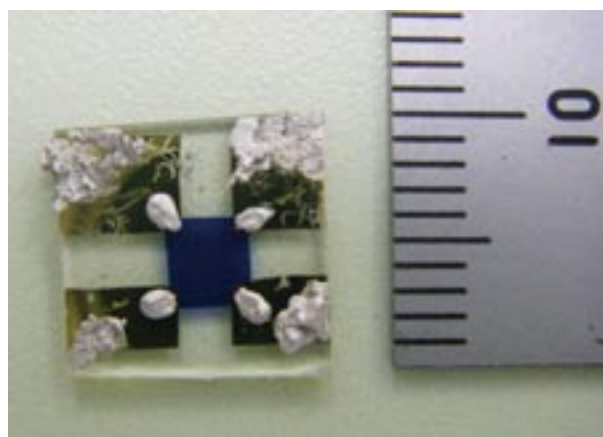
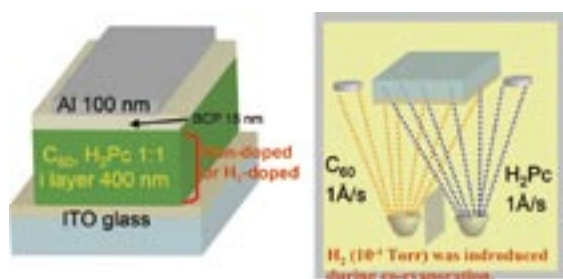


Figure 2. Photograph of  $\text{H}_2\text{Pc}$  cell for AC Hall effect measurements. Blue square part is  $\text{H}_2\text{Pc}$  film (1  $\mu\text{m}$ ).

## 2. n-Type C<sub>60</sub> Formation by H<sub>2</sub>-Doping

Hydrogen (H<sub>2</sub>) doping effect<sup>3)</sup> for C<sub>60</sub> was investigated. Highly purified 7N-C<sub>60</sub> (seven nines; 99.99999%) sample was used. Doping was performed by introducing H<sub>2</sub> gas ( $1 \times 10^{-4}$  Torr) into the evaporation chamber during the co-evaporation of C<sub>60</sub> and H<sub>2</sub>Pc (Figure 3). For ITO/H<sub>2</sub>Pc:C<sub>60</sub> codeposited layer/Al cell (Figure 3), open-circuit photovoltage ( $V_{oc}$ ) and short-circuit photocurrent ( $J_{sc}$ ) increased from 0.3 to 0.5 V and from 2 to 5 mA/cm<sup>2</sup>, respectively, by H<sub>2</sub>-doping (Figure 4). Internal quantum efficiency of  $J_{sc}$  increased 4 times from 5% to 20% in the absorption region of C<sub>60</sub> (400–500 nm). Similar result was observed for ITO/C<sub>60</sub> single layer/Al cell.

Above results can be reasonably explained by the increase of the built-in potential, which is caused by the negative shift of Fermi level ( $E_F$ ) of C<sub>60</sub> by H<sub>2</sub>-doping (Figure 5). We think that the n-type C<sub>60</sub> was formed by the intentional H<sub>2</sub>-doping. This is a clear demonstration of pn-control by the doping technique for organic semiconductors. Quantitative evaluation of donor concentration by H<sub>2</sub>-doping is now in progress by the AC Hall effect.



**Figure 3.** Sandwich-type cell of C<sub>60</sub>:H<sub>2</sub>Pc codeposited layer and H<sub>2</sub>-doping during co-evaporation.

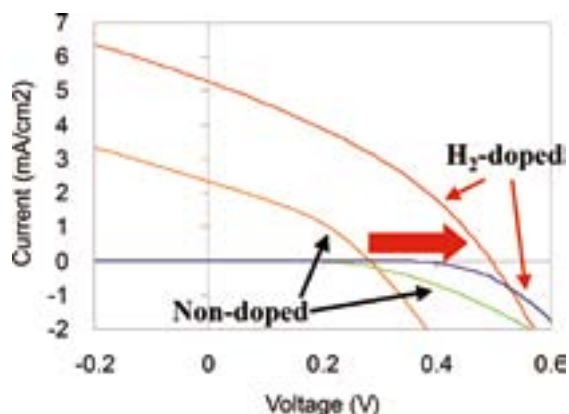


**Figure 4.** Current-voltage characteristics for undoped and H<sub>2</sub>-doped cells.

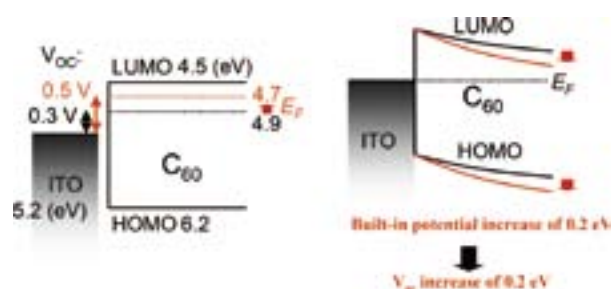


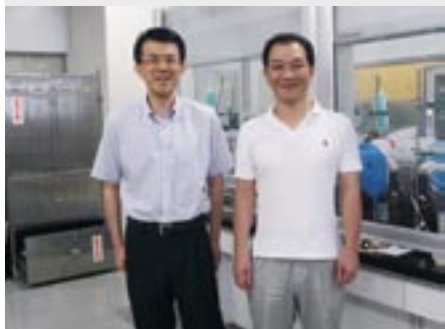
**Figure 5.** (a) Negative shift of Fermi level ( $E_F$ ) of C<sub>60</sub> by H<sub>2</sub>-doping. (b) Increase of built-in potential caused by  $V_{oc}$  increase.

### References

- 1) M. Hiramoto, *Proceedings of SPIE Vol. 7052, Organic photovoltaics IX*, pp 70520H-1-6, San Diego, CA, 12-14 Aug. (2008).
- 2) K. Sakai and M. Hiramoto, *Mol. Cryst. Liq. Cryst.* **491**, 284–289 (2008).
- 3) M. Hiramoto *et al.*, *Chem. Lett.* 119 (1990).

# Development of Organic Semiconductors for Molecular Thin-Film Devices

Research Center for Molecular Scale Nanoscience  
Division of Molecular Nanoscience



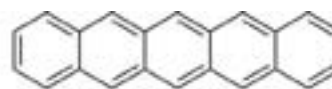
SUZUKI, Toshiyasu  
SAKAMOTO, Youichi  
WATANABE, Yoko

Associate Professor  
Assistant Professor  
Secretary

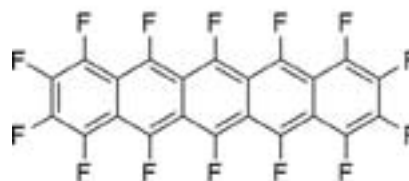
Organic light-emitting diodes (OLEDs) and organic field-effect transistors (OFETs) based on  $\pi$ -conjugated oligomers have been extensively studied as molecular thin-film devices. Organic semiconductors with low injection barriers and high mobilities are required for highly efficient OLEDs and OFETs. Radical cations or anions of an organic semiconductor have to be generated easily at the interface with an electrode (or a dielectric), and holes or electrons must move fast in the semiconducting layer. Compared with organic p-type semiconductors, organic n-type semiconductors for practical use are few and rather difficult to develop. Recently, we found that perfluorinated aromatic compounds are efficient n-type semiconductors for OLEDs and OFETs.

## 1. Effect of Fluorination on the Molecular Packing of Perfluoropentacene and Pentacene Ultrathin Films on Ag (111)<sup>1)</sup>

The growth of perfluoropentacene (PFP) and pentacene (PEN) ultrathin films on Ag(111) has been investigated using low-temperature scanning tunneling microscopy. To understand the influence that perfluorination of the parent molecule has on its resultant packing structure, the results are compared against each other in the framework of morphological differences. Perfluorination leads to a different packing structure in the first monolayer. We observed only one closely packed arrangement with periodic dislocation lines for PFP molecules, while for PEN molecules, there are two coexisting arrangements in the first monolayer. Monolayers of each molecule are commensurate with the underlying substrate with long axes of both molecules aligned in the [110] direction along the silver surface. The disparity in arrangements is attributed to the difference in peripheral atoms of the two molecules. Additional photoemission spectroscopy studies reveal that PFP physisorbs on Ag (111).



Pentacene (PEN)



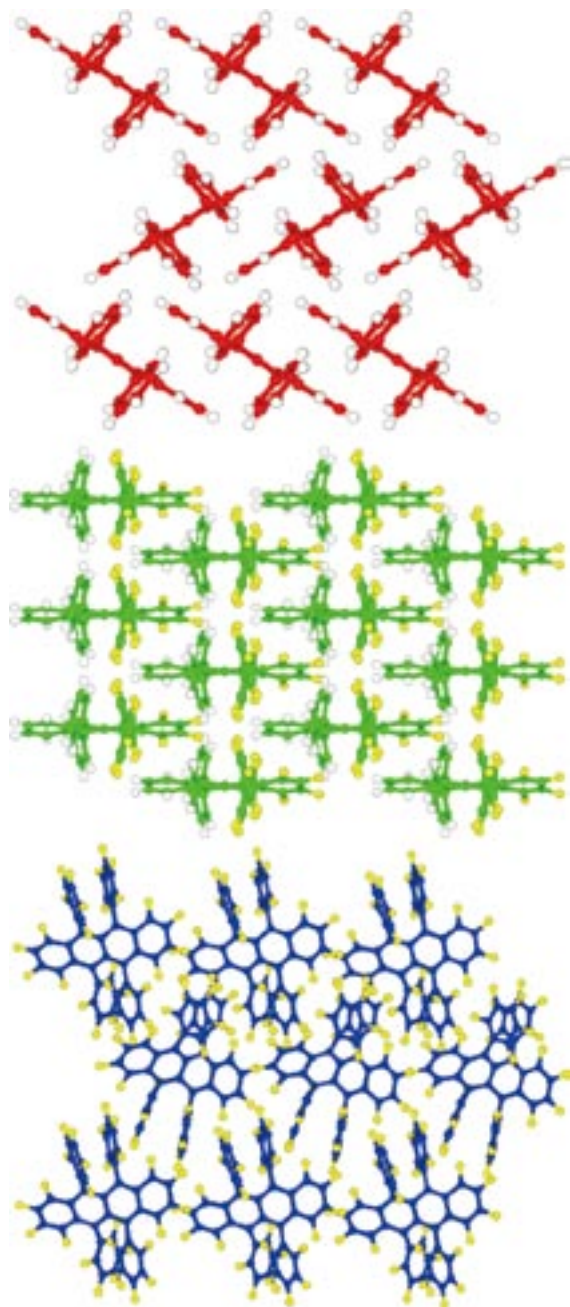
Perfluoropentacene (PFP)

Figure 1. Molecular structures of pentacene (PEN) and perfluoropentacene (PFP).

## 2. Synthesis, Structure, and Property of Fluorinated Rubrenes

Rubrene is the tetraphenyl-substituted tetracene and has a nonplanar structure unlike pentacene. The single-crystal field-effect transistors (FETs) with rubrene have shown the highest hole mobilities up to  $40 \text{ cm}^2\text{V}^{-1}\text{s}^{-1}$ . We synthesized partially and fully fluorinated rubrenes for single-crystal FETs with high electron mobilities. Tetradecafluororubrene (**F14-RB**) and perfluororubrene (**PF-RB**) are red crystalline solids similar to rubrene. The electrochemical measurements showed that the first reduction potentials shifted positively in the order of rubrene, **F14-RB**, and **PF-RB** ( $-2.06$ ,  $-1.48$ , and  $-0.92 \text{ V vs Fc/Fc}^+$ , respectively). The single-crystal X-ray analyses indicated that **F14-RB** adopted the 2-D  $\pi$ -stacking interactions with face-to-face distances as short as  $3.54 \text{ \AA}$ . In the case of **PF-RB**, no face-to-face interactions were found probably because the fluorine atoms resulted in larger molecular distances compared to the hydrogen atoms. The thin-film tran-

sistors (TFTs) with **F14-RB** and **PF-RB** have been fabricated, and they showed the n-type behaviors with the mobilities of  $10^{-6}$  to  $10^{-5}$   $\text{cm}^2\text{V}^{-1}\text{s}^{-1}$ . These values are similar to that of the rubrene TFT. The fabrications of the single-crystal transistors are underway.



**Figure 2.** Crystal structures of rubrene (top), **F14-RB** (middle), and **PF-RB** (bottom).

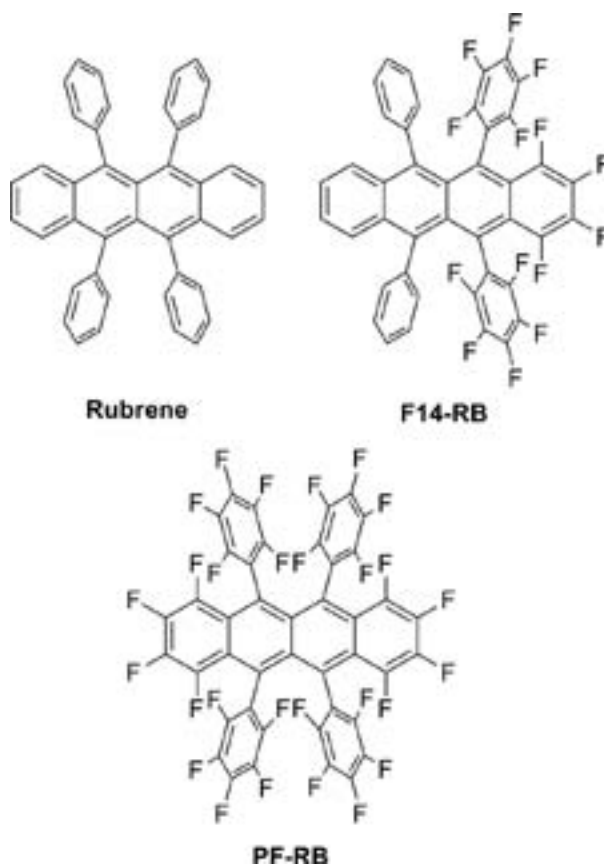


**Figure 3.** Molecular Structures of rubrene (top), **F14-RB** (middle), and **PF-RB** (bottom).

#### Reference

- 1) S. L. Wong, H. Huang, Y. L. Huang, Y. Z. Wang, X. Y. Gao, T. Suzuki, W. Chen and A. T. S. Wee, *J. Phys. Chem. C* **114**, 9356–9361 (2010).

# Building Photosynthesis by Artificial Molecules

Research Center for Molecular Scale Nanoscience  
Division of Molecular Nanoscience



NAGATA, Toshi  
KAWAO, Masahiro  
KON, Hiroki  
MIURA, Takahiro  
YUSA, Masaaki  
WANATABE, Yoko

Associate Professor  
IMS Fellow  
Post-Doctoral Fellow  
Graduate Student  
Graduate Student  
Secretary

The purpose of this project is to build nanomolecular machinery for photosynthesis by use of artificial molecules. The world's most successful molecular machinery for photosynthesis is that of green plants—the two photosystems and related protein complexes. These are composed almost exclusively from organic molecules, plus a small amount of metal elements playing important roles. Inspired by these natural systems, we are trying to build up multimolecular systems that are capable of light-to-chemical energy conversion. At present, our interest is mainly focused on constructing necessary molecular parts.

## 1. Synthesis of Single-Molecular Quinone Pools with Internal Redox Gradients and $^{19}\text{F}$ -NMR Handles

Mimicking photosynthesis by artificial molecules is an interesting research subject from both academic and industrial viewpoints. Although many aspects of natural photosynthesis have been successfully modeled by use of artificial molecules, there are still many important features that are yet unexplored by model chemists. One of such disregarded features is the quinone pool, which consists of a collection of quinones embedded in some biomembranes.

Previously we reported our research on building “single-molecular” quinone pools by use of synthetic dendrimer molecules.<sup>1,2)</sup> In these molecules, the quinones were converted to quinols by irradiation of the attached porphyrin with visible light in the presence of reducing agents (thiols). However, all quinones in these molecules were the same, so that there was no chance to realize vectorial electron transport which is essential for photochemical energy conversion.

In this work, we prepared new quinone pool molecules that contained two different quinones with different redox potentials. By changing the locations of the quinones, we can control the vectorial electron transport within the pool. We also introduced fluorine atoms to the quinones, which enable

selective observation of the changes in the quinone moieties by  $^{19}\text{F}$  NMR spectroscopy.

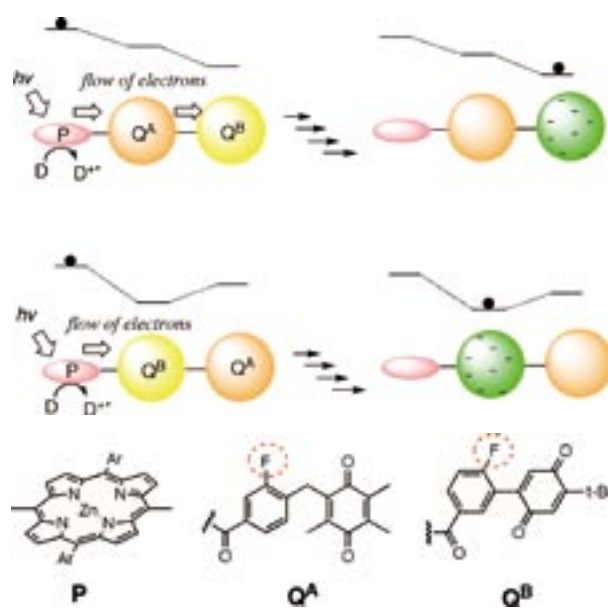


**Figure 1.** Pictorial representation of the quinone pool molecules in this work. P: Pigment (porphyrin),  $Q^A$  and  $Q^B$ : Quinones, D: Electron donor.

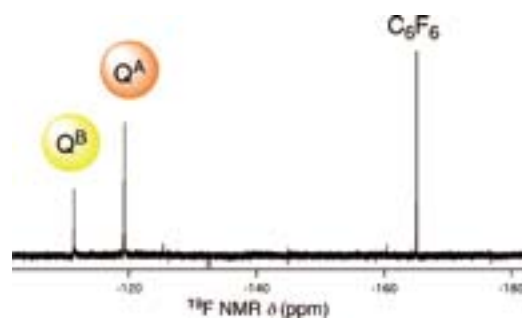


**Figure 2.** The  $^{19}\text{F}$  NMR of the synthesized quinone-pool molecule.



## 2. Synthesis of Zinc Porphyrin/Co(II) Polypyridine Dyad Molecules by Use of Terpyridine-Bipyridine Binary Ligands

Combination of photoinduced electron transfer and redox chemistry of transition metal complexes is an attractive way to achieve useful photochemical energy and materials conversion. A number of successful systems have been reported in the literature, however most of them share one potentially disturbing issue: Use of precious metals such as Ru, Rh and Re. In addition to their high cost, they may suffer from availability problems due to the low abundance of these elements. Therefore, it is desirable to substitute them with more common elements.

In the present study, we chose Zn porphyrins as photosensitizers, and a Co(II) polypyridine complex as a redox-active metal center. The redox chemistry of Co(II) is particularly interesting, because it can be converted to a super-nucleophilic Co(I) species by one-electron reduction, which can be easily achieved by photoinduced electron transfer.

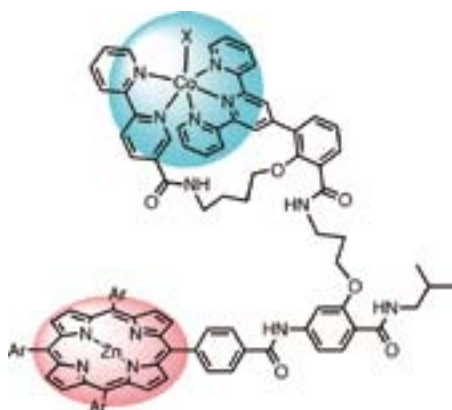


Figure 3. The Zn porphyrin/Co(II) complex dyad molecules.

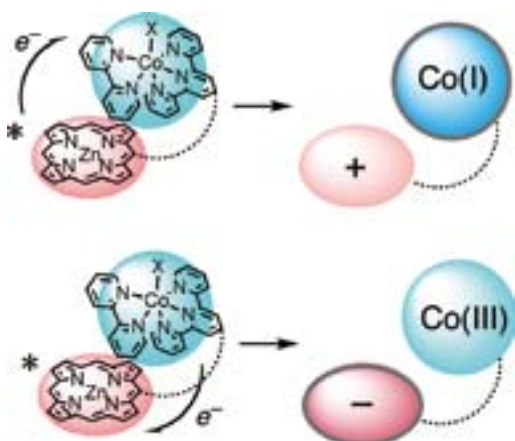


Figure 4. Two different routes for photoinduced electron transfer between the porphyrin and Co(II) complex

We synthesized a series of Zn porphyrin/Co(II) complex dyad molecules with two objectives. One is to utilize our terpyridine-bipyridine binary ligand which enabled predictable formation of Co(II) mononuclear complexes without complication by ligand exchange.<sup>3)</sup> The other is to examine the photochemical interaction between the Zn porphyrin and the Co(II) complex in the intramolecular manner, particularly with porphyrins having various redox potentials.

## 3. Synthesis of Diporphyrin Molecules with Tweezer-Like Bridges

Molecules capable of dynamic conformational change are gaining interest as components of “molecular machines.” Such conformational changes should be also useful in chemical energy conversions, as known in the molecular mechanism of cytochrome bc1 enzyme. Based on this consideration, we have started research on tweezer-like molecules whose photochemistry and redox chemistry can be modulated by conformational changes.

In this study, we synthesized a diporphyrin molecule with a tweezer-like bridge, where one leg of the tweezer has a zinc porphyrin and a positive charge, and the other leg has a free-base porphyrin and a negative charge. The conformation of the molecule was estimated by the intramolecular energy transfer from the zinc porphyrin to the free-base porphyrin. The conformational change in the solution phase was recorded by systematic change of the polarity and ionic strength of the surrounding media.



Figure 5. The dirporphyrin tweezer and the conformational change.

### References

- 1) T. Nagata and Y. Kikuzawa, *Biochim. Biophys. Acta* **1767**, 648–652 (2007).
- 2) T. Nagata, Y. Kikuzawa, T. Nagasawa and S. I. Allakhverdiev, *Trans. Mater. Res. Soc. Jpn.* **34**, 505–508 (2009).
- 3) H. Kon and T. Nagata, *Inorg. Chem.* **48**, 8593–8602 (2009).

# Chemistry of Bowl-Shaped Aromatic Compounds and Metal Nanocluster Catalysts

Research Center for Molecular Scale Nanoscience  
Division of Molecular Nanoscience



SAKURAI, Hidehiro	Associate Professor
HIGASHIBAYASHI, Shuhei	Assistant Professor
TSURUOKA, Ryoji	IMS Fellow
SAL PRIMA, Yudha S.	Visiting Scientist; JSPS Invited Fellow
SCHMIDT, Bernd	Visiting Scientist; JSPS Invited Fellow
MURUGADOSS, Arumugam	Visiting Scientist; JSPS Post-Doctoral Fellow
TAN, Qi-Tao	Visiting Scientist; JSPS Post-Doctoral Fellow
VARIPARAMBIL, Sajisha Sanjayan	Post-Doctoral Fellow
JEBAMALAI, W. J. B.	Post-Doctoral Fellow
BAIG, Nasir R.	Post-Doctoral Fellow
KITAHARA, Hiroaki	Post-Doctoral Fellow/Graduate Student
TOPOLINSKI, Berit	Visiting Scientist
CHEN, Hsiao Wei	Visiting Scientist
LORPITTHAYA, Rujee	Visiting Scientist
PURUSHOTHAM, Uppula	Visiting Scientist
ANH, Dang Thi Tuyet	Visiting Scientist
KARUEHANON, Weeranuch	Visiting Scientist
KATRUN, Praewpan	Visiting Scientist
DEIVASIGAMANI, Umadevi	Visiting Scientist
REZA, A. F. G. Masud	Graduate Student
ONOGI, Satoru	Graduate Student
DHITAL, Raghu Nath	Graduate Student
KATAOKA, Keita	Graduate Student
PREEDASURIYACHAI, Patcharee	Graduate Student*
NAKANO, Sachiko	Technical Fellow
KAI, Noriko	Technical Fellow
ISHIDA, Yuka	Technical Fellow
KIM, Yukimi	Technical Fellow
SASAKI, Tokiyo	Secretary
YURIKUSA, Tomoko	Secretary
TANIWAKE, Mayuko	Secretary

Bowl-shaped  $\pi$ -conjugated compounds including partial structures of the fullerenes, which are called “buckybowls,” are of importance not only as model compounds of fullerenes but also as their own chemical and physical properties. Heteroatom-containing buckybowls (heterobuckybowls) have also been expected to exhibit unique physical characters. For example, in solution they show the characteristic dynamic behavior such as bowl-to-bowl inversion. On the other hand, they sometimes favor stacking structure in a concave-convex fashion in the solid state, giving excellent electron conductivity. Furthermore, some buckybowls are conceivable to possess the bowl-chirality if the racemization process, as equal as bowl-to-bowl inversion, is slow enough to be isolated. However, very few buckybowls/heterobuckybowls has been achieved for preparation mainly due to their strained structure, and no report on the preparation of chiralbowls has appeared. In the present project, we develop the rational route to the various kinds of buckybowls/heterobuckybowls with perfect chirality control using the organic synthesis approach.

We also investigate to develop novel catalytic properties of metal nanoclusters. We focus on the following projects: Preparation of size-selective gold nanoclusters supported by hydrophilic polymers and its application to aerobic oxidation catalysts: Synthetic application using metal nanocluster catalyst: Development of designer metal nanocluster catalyst using the highly-functionalized protective polymers.

## 1. Optical Resolution of Chiral Buckybowls by Chiral HPLC<sup>1)</sup>

Buckybowls have been a focus of recent attention because of their interesting physical properties derived from the bowl-shaped  $\pi$ -conjugated aromatic structure. One of the interesting

features of the structure is the chirality of these spherical aromatic compounds unlike planer ones, named *Bowl chirality*. The bowl chirality is expected to provide fascinating characters for their applicability not only for asymmetric molecular recognition and chiral ligands for transition metals, but also for precursors of chiral fullerenes and carbon nanotubes in chemical synthesis. Enantiopure or -enriched chiral buckybowls could be obtained by either asymmetric synthesis or optical resolution of racemate. As an example of the former, we have recently achieved the first enantioselective synthesis of chiral trimethylsumanene (**1**) (Figure 1) by converting chirality based on  $sp^3$  carbon to bowl chirality. In contrast, the latter approach has not been reported, although those of related chiral fullerenes and carbon nanotubes have been reported. We focus on optical resolution of chiral buckybowls, trimethyltris(trimethylsilyl)sumanene (**2**) and trimethylsumanenetrione (**3**) (Figure 1), by chiral HPLC, and determination of bowl inversion energy barrier of **3** by CD spectra.

Optical resolution of racemic trimethyltris(trimethylsilyl)sumanene (**2**) was initially investigated for the following reasons. The ee of enantioselectively prepared substituted sumanenes would be easily determined by the chiral HPLC analysis of the tris(trimethylsilyl)-derivatives as well. Chiral column DAICEL CHIRALPAK<sup>®</sup> IA, which is composed of

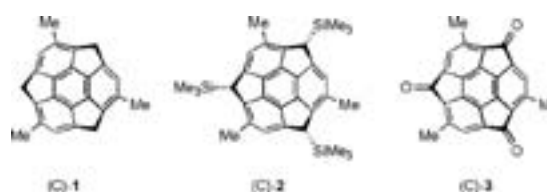
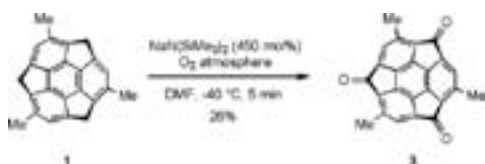


**Figure 1.** Structures of (C)-8,13,18-trimethylsumanene (**1**), (C)-(8R,13R,18R)-10,15,20-trimethyl-8,13,18-tris(trimethylsilyl)sumanene (**2**), and (C)-10,15,20-trimethylsumanene-8,13,18-trione (**3**).

amylose tris(3,5-dimethylphenylcarbamate), realized the desired optical resolution.

Next, we investigated the optical resolution of racemic **3**. The racemization energy barrier of **3** was estimated to be ca. 23.5 kcal/mol, which corresponds to ca. 44 h half-life at 10 °C. This could be sufficiently high to obtain enantioenriched **3** in HPLC time-scale. Racemic **3** was prepared by aerobic oxidation of racemic **1** (Scheme 1). Reaction of **1** with sodium hexamethyldisilazide and molecular oxygen in DMF at low temperature for 5 min gave the desired product in 26% yield. As expected, optical resolution of **3** was attained at 9 °C and afforded each enantioenriched sample of **3**. Absolute configuration of each enantiomer was assigned as (A)-**3** ( $t^R = 17$  min) and (C)-**3** ( $t^R = 18$  min) by the fact that enantioenriched sample prepared from (C)-**1** possessed  $t^R = 18$  min.



Scheme 1. Synthesis of trimethylsumanenetrione (**3**).

With enantioenriched **3** in hand by chiral HPLC separation, the bowl inversion energy barrier of **3** can be determined by CD spectra measurement. Bowl inversion is a characteristic feature of buckybowls and has been extensively studied by experimental and theoretical methods. A limitation of commonly used NMR methods for experimental determination of the energies is that those of buckybowls without diastereotopic protons cannot be determined by the technique. In contrast, the energies of enantiopure or -enriched chiral buckybowls even without diastereotopic protons such as **3** can be determined by CD spectra measurement because they are racemized through bowl inversion. By time-dependent decay of the intensity of CD spectra of **3** at 255 nm at 30 °C (Figure 2), the energy barrier was determined to be 23.4 and 23.3 kcal/mol in CH<sub>3</sub>CN and CH<sub>2</sub>Cl<sub>2</sub>, respectively. These experimental values showed good agreement with predicted values.

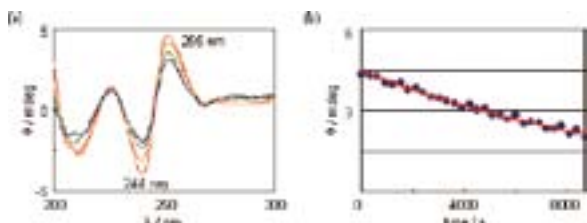


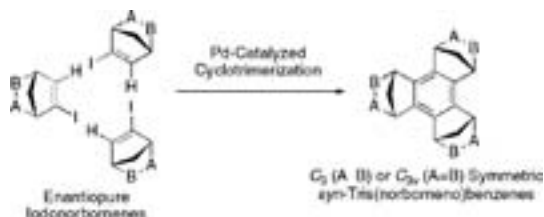
Figure 2. (a) Time-dependent decay of intensity of CD spectra of (A)-**3** in CH<sub>3</sub>CN at 30 °C (red: 0 h, orange: 1 h, green: 2 h, blue: 3 h). (b) Decay of ellipse  $\theta$  and their fitting curve at 255 nm in CH<sub>3</sub>CN at 30 °C.

#### Award

HIGASHIBAYASHI, Shuhei; The 24<sup>th</sup> Young Scholar Lectures in the 90<sup>th</sup> Annual Meeting of CSJ.

## 2. Stereoselective Cyclotrimerization of Enantiopure Iodonorbornenes Catalyzed by Pd Nanoclusters for C<sub>3</sub> Symmetric *syn*-Tris(norborneno)benzenes<sup>2)</sup>

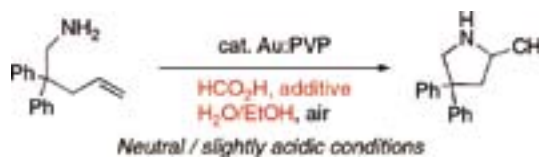
C<sub>3</sub> or C<sub>3v</sub> symmetric enantiopure *syn*-tris(norborneno)benzenes with various functional groups were synthesized through Pd-catalyzed cyclotrimerization of enantiopure iodonorbornenes. The generality of Pd-catalyzed cyclotrimerization for *syn*-tris(norborneno)benzenes were well-demonstrated.



Scheme 2. Pd-catalyzed cyclotrimerization of iodonorbornenes.

## 3. Gold Nanocluster as a Catalyst for Intramolecular Addition of Primary Amines to Unactivated Alkenes under Aerobic Conditions<sup>3)</sup>

Gold nanoclusters stabilized by hydrophilic polymer, poly(*N*-vinyl-2-pyrrolidone) (Au:PVP), catalyzed the intramolecular addition of primary amines to unactivated alkenes in good yield in the presence of formic acid derivatives under aerobic conditions. Since Au:PVP also promotes the cycloaddition of toluenesulfonamides under basic conditions, Au:PVP catalyst is expected to be a versatile and easy-to-handle catalyst for hydroamination reactions.



Scheme 3. Au:PVP-catalyzed Hydroamination.

#### References

- 1) R. Tsuruoka, S. Higashibayashi, T. Ishikawa, S. Toyota and H. Sakurai, *Chem. Lett.* **39**, 646–647 (2010).
- 2) S. Higashibayashi, A. F. G. Masud Reza and H. Sakurai, *J. Org. Chem.* **75**, 4626–4628 (2010).
- 3) H. Kitahara and H. Sakurai, *Chem. Lett.* **39**, 46–48 (2010).

\* carrying out graduate research on Cooperative Education Program of IMS with Chulalongkorn University

# Multifunction Integrated Macromolecules for Molecular-Scale Electronics

Research Center for Molecular Scale Nanoscience  
Division of Molecular Nanoscience



TANAKA, Shoji

Assistant Professor

Single molecular science and technology are the new frontier for physical and synthetic organic chemistry. Especially quantum device engineering is a promising field. Recently the power consumption of information processing systems becomes critical issues, and the growing demand for ultra-low-power device has led to a greater interest in a single electron tunneling (SET) device. A SET device manipulates an electron by means of one-by-one electron transfer, resulting in ultimately low power consumption. However, for room temperature operation, the size of SET device must be as small as a few nm to overcome the thermal fluctuation problems. The process size of a few nm is out of the range of conventional micro-technology, and therefore new nano fabrication approaches for SET device have been explored worldwide.

In this project, to establish an innovative fabrication process for SET device systems, we have been developing step-wise synthetic protocols for integrating molecule-based quantum device elements (quantum dots, wells, and tunnel junctions) within a single planar macromolecule. Our strategy is based on “modular architecture” using a library of basic functional building blocks, and so far we have developed various types and sizes of 1-dimensional (1D) building blocks (1-3). Now we shift to the next stage, that is, the development of multi-terminal building blocks for the step-wise fabrication of planar 2-dimensional (2D) macromolecular systems.

## 1. Development of Multi-Terminal Molecular Building Blocks for Precisely Defined Functional 2D-Macromolecules

To synthesize a precisely defined 2D-macromolecule we first prepared three types of multi-terminal modules (4-20). Figure 1 shows the molecular structures. The module Type-1 is a conductive junction block, in which the  $\pi$ -system of the main chain and that of the side chain are fully conjugated. The type-2 is a multi-terminal tunnel/capacitive junction block: The main chain and the side chain are electronically coupled by

tunnel or capacitive junction. The type-3 is an insulating spacer block: The side chain is used to prevent electrical short circuits between the conductive parts and to maintain a desired structure of the 2D system. Now we are challenging to fabricate planar 2D macromolecules operating as an individual SET device from these trial modules.

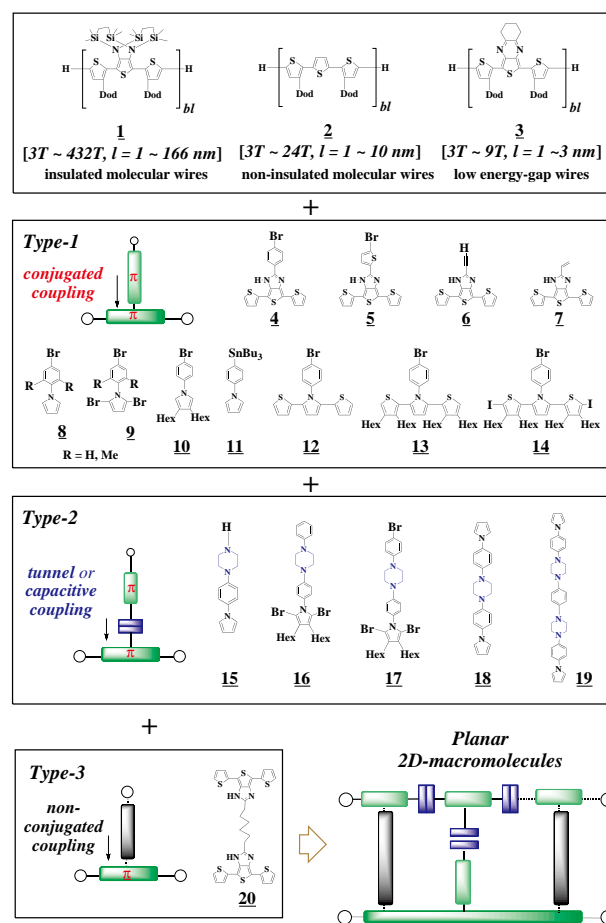


Figure 1. Structures of wire and multi-terminal modules.

# Development of Novel Heterocyclic Compounds and Their Molecular Assemblies for Advanced Materials

## Safety Office



TOMURA, Masaaki

Assistant Professor

Heterocycles containing sulfur and/or nitrogen atoms are useful as components of functional organic materials since heteroatoms in their rings are helpful to stabilize ions or ion-radical species. In addition, intermolecular interactions caused by heteroatom contacts can be expected to form unique molecular assemblies. In this project, novel functional organic materials based on various heterocycles were synthesized and their physical and structural properties were investigated.

## 1. A Two-Dimensional Ladder-Type Network in the 2:1 Co-Crystal of 1,2,5-Thiadiazole-3,4-dicarboxylic Acid and 4,4'-Bipyridine<sup>1)</sup>

The crystal structure of the 2:1 co-crystal of 1,2,5-thiadiazole-3,4-dicarboxylic acid and 4,4'-bipyridine has been determined by X-ray diffraction. Two intramolecular O–H...N [2.730(7) Å] and O–H...O [2.433(6) Å] hydrogen bonds are observed in the thiadiazole molecule. In the crystal structure, the molecules form a unique two-dimensional ladder-type network linked by intermolecular O–H...N [2.704(4) Å] hydrogen bonds and S...O [3.100(5) Å] heteroatom interactions.

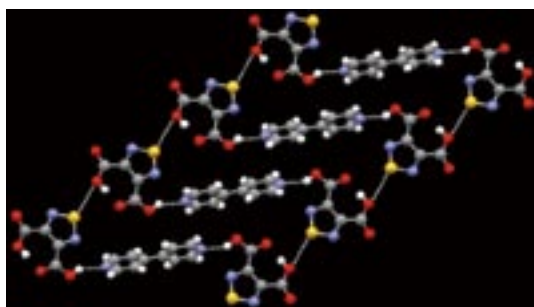
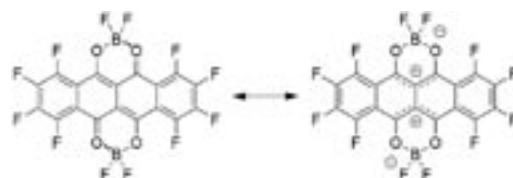


Figure 1. A unique two-dimensional ladder-type network.

## 2. A BF<sub>2</sub> Complex of a Dihydroxydione with a Perfluorotetracene Skeleton<sup>2)</sup>

A BF<sub>2</sub> complex containing an octafluorotetracene moiety was synthesized as a new type of electron acceptor. This compound exhibits a long-wavelength absorption based on the perfluorotetracene skeleton and high electron affinity due to its quadrupolar structure enhanced by fluorination. The BF<sub>2</sub> complex exhibited n-type semiconducting behavior.



## 3. Photovoltaic Properties of (*E*)-2-Cyano-3-[4-(diphenylamino)phenyl]acrylic Acid Substituted by *tert*-Butyl Groups<sup>3)</sup>

The title dye and its related compounds were synthesized. The *tert*-butyl substituents decreased molecular stacking in the crystals, thus affecting the photovoltaic properties of the dyes. A solar cell using the dye exhibited higher performance than that for the analog without *tert*-butyl group substitution.

### References

- 1) M. Tomura and Y. Yamashita, *Struct. Chem.* **21**, 107–111 (2010).
- 2) K. Ono, J. Hashizume, H. Yamaguchi, M. Tomura, J. Nishida and Y. Yamashita, *Org. Lett.* **11**, 4326–4329 (2009).
- 3) K. Ono, T. Yamaguchi and M. Tomura, *Chem. Lett.* **39**, 864–866 (2010).

## Visiting Professors



Visiting Professor  
**NAKAZAWA, Yasuhiro** (from *Osaka University*)

### Low-Temperature Calorimetric Studies of Organic Conductors and Organic Magnets

The calorimetry system equipped with the dilution refrigerator of instrument center (Kelvinox300 Oxford Instruments) is under construction at IMS. We have prepared a Ag-based relaxation calorimetry cell which are consisting of tiny film heater and a chip type ruthenium oxide sensor. The magnetoresistance of the sensor has been measured and we have confirmed that the sensor is available up to 16 T. The heat capacity measurement of a 45  $\mu\text{g}$  single crystal of  $\kappa\text{-BETS}_2\text{FeCl}_4$  has been succeeded in a temperature range between 100 mK and 2 K. This compound is known as an organic magnetic superconductor in which superconductivity and magnetic order coexists below about 120 mK. A large thermal anomaly due to the long range ordering of  $\text{Fe}^{3+}$  has been observed at 500 mK. The application of weak magnetic fields reduces the peak temperature which is consistent with the behavior of typical antiferromagnetic system. The experiment to clarify relationship between magnetism and superconductivity is in progress now. The microchip calorimetry devices obtained by the micro-fabrication technique will be installed in the dilution refrigerator in order to study  $\mu\text{g}$  class single crystal samples with high resolution.



Visiting Professor  
**SEKIYA, Hiroshi** (from *Kyushu University*)

### Spectroscopic Study on Intermolecular Interactions and Dynamics in Hydrogen-Bonded Clusters and Coordination and Solvation Structures of Transition Metal Ions

We investigate the structures, intermolecular interactions, and dynamics associated with hydrogen-bonded networks in crystals as well as in the gas phase. These studies provide insights into dynamics of hydration water on the surface of proteins. Rearrangement of water networks has been observed for model hydrated amino groups in the gas phase. In molecular crystals, cooperative multiple-proton transfer along one-dimensional hydrogen-bond networks has been investigated. We also investigate the coordination and solvation structures of transition-metal ions.  $\text{Co}^+(\text{NH}_3)_n$ ,  $\text{Ag}^+(\text{NH}_3)_n$  and  $\text{Ni}^+(\text{NH}_3)_n$  are studied by infrared spectroscopy and quantum chemical calculations.  $\text{Ag}^+$  and  $\text{Ni}^+$  adopt tetrahedral and square-planar coordination, and a distorted tetrahedral coordination, respectively. The results demonstrate a close relationship between the d-electron configurations of the metals and the geometric structures of the solvated complexes.



Visiting Professor  
**OHTA, Nobuhiro** (from *Hokkaido University*)

### Photoirradiation Effects on Magnetic Property of Organic Conductors and Ionic Conductors

Photoinduced change in the electrical conductivity of organic conductor or ionic conductor has been examined with the time-resolved measurements of the change in resistance following photoirradiation or with the impedance spectroscopy in the absence and presence of photoirradiation. In the photoirradiated organic crystals, conductivity switching and bistability of current over certain ranges of applied voltages have been observed. In organic superconductors, photoinduced change in the electrical conductivity has been also examined at temperatures in the vicinity of the metal–superconductor (M–S) phase transition temperature, and unconventional asymmetry of critical slowing down about the M–S transition temperature has been found. In ionic conductor such as silver iodide, photoirradiation effect on ionic conductivity has been observed, depending on the excitation wavelength. To understand the photoirradiation effect as well as the synergy effect of photoirradiation and applied electric field on electrical conductivity, photoirradiation effects not only on the electrical conductivity but also on the magnetic property will be examined.



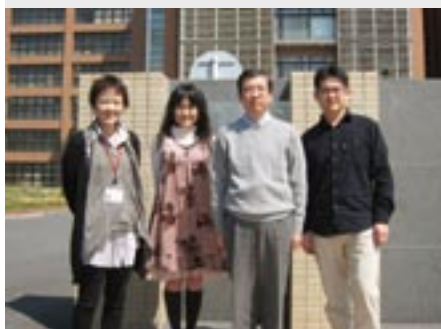
## RESEARCH ACTIVITIES

### Life and Coordination-Complex Molecular Science

Department of Life and Coordination-Complex Molecular Science is composed of four divisions of Biomolecular science, two divisions of Coordination molecular science and two adjunct divisions. Biomolecular science divisions cover the studies on the elucidation of functions and mechanisms for various types of sensor proteins, protein folding, molecular chaperone, and metal proteins. Coordination complex divisions aim to develop molecular catalysts for the transformation of organic molecules, activation small inorganic molecules, and reversible conversion between chemical and electrical energies. Interdisciplinary alliances in the Department aim to create new basic concepts for the molecular and energy conversion through the fundamental science conducted at each division.

# Bioinorganic Chemistry of Metal-Containing Sensor Proteins

Department of Life and Coordination-Complex Molecular Science  
Division of Biomolecular Functions



AONO, Shigetoshi  
YOSHIOKA, Shiro  
ISHIKAWA, Haruto  
SAWAI, Hitomi

TANIZAWA, Misako

Professor  
Assistant Professor  
IMS Research Assistant Professor\*  
JSPS Post-Doctoral Fellow (–March '10)  
Post-Doctoral Fellow (–April '10)  
IMS Research Assistant Professor (May '10–)  
Secretary

Hemeproteins are a typical metalloprotein, which show a variety of functions including oxygen storage/transport, electron transfer, redox catalysis with various substrates. Besides these traditional functions of hemeproteins, a new function of hemeprotein has been found recently, which is a sensor of diatomic gas molecules or redox change.<sup>1)</sup> In these heme-based sensor proteins, the heme acts as the active site for sensing the external signal such as gas molecules and redox change. Our research interests are focused on the elucidation of the structure-function relationships of these heme-based sensor proteins. We are also studying about an iron-sulfur (Fe-S) cluster-containing sensor protein responsible for the transcriptional regulation of nitrogenase gene.

## 1. Oxygen Sensor Proteins Responsible for Aerotaxis (Chemotaxis toward Molecular Oxygen) Control in Bacteria

Chemotaxis is a major biological signal transduction system, which consists of signal transducer proteins and several chemotaxis proteins including CheA, CheY, and CheW responsible for intermolecular signal transduction to control direction of flagellar rotation. Signal transducer proteins, sometimes called as MCPs (methyl-accepting chemotaxis proteins), bind a repellent or attractant in their sensor domain. Many chemical and physical stimuli act as a repellent or attractant, among which molecular oxygen is a typical gaseous signaling molecule. In this work, we have studied the structure and function relationships of MCPs, Aer2 and HemAT, that sense molecular oxygen for aerotaxis (chemotaxis toward molecular oxygen) control.

HemAT is well known as a MCP that senses molecular oxygen for aerotaxis control, which contains a *b*-type heme as the active site for sensing molecular oxygen. Though both of HemAT and Aer2 use a heme as the active site for sensing

molecular oxygen, the sensor domains of HemAT and Aer2 are different. HemAT and Aer2 adopt a globin domain and PAS domain as their sensor domains, respectively. Though the globin domain of HemAT shows a structural homology to myoglobin, it has a different heme environmental structure in the distal heme pocket from myoglobin. In the case of myoglobin, a distal His forms a hydrogen bond with the heme-bound oxygen to stabilize the heme-oxygen complex. However, there is no distal His in HemAT, in which a Thr is involved in the formation of a hydrogen bonding network upon oxygen binding to HemAT. We have studied conformational changes induced by oxygen binding by means of resonance Raman spectroscopy.

Aer2 is a new MCP responsible for aerotaxis of *Pseudomonas aeruginosa*, which adopts a PAS domain as a sensor domain. We have constructed an expression system of Aer2 in *E. coli* and purified the recombinant protein. The purified Aer2 shows the Soret,  $\alpha$  and  $\beta$  peaks at 419, 578, and 543 nm, respectively, as shown in Figure 1. When the purified Aer2 is

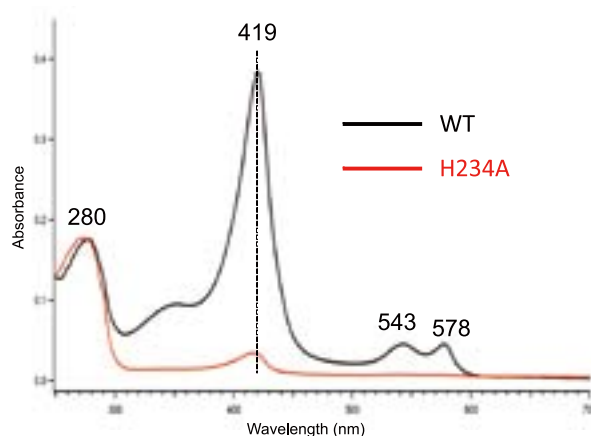


**Figure 1.** Electronic absorption spectra of wild-type and H234A mutant Aer2.



reacted with CO, CO-bound Aer2 is formed. The purified Aer2 shows a typical Resonance Raman spectrum of oxygen-bound heme proteins. These results indicate that Aer2 is purified as an oxygen-bound form.

Domain analysis by using SMART program (<http://smart.embl-heidelberg.de/>) reveals that Aer2 consists of a PAS domain in its N-terminal region. PAS domain is widely used as a sensor domain sensing various chemical and physical signals. PAS domains show a similar 3D structure, though their amino acid sequences do not necessarily show a high homology. Figure 2 shows X-ray crystal structures of the heme-containing PAS domain of FixL that is an oxygen sensor protein in FixL/FisJ two-component system. The PAS domain of Aer2 would

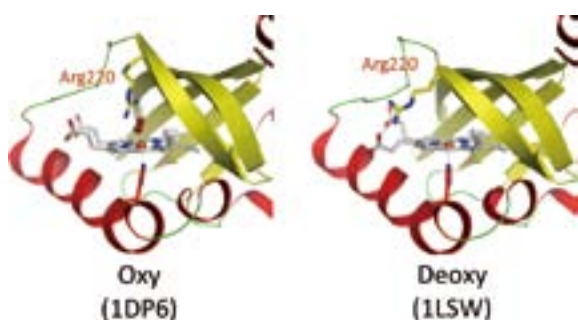


**Figure 2.** X-ray crystal structure of the PAS domain of FixL in oxy- and deoxy-forms. PDB accession numbers are shown in parenthesis.

be similar to that of FixL. Amino acid sequence alignments among heme-containing PAS domains including Aer2 show that a His residue is conserved at the position of 234 in Aer2, at which the proximal ligand of the heme is located in other heme-containing PAS domains. Site-directed mutagenesis reveals that His234 is indeed the proximal ligand of the heme in Aer2. Mutation of His234 to Ala results in loss of heme (Figure 1). Further characterization of Aer2 is now in progress.

## 2. The Role of the Fe-S Cluster in the Sensory Domain of Nitrogenase Transcriptional Activator VnfA from *Azotobacter vinelandii*<sup>2)</sup>

Transcriptional activator VnfA is required for the expres-

sion of the second nitrogenase system encoded in the *vnfH* and *vnfDGK* operons in *Azotobacter vinelandii*. VnfA belongs to a  $\sigma^N$ -dependent regulatory protein generally consisting of three major domains, and contains a GAF domain in its N-terminal region as a sensory domain. VnfA has a characteristic Cys-rich motif, Cys-X-Cys-XXXX-Cys, in its GAF domain. Although this motif is supposed to be a metal ions/cluster binding motif, metal ions/cluster in VnfA is not characterized yet. In the present study, we have purified full-length VnfA produced in *E. coli* as recombinant proteins (*Strep*-tag attached and tag-less proteins), enabling detailed characterization of VnfA for the first time. The EPR spectra of whole cells producing tag-less VnfA (VnfA) show distinctive signals assignable to a 3Fe-4S cluster in the oxidized form ( $[\text{Fe}_3\text{S}_4]^+$ ). Although aerobically purified VnfA shows no vestiges of any Fe-S clusters, enzymatic reconstitution under anaerobic conditions reproduced  $[\text{Fe}_3\text{S}_4]^+$  dominantly in the protein. Additional spectroscopic evidence of  $[\text{Fe}_3\text{S}_4]^+$  *in vitro* is provided by anaerobically purified *Strep*-tag attached VnfA. Thus, spectroscopic studies both *in vivo* and *in vitro* indicate the involvement of  $[\text{Fe}_3\text{S}_4]^+$  as a prosthetic group in VnfA. Molecular mass analyses reveal that VnfA is a tetramer both in the presence and absence of the Fe-S cluster. Quantitative data of iron and acid-labile sulfur in reconstituted VnfA are fitted with four 3Fe-4S clusters per a tetramer, suggesting that one subunit bears one cluster. *In vivo*  $\beta$ -gal assays reveal that the Fe-S cluster which is presumably anchored in the GAF domain by the N-terminal cysteine residues is essential for VnfA to exert its transcription activity on the target nitrogenase genes. Unlike the NifAL system of *A. vinelandii*,  $\text{O}_2$  shows no effect on the transcriptional activity of VnfA but reactive oxygen species is reactive to cause disassembly of the Fe-S cluster and turns active VnfA inactive.

### References

- 1) S. Aono, *Dalton Trans.* 3125–3248 (2008).
- 2) H. Nakajima, N. Takatani, K. Yoshimitsu, M. Itoh, S. Aono, Y. Takahashi and Y. Watanabe, *FEBS J.* **277**, 817–832 (2010).

\* Present Address: Department of Chemistry, Graduate School of Science, Osaka University, Toyonaka, Osaka 560-0043

# Elucidation of the Molecular Mechanisms of Protein Folding

Department of Life and Coordination-Complex Molecular Science  
Division of Biomolecular Functions



KUWAJIMA, Kunihiro	Professor
MAKABE, Koki	Assistant Professor
NAKAMURA, Takashi	IMS Research Assistant Professor
CHEN, Jin	OIB Research Assistant Professor
TAKENAKA, Toshio	Post-Doctoral Fellow
TAKAHASHI, Kazunobu	Graduate Student*
MIZUKI, Hiroko	Technical Fellow
TANAKA, Kei	Secretary

Kuwajima group is studying mechanisms of *in vitro* protein folding and mechanisms of molecular chaperone function. Our goals are to elucidate the physical principles by which a protein organizes its specific native structure from the amino acid sequence. In this year, we carried out comparative studies of folding pathways of highly homologous proteins, goat  $\alpha$ -lactalbumin and canine milk lysozyme.

## 1. Different Folding Pathways Taken by Highly Homologous Proteins, Goat $\alpha$ -Lactalbumin and Canine Milk Lysozyme<sup>1)</sup>

Is the folding pathway conserved in homologous proteins? To address this question, we compared the folding pathways of goat  $\alpha$ -lactalbumin and canine milk lysozyme using equilibrium and kinetic circular dichroism spectroscopy. Both  $\text{Ca}^{2+}$ -binding proteins have 41% sequence identity and essentially identical backbone structures. The  $\Phi$ -value analysis, based on the effect of  $\text{Ca}^{2+}$  on the folding kinetics, showed that the  $\text{Ca}^{2+}$ -binding site was well organized in the transition state in  $\alpha$ -lactalbumin, although it was not yet organized in lysozyme. Equilibrium unfolding and hydrogen-exchange 2D NMR analysis of the molten globule intermediate also showed that different regions were stabilized in the two proteins. In  $\alpha$ -lactalbumin, the  $\text{Ca}^{2+}$ -binding site and the C-helix were weakly organized, whereas the A- and B-helices, both distant from the  $\text{Ca}^{2+}$ -binding site, were well organized in lysozyme. The results thus provide an example of highly homologous proteins taking different folding pathways. To understand the molecular origin of this difference, we investigated the native three-dimensional structures of the proteins in terms of non-local

contact clusters, a parameter based on the residue–residue contact map and known to be well correlated with the folding rate of non-two-state proteins. There were remarkable differences between the proteins in the distribution of the non-local contact clusters, and these differences provided a reasonable explanation of the observed difference in the folding initiation sites. In conclusion, the protein folding pathway is determined not only by the backbone topology but also by the specific side-chain interactions of contacting residues.

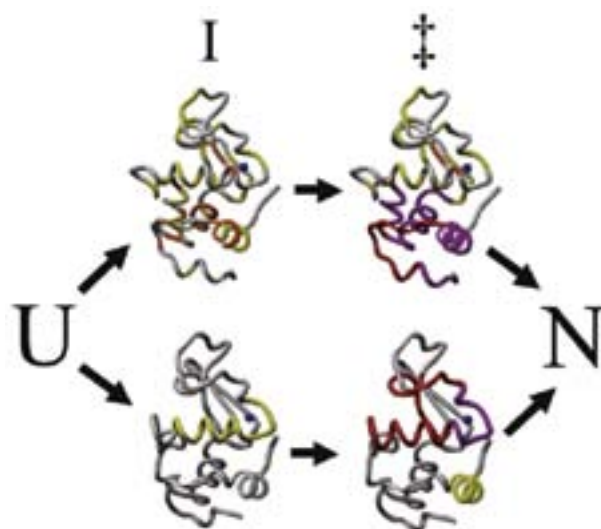


**Figure 1.** A folding model of  $\alpha$ -lactalbumin/lysozyme family proteins. Two parallel pathways are available for the backbone topology of this family, and the lower and upper pathways are taken by goat  $\alpha$ -lactalbumin and canine milk lysozyme, respectively, because of the distributions of the strong clusters in their native 3D structures.

## 2. Flexible Recognition of the tRNA G18 Methylation Target Site by TrmH Methyltransferase through First Binding and Induced Fit Processes<sup>2)</sup>

Transfer RNA (Gm18) methyltransferase (TrmH) catalyzes methyl transfer from S-adenosyl-L-methionine to a conserved G18 in tRNA. We investigated the recognition mechanism of *Thermus thermophilus* TrmH for its guanosine target. Thirteen yeast tRNA(Phe) mutant transcripts were prepared in which the modification site and/or other nucleotides in the D-loop were substituted by dG, inosine, or other nucleotides. We then conducted methyl transfer kinetic studies, gel shift assays, and inhibition experiments using these tRNA variants. Sites of methylation were confirmed with RNA sequencing or primer extension. Although the G18G19 sequence is not essential for methylation by TrmH, disruption of G18G19 severely reduces the efficiency of methyl transfer. There is strict recognition of guanosine by TrmH, in that methylation occurs at the adjacent G19 when the G18 is replaced by dG or adenosine. The fact that TrmH methylates guanosine in D-loops from 4 to 12 nucleotides in length suggests that selection of the position of guanosine within the D-loop is relatively flexible. Our studies also demonstrate that the oxygen 6 atom of the guanine base is a positive determinant for TrmH recognition. The recognition process of TrmH for substrate is inducible and product-inhibited, in that tRNAs containing Gm18 are excluded by TrmH. In contrast, substitution of G18 with dG18 results in the formation of a more stable TrmH-tRNA complex. To address the mechanism, we performed the stopped-flow pre-steady state kinetic analysis. The result clearly showed that the binding of TrmH to tRNA is composed of at least three steps, the first bi-molecular binding and the subsequent two uni-molecular induced-fit processes.

## 3. Adaptation of a Hyperthermophilic Group II Chaperonin to Relatively Moderate Temperatures<sup>3)</sup>

Group II chaperonins exist in archaea and the eukaryotic

cytosol, and mediate protein folding in an ATP-dependent manner. We have been studying the reaction mechanism of group II chaperonins using alpha chaperonin, the recombinant chaperonin alpha subunit homo-oligomer from a hyperthermophilic archaeon, *Thermococcus* sp. strain KS-1 (*T. KS-1*). Although the high stability and activity of *T. KS-1* alpha chaperonin provided advantages for our study, its high thermophilicity caused the difficulty in using various analytical methods. To resolve this problem, we tried to adapt *T. KS-1* alpha chaperonin to moderate temperatures by mutations. The comparison of amino acid sequences between 26 thermophilic and 17 mesophilic chaperonins showed that three amino acid replacements are likely responsible for the difference of their optimal temperatures. We introduced three single mutations and also their double combinations into *T. KS-1* alpha chaperonin. Among them, K323R single mutant exhibited the improvements of the folding activity and the ATP-dependent conformational change ability at lower temperatures, such as 50 °C and 40 °C. Since K323 may secure helix 12 in the closed conformation by interacting with D198, the replacement of Lys to Arg likely induced the higher mobility of the built-in lid, resulting in the higher activity at relatively low temperatures.

### References

- 1) T. Nakamura, K. Makabe, K. Tomoyori, K. Maki, A. Mukaiyama and K. Kuwajima, *J. Mol. Biol.* **396**, 1361–1378 (2010).
- 2) A. Ochi, K. Makabe, K. Kuwajima and H. Hori, *J. Biol. Chem.* **285**, 9018–9029 (2010).
- 3) T. Kanzaki, S. Ushioku, A. Nakagawa, T. Oka, K. Takahashi, T. Nakamura, K. Kuwajima, A. Yamagishi and M. Yohda, *Protein Eng., Des. Sel.* **23**, 393–402 (2010).

\* carrying out graduate research on Cooperative Education Program of IMS with the University of Tokyo

# Elucidation of Dynamical Structures of Biomolecules toward Understanding the Mechanisms Underlying Their Functions

Department of Life and Coordination-Complex Molecular Science  
Division of Biomolecular Functions



KATO, Koichi  
YAMAGUCHI, Takumi  
KAMIYA, Yukiko  
UEKUSA, Yoshinori  
SERVE, Olivier  
MONDAL, Gautam  
CHOO, Yeun-Mun  
SUGIHARA, Takahiro  
YAGI-UTSUMI, Maho  
NISHIO, Miho  
YOSHIKAWA, Sumi  
HIRANO, Takashi  
BUNKO, Yuji  
UNO, Tsuyoshi  
YAMAMOTO, Sayoko  
SUZUKI, Mariko  
ISONO, Yukiko  
TANAKA, Kei

Professor  
Assistant Professor  
IMS Research Assistant Professor  
JSPS Post-Doctoral Fellow  
Post-Doctoral Fellow  
Visiting Scientist  
Visiting Scientist  
Research Fellow  
Research Fellow  
Graduate Student\*  
Graduate Student\*  
Graduate Student\*  
Graduate Student\*  
Graduate Student\*  
Graduate Student\*  
Graduate Student\*  
Technical Fellow  
Technical Fellow  
Secretary

Our biomolecular studies are based on detailed analyses of structures and dynamics of various biological macromolecules and their complexes at atomic level, primarily using nuclear magnetic resonance (NMR) spectroscopy. In particular, we conducted studies aimed at elucidating dynamic structures of glycoconjugates and proteins for integrative understanding of the mechanisms underlying their biological functions. For this purpose, we use multidisciplinary approaches integrating the methodologies of molecular and cellular biology and nano-science along with molecular spectroscopy.

## 1. NMR Characterization of the Interaction between Amyloid $\beta$ -Peptide and Ganglioside Clusters<sup>1,2)</sup>

Gangliosides are targets for a variety of pathologically relevant proteins, including amyloid  $\beta$  ( $A\beta$ ), an important component implicated in Alzheimer's disease (AD). To provide a structural basis for this pathogenic interaction associated with AD, we conducted NMR analyses of the interactions of  $A\beta$  with gangliosides using lyso-GM1 micelles as a model system. Our NMR data revealed that the sugar-lipid interface is primarily perturbed upon binding of  $A\beta$  to the micelles, underscoring the importance of the inner part of the ganglioside cluster for accommodating  $A\beta$  in comparison with the outer carbohydrate branches that provide microbial toxin- and virus-binding sites. To provide a more detailed understanding of the interaction mode of  $A\beta$  and gangliosides, we observed NMR peaks originating from isotopically labeled  $A\beta$  bound to the micelles. The secondary chemical shifts of the polypeptide backbone indicated that  $A\beta$  forms discontinuous  $\alpha$ -helices upon binding to the gangliosidic micelles, leaving the remaining regions disordered. TROSY-based saturation transfer

analyses revealed that  $A\beta$  lies on hydrophobic/hydrophilic interface of the ganglioside cluster exhibiting an up-and-down topological mode in which the two  $\alpha$ -helices and the C-terminal dipeptide segment are in contact with the hydrophobic interior, whereas the remaining regions are exposed to the aqueous environment (Figure 1). These findings suggest that the ganglioside clusters provide a unique platform at their hydrophobic/hydrophilic interface for binding coupled with conformational transition of  $A\beta$  molecules, rendering their spatial rearrangements restricted to promote specific inter-molecular interactions.

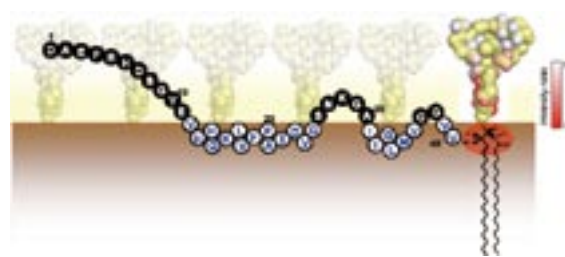


**Figure 1.** Schematic drawing of  $A\beta(1-40)$  lying on the hydrophobic/hydrophilic interface of ganglioside clusters. The amino acid residues exposed to the hydrophilic and hydrophobic milieus are represented by closed and open circles with single-letter codes. The sugar hydrogen atoms coloured in red and the ceramide hydrogen atoms located within the red ellipse area exhibit lower peak intensity ratios, indicating that they are in close spatial proximity of the C-terminus of  $A\beta(1-40)$ .

## 2. Structural Basis of the Protein-Fate Determination in Cells<sup>3-6)</sup>

In eukaryotic cells, folding of nascent proteins is assisted by complexes of molecular chaperones in the endoplasmic

reticulum (ER). Correctly folded proteins are transferred from the ER to the Golgi complex on the secretion pathway, while terminally misfolded proteins are transferred from the ER to the cytosol and subsequently degraded in the ubiquitin (Ub)- and proteasome-mediated proteolytic pathway. We conducted structural biology studies of the ER chaperones, the cargo receptors, and the ubiquitinating enzymes to elucidate the mechanisms underlying the protein-fate determination in cells.

Protein disulfide isomerase (PDI) is a major protein in the ER, operating as an essential folding catalyst and molecular chaperone for disulfide-containing proteins by catalyzing the formation, rearrangement, and breakage of their disulfide bridges. By combined use of NMR and small-angle X-ray scattering methods, we reveal the redox-dependent domain rearrangement of PDI coupled with exposure of its substrate-binding hydrophobic surface spanning the *b'* and *a'* domains (Figure 2A). On the basis of these data, we propose a mechanistic model of PDI action; the *a'* domain transfers its own disulfide bond into the unfolded protein accommodated on the hydrophobic surface, which consequently changes into a *closed* form releasing the oxidized substrate.

The intracellular lectin ERGIC-53 and the EF-hand  $\text{Ca}^{2+}$ -binding protein MCFD2, which have been identified as products of the causative genes of combined deficiency of coagulation factors V and VIII (F5F8D), form a complex operating as cargo receptor of these coagulation factors. We determined the 3D structure of ERGIC-53 complexed with MCFD2 by X-ray crystallographic analysis in conjunction with NMR and ultracentrifugation analyses (Figure 2B). The interaction is independent of sugarbinding of ERGIC-53 and involves most of the missense mutation sites of MCFD2 so far reported in F5F8D. Comparison with the previously reported uncomplexed structure of each protein indicates that MCFD2 but not ERGIC-53-CRD undergoes significant conformational alterations upon complex formation. These findings provide a structural basis for the cooperative interplay between ERGIC-53 and MCFD2 in capturing FV and FVIII.

A key question in ubiquitination is how E2-E3 complexes can deal with the various acceptor sites distributed on the substrate surface to perform multiple ubiquitination and/or poly-Ub elongation. We solved the crystal structure of an intermediate of the UbcH5b E2 enzyme conjugated with Ub which is assembled into an infinite spiral through the backside interaction (Figure 2C). This active complex may provide multiple E2 active sites, enabling efficient ubiquitination of substrates. Indeed, biochemical assays support a model in which the self-assembled UbcH5b~Ub can serve as a bridge for the gap between the lysine residue of the substrate and the catalytic cysteine of E2.

#### Award

YAGI-UTSUMI, Maho; Poster Presentation Award, The 74<sup>th</sup> Annual meeting in The Japanese Biochemical Society, Chubu Branch (2010).

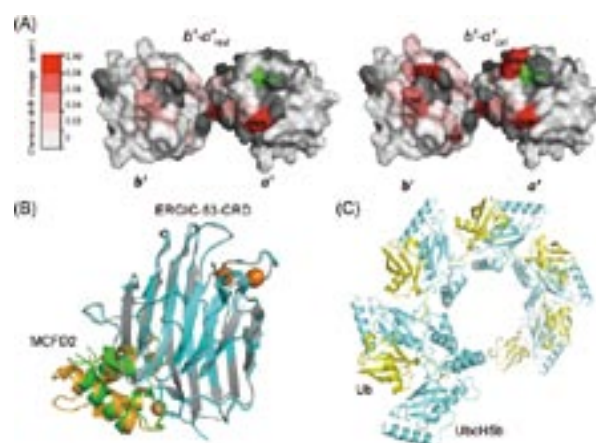


**Figure 2.** (A) Mapping on the 3D model of *b'*-*a'* (reduced form) of the residues whose chemical shift were perturbed upon binding with mastoparan (as a model ligand) in the reduced (left) and oxidized (right) forms of *b'*-*a'*. Red gradient indicates the strength of the perturbation. The proline residues and the residues whose <sup>1</sup>H-<sup>15</sup>N HSQC peak could not be used as a probe due to broadening and/or overlapping are shown in gray. The catalytic cysteine residues appear in green. (B) 3D structures of MCFD2 and ERGIC-53-CRD. Uncomplexed structures of rat ERGIC-53 (cyan) and human MCFD2 (orange) are superimposed on our crystal structure of the complex between human ERGIC-53 (gray) and MCFD2 (green). The bound calcium ions are shown as spheres. (C) Formation of the self-assembly of the UbcH5b~Ub conjugate through the backside interaction.

#### References

- 1) M. Utsumi, Y. Yamaguchi, H. Sasakawa, N. Yamamoto, K. Yanagisawa and K. Kato, *Glycoconjugate J.* **26**, 999–1006 (2009).
- 2) M. Yagi-Utsumi, T. Kameda, Y. Yamaguchi and K. Kato, *FEBS Lett.* **584**, 831–836 (2010).
- 3) E. Sakata, T. Satoh, S. Yamamoto, Y. Yamaguchi, M. Yagi-Utsumi, E. Kurimoto, K. Tanaka, S. Wakatsuki and K. Kato, *Structure* **18**, 138–147 (2010).
- 4) O. Serve, Y. Kamiya, A. Maeno, M. Nakano, C. Murakami, H. Sasakawa, Y. Yamaguchi, T. Harada, E. Kurimoto, M. Yagi-Utsumi, T. Iguchi, K. Inaba, J. Kikuchi, O. Asami, T. Kajino, T. Oka, M. Nakasako and K. Kato, *J. Mol. Biol.* **396**, 361–374 (2010).
- 5) M. Nishio, Y. Kamiya, T. Mizushima, S. Wakatsuki, H. Sasakawa, K. Yamamoto, S. Uchiyama, M. Noda, A. R. McKay, K. Fukui, H.-P. Hauri and K. Kato, *Proc. Natl. Acad. Sci. U. S. A.* **107**, 4034–4039 (2010).
- 6) M. Nakasako, A. Maeno, E. Kurimoto, T. Harada, Y. Yamaguchi, T. Oka, Y. Takayama, A. Iwata and K. Kato, *Biochemistry* **49**, 6953–6962 (2010).

# Structure-Function Relationship of Metalloproteins

Department of Life and Coordination-Complex Molecular Science  
Division of Biomolecular Functions



FUJII, Hiroshi  
KURAHASHI, Takuya  
CONG, Zhiqi  
NAKAGAWA, Takafumi  
WANG, Shunlan  
TANIZAWA, Misako

Associate Professor  
Assistant Professor  
IMS Fellow  
Post-Doctoral Fellow  
Graduate Student  
Secretary

Metalloproteins are a class of biologically important macromolecules, which have various functions such as oxygen transport, electron transfer, oxidation, and oxygenation. These diverse functions of metalloproteins have been thought to depend on the ligands from amino acid, coordination structures, and protein structures in immediate vicinity of metal ions. In this project, we are studying the relationship between the electronic structures of the metal active sites and reactivity of metalloproteins.

## 1. Unique Property and Reactivity of High-Valent Manganese-Oxo versus Manganese-Hydroxo in the Salen Platform<sup>1,2)</sup>

To gain an understanding of oxidation reactions by Mn<sup>III</sup>(salen), a reaction of Mn<sup>III</sup>(salen) with *m*-chloroperoxybenzoic acid in the absence of a substrate is investigated. UV-vis, perpendicular- and parallel-mode electron paramagnetic resonance and X-ray absorption spectroscopy show the resulting solution contains Mn<sup>IV</sup>(salen)(O) as a major product and Mn<sup>IV</sup>(salen)(OH) as a minor product. Mn<sup>IV</sup>(salen)(O) readily reacts with 4-H-2,6-*tert*-Bu<sub>2</sub>C<sub>6</sub>H<sub>2</sub>OH (BDE<sub>OH</sub> = 82.8 kcal/mol), 4-CH<sub>3</sub>CO-2,6-*tert*-Bu<sub>2</sub>C<sub>6</sub>H<sub>2</sub>OH (BDE<sub>OH</sub> = 83.1 kcal/mol) and 4-NC-2,6-*tert*-Bu<sub>2</sub>C<sub>6</sub>H<sub>2</sub>OH (BDE<sub>OH</sub> = 84.2 kcal/mol) at 203 K, following second-order rate kinetics (BDE<sub>OH</sub>; homolytic bond dissociation energy of an OH bond). Mn<sup>IV</sup>(salen)(OH) reacts with 4-CH<sub>3</sub>CO-2,6-*tert*-Bu<sub>2</sub>C<sub>6</sub>H<sub>2</sub>OH (BDE<sub>OH</sub> = 83.1 kcal/mol) much more slowly under the identical conditions than Mn<sup>IV</sup>(salen)(O), and does not react with 4-NC-2,6-*tert*-Bu<sub>2</sub>C<sub>6</sub>H<sub>2</sub>OH (BDE<sub>OH</sub> = 84.2 kcal/mol), suggesting thermodynamic hydrogen-atom abstracting ability of Mn<sup>IV</sup>(salen)(OH) is about 83 kcal/mol. The rate constant for reactions of Mn<sup>IV</sup>(salen)(OH) with phenols are not dependent on

the concentration of phenols, suggesting that Mn<sup>IV</sup>(salen)(OH) might bind phenols prior to the rate-limiting oxidation reactions. Quantum chemical calculations are carried out for Mn<sup>IV</sup>(salen)(O) and Mn<sup>IV</sup>(salen)(OH), both of which well reproduce the EXAFS structures as well as the electronic configurations. It is also indicated that protonation of Mn<sup>IV</sup>(salen)(OH) induces a drastic electronic structural change from Mn<sup>IV</sup>-phenolate to Mn<sup>III</sup>-phenoxyl radical, which is also consistent with the experimental observation.

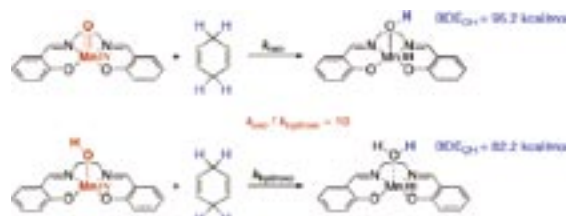


**Figure 1.** Hydrogen abstractions of oxo-manganese(IV) salen and hydroxy-manganese(IV) salen complexes.

## 2. Resonance Raman Study of a High-Valent Fe=O Porphyrin Complex as a Model for Peroxidase Compound II<sup>3)</sup>

Horseradish peroxidase (HRP) catalyzes the oxidation of organic substrates using H<sub>2</sub>O<sub>2</sub> as a specific oxidant. Upon reaction with H<sub>2</sub>O<sub>2</sub>, HRP sequentially forms two reaction intermediates known as compound I and compound II, before returning to the original ferric state. Compound I and compound II are respectively 2 and 1 oxidative equivalents higher than the Fe<sup>III</sup> state, and respectively correspond to the Fe<sup>V</sup> and Fe<sup>IV</sup> formal oxidation states. Compound II of HRP exhibits a ν<sub>Fe=O</sub> resonance Raman (RR) band at 775 and 787 cm<sup>-1</sup> at pH

7 and 11, respectively. The  $12\text{ cm}^{-1}$  upshift of the  $\nu_{\text{Fe=O}}$  mode of HRP compound II upon alkalization is caused by elimination of the hydrogen bond between the oxygen atom and the distal His and is regarded as a “distal effect.” The  $\nu_{\text{Fe=O}}$  mode of the  $\text{Fe}^{\text{IV}}$  state of myoglobin (Mb) at pH 8.5 is located at *ca.*  $800\text{ cm}^{-1}$  (sperm whale Mb at  $797\text{ cm}^{-1}$  and horse heart Mb at  $804\text{ cm}^{-1}$ ), where no hydrogen bond exists between the oxygen atom and the distal His. There is a  $13\text{ cm}^{-1}$  frequency difference in the  $\nu_{\text{Fe=O}}$  mode between HRP at  $787\text{ cm}^{-1}$  and Mb at  $800\text{ cm}^{-1}$ . This has been interpreted as a result of a “proximal effect.” Both HRP and Mb have a proximal His residue. However, the proximal His of HRP has the anionic character of imidazolate ( $\text{Im}^-$ ), while the proximal His of Mb is considered to be neutral.

Many  $\text{Fe=O}$  porphyrin model complexes with 1-methylimidazole (1MeIm) or a solvent molecule acting as the axial ligand have been prepared and characterized by RR spectroscopy, in order to obtain insights into the electronic structures and reactivities of hemoproteins. However, there have been no reports of model complexes with  $\text{Im}^-$  as a *trans* axial ligand. In the present study, we have prepared an  $\text{Fe=O}$  porphyrin model complex with  $\text{Im}^-$  as the axial ligand and identified the  $\nu_{\text{Fe=O}}$  mode at  $792\text{ cm}^{-1}$ , which is significantly lower than that of an analogous complex with 1MeIm as the axial ligand ( $815\text{ cm}^{-1}$ ). Thus, the imidazolate complex could be regarded as a model for compound II of HRP. The experimental details are described in Supporting Information.

### 3. Direct Probing of Spin State Dynamics Coupled with Electronic and Structural Modifications by Picosecond Time-Resolved XAFS<sup>4</sup>

Molecular magnetic systems such as nanomagnets and biological systems have attracted much interest in recent years. In disordered magnetic systems, where the spin system does not have macroscopic magnetization, it is crucial to directly observe the transient spin states to aid in the understanding and controlling of the dynamic magnetic properties. In studies of ultrafast spin dynamics, pico- and femtosecond time scales are now accessible with advanced optical pump-probe measurement using two ultrafast lasers. However, it is not trivial to deconvoluting the dynamics of the spin state from transient optical signal. Although the magneto-optical effect has been applied to macroscopic magnetization, it is difficult to apply in disordered magnetic systems. To overcome these difficulties, a pulsed hard X-ray has been utilized as a probe for the dynamics of the inner-atomic transitions.

The first direct observation of the transient spin-state in a disordered magnetic system with time-resolved XAFS is reported. By observing the evolution of the  $\text{Fe}^{\text{II}}$   $1s\text{--}3d$  transition, the spin crossover transition from the  $^1A_1$  low spin state to  $^5T_2$  high spin state has been directly observed on a picose-

cond time scale. Moreover, observation of the transient spin state with time-resolved XAFS allows for the investigation of the variations in the electronic state and molecular structure. This unique experimental technique probes the excited states involved in the ultrafast photoinduced reactions in disordered magnetic systems.

### 4. Paramagnetic $^{13}\text{C}$ and $^{15}\text{N}$ NMR Analyses of the Push- and Pull-Effects in Cytochrome *c* Peroxidase and *Coprinus cinereus* Peroxidase Variants: Functional Roles of Highly-Conserved Amino Acids around Heme<sup>5</sup>

Paramagnetic  $^{13}\text{C}$  and  $^{15}\text{N}$  nuclear magnetic resonance (NMR) spectroscopy of heme-bound cyanide ( $^{13}\text{C}^{15}\text{N}$ ) was applied to 11 cytochrome *c* peroxidase (CcP) and *Coprinus cinereus* peroxidase (CIP) mutants to investigate contributions to the push- and pull-effects of conserved amino acids around heme. The  $^{13}\text{C}$  and  $^{15}\text{N}$  NMR data for the distal His and Arg mutants indicated that distal His is the key amino acid residue creating the strong pull-effect and that distal Arg assists. The mutation of distal Trp of CcP to Phe, the amino acid at this position in CIP, changed the push- and pull-effects close to those of CIP, whereas the mutation of distal Phe of CIP to Trp changed this mutant to become CcP-like. The  $^{13}\text{C}$  NMR shifts for the proximal Asp mutants clearly showed that the proximal Asp-His hydrogen-bonding increase the push-effect. However, even in absence of a hydrogen-bond the push-effect of proximal His in peroxidase is significantly stronger than in globins. Comparison of the present NMR data with the compound I formation rate constants and crystal structures of these mutants showed that (1) the base catalysis of the distal His is more critical for rapid compound I formation than its acid catalysis, (2) the primary function of the distal Arg is to maintain the distal heme pocket in favor of rapid compound I formation via hydrogen-bonding, and (3) the push-effect is the major contributor to the differential rates of compound I formation in wild-type peroxidases.

#### References

- 1) T. Kurahashi, M. Hada and H. Fujii, *J. Am. Chem. Soc.* **131**, 12394–12405 (2009).
- 2) T. Kurahashi, A. Kikuchi, Y. Shiro, M. Hada and H. Fujii, *Inorg. Chem.* **49**, 6664–6672 (2010).
- 3) H. Ishimaru, H. Fujii and T. Ogura, *Chem. Lett.* **39**, 332–333 (2010).
- 4) S. Nozawa, T. Sato, M. Chollet, K. Ichyanagi, A. Tomita, H. Fujii, S. Adachi and S. Koshihara, *J. Am. Chem. Soc.* **132**, 61–63 (2010).
- 5) D. Nonaka, H. Wariishi and H. Fujii, *Biochemistry* **49**, 49–57 (2010).

# Fabrication of Silicon-Based Planar Ion-Channel Biosensors and Integration of Functional Cell Membrane Model Systems on Solid Substrates

Department of Life and Coordination-Complex Molecular Science  
Division of Biomolecular Sensing



URISU, Tsuneo  
TERO, Ryugo  
WANG, Zhihong  
RAHMAN, Mashiur  
ASANO, Toshifumi  
NAGAIRO, Takeshi  
NAGAOKA, Yasutaka  
UNO, Hidetaka  
NAKAI, Naohito  
SHANG, Zhi-Guo  
FUJIWARA, Kuniyo  
SHIMIZU, Atsuko

Professor  
Assistant Professor  
Post-Doctoral Fellow  
Post-Doctoral Fellow  
Post-Doctoral Fellow  
Post-Doctoral Fellow  
Research Fellow  
Graduate Student  
Graduate Student  
Graduate Student  
Graduate Student  
Secretary

We are interested in the investigation of cell membrane surface reactions and the pathogen mechanism of the neurodegenerative diseases, based on the molecular science. We are advancing two subjects, aiming the creation and development of new molecular science field, “medical molecular science.” One is the development of ion channel biosensor and its application to the neural network analyzer device. The other is the fundamental understanding of bilayer membrane properties using the artificial lipid bilayers on solid substrates, which is called supported bilayers, by means of atomic force microscope and fluorescence microscope-based techniques.

## 1. Development of Neural Network Device and Precise Microfabrications

We have successfully developed the neural cell device which emits the action potential by the photo-stimulation using a photo-receptor ion channel protein and the ion channel biosensor as the detector of the action potential. As an application of these elementary devices, we are now developing the neural cell network devices, using the state-of-the-art precision work combining the superprecision machining, the hot emboss technology, and the LIGA process. The high precision fabri-

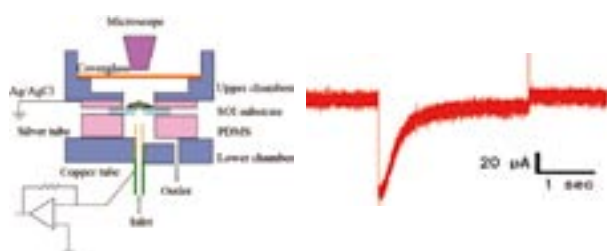


**Figure 1.** Structure of ion channel biosensor, and the observed channel current gated by laser irradiation. Chr2 is expressed on the C2C12 cell set on the biosensor substrate.

cation technology will bring a significant breakthrough into the brain science.

## 2. Surface-Induced Phase Separation of Sphingomyelin/Cholesterol/Ganglioside GM1-Planar Bilayer on Mica Surfaces and Microdomain Molecular Conformation that Accelerates A $\beta$ Oligomerization

Ganglioside GM1 mediates the amyloid beta (A $\beta$ ) aggregation that is the hallmark of Alzheimer’s disease (AD). To investigate how ganglioside-containing lipid bilayers interact with A $\beta$ , we examined the interaction between A $\beta$ 40 and supported planar lipid bilayers (SPBs) on mica and SiO<sub>2</sub> substrates using atomic force microscopy, fluorescence microscopy, and molecular dynamics computer simulations. These SPBs contained several compositions of sphingomyelin, cholesterol, and GM1 which covers compositions commonly seen in eukaryotic biomembranes and were treated at physiological salt concentrations. Surprisingly high speed A $\beta$  aggregations of fibril formation were induced for all GM1 concentrations examined on the mica surface, but only globular agglomerates are formed slowly on the SiO<sub>2</sub> surfaces. Especially for the 20 mol% GM1 concentration on the mica surface, unique triangular domains were formed and the high speed A $\beta$  aggregations were observed only outside of the triangular domains. We have found that some unique surface-induced phase separations are induced due to the GM1 clustering effects and the strong interactions between the GM1 head group and the water layer adsorbed in the ditrigonal cavities on the mica surface. The speed of A $\beta$ 40 aggregation and the shape of the agglomerates depend on the molecular conformation of GM1, which varies depending on the substrate materials. We identified the conformation that significantly accelerates A $\beta$ 40 aggregation, and we think that the detailed knowledge about the GM1 molecular



conformation obtained in this work will be useful to those investigating A $\beta$ -GM1 interactions.<sup>1)</sup>

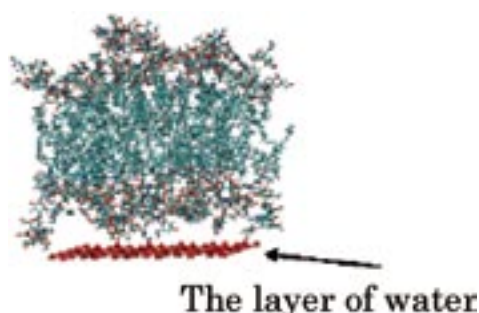


**Figure 2.** Starting model of the calculation, including the substrate effects. CHOL/GM1 (50:50)-SPB sitting on a layer of water molecules trapped in the ditrigrinal cavities with 0.52-nm spacing of the mica surface.

### 3. Clustering Effects of GM1 and Formation Mechanisms of Interdigitated Liquid Disordered Domains in GM1/SM/CHOL-Supported Planar Bilayers on Mica Surface

We investigate the formation mechanisms of the interdigitated liquid disordered domain (ILDD), which is observed in the ganglioside (GM1)/sphingomyelin (SM)/cholesterol (CHOL) bilayers on a mica surface and accelerates the formation of fibrillar A $\beta$  agglomerates, using molecular dynamics computer simulations and atomic force microscopy. The ILDD structure is stable both on mica and SiO<sub>2</sub> surfaces, but it is observed only on the mica surface. We conclude that the phase separation of SM- and GM1-rich domains is induced by GM1 clustering and the interaction between the GM1 head group and the water layer adsorbed in the ditrigrinal cavity on the mica surface.

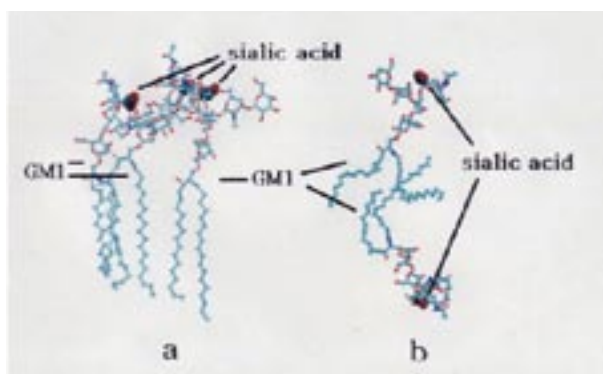


**Figure 3.** Molecular structures of GM1 and SM in the lipid bilayer of GM1<sub>x</sub>/SM<sub>32-x</sub>/CHOL<sub>32</sub> on the mica surface, for  $x = 16$  (a) and  $24$  (b) after 10-ns simulation.

### 4. Anomalous Diffusion in Supported Lipid Bilayers Induced by Nanostructures on Substrate Surfaces

Lateral organization and diffusion of lipids and membrane proteins are crucial factors of biological reactions on cell membranes such as signal transduction and cell recognition. We have observed directly the lipid diffusion in supported lipid bilayers (SLBs) by single molecule tracking (SMT) method. SMT measurement of fluorescent dye-labeled lipid (lissamine rhodamine B labeled dipalmitoyl-phosphatidylethanolamine; Rb-DPPE,  $E_x/E_m = 557 \text{ nm}/571 \text{ nm}$ ) in dioleoylphosphatidylcholine (DOPC)-SLBs on thermally oxidized SiO<sub>2</sub>/Si(100) and step-and-terrace TiO<sub>2</sub>(100) surfaces was performed by diagonal illumination method applying an objective type total internal reflection fluorescence microscope. The SiO<sub>2</sub> surface has amorphous structure of  $\sim 1 \text{ nm}$  at peak-to-valley. The step-and-terrace TiO<sub>2</sub>(100) surface has linear atomic steps at 550 nm interval, and 50–300 nm oval pits surrounded by an atomic step exists in terraces. Diffusion of Rb-DPPE in the DOPC-SLBs on SiO<sub>2</sub>/Si(100) and TiO<sub>2</sub>(100) surfaces were recorded at the time resolution ranging from 497  $\mu\text{s}$  (2011 fps) to 30 ms (33 fps), and the diffusion coefficients on various time scale were evaluated from the time evolution of mean square displacement ( $\langle r^2 \rangle$ ). The diffusion coefficients ( $D$ ) of Rb-DPPE decreased with diffusion length, and their tendency depend on the substrate nanostructures (Figure 4). On TiO<sub>2</sub>(100) decrease in diffusion coefficient ( $D$ ) is observed at the mean diffusion distance ( $\sqrt{\langle r^2 \rangle}$ ) less than 400 nm, which corresponds to the interval of the atomic steps. We attribute this anomalous diffusion to the surface atomic steps on the TiO<sub>2</sub>(100) surface.

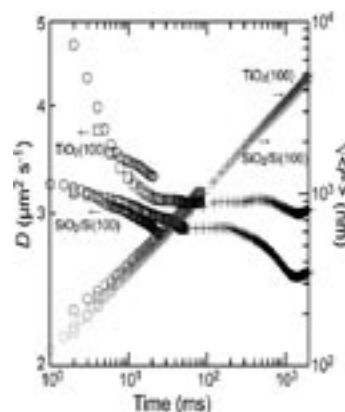


**Figure 4.** Time dependence of the diffusion coefficients ( $D$ ) of Rb-DPPE and the mean diffusion distance ( $\sqrt{\langle r^2 \rangle}$ ).

#### Reference

- 1) Y.-Li. Mao, Z.-G. Shang, Y. Imai, T. Hoshino, R. Tero, M. Tanaka, N. Yamamoto, K. Yanagisawa and T. Urisu, *Biochim. Biophys. Acta, Biomemb.* **1798**, 1090–1099 (2010).

#### Awards

TERO, Ryugo; CSJ Presentation Award 2010.

UNO, Hidetaka; 3<sup>rd</sup> International Symposium of Nano-medicine, Young Scientist Award.

# Investigation of Molecular Mechanisms of Transporters and Receptors in Membrane by Using Stimulus-Induced Difference FT-IR Spectroscopy

Department of Life and Coordination-Complex Molecular Science  
Division of Biomolecular Sensing



FURUTANI, Yuji  
KIMURA, Tetsunari  
GUO, Hao  
SHIMIZU, Atsuko

Associate Professor  
Assistant Professor  
Graduate Student  
Secretary

Membrane proteins are important for homeostasis of living cells, which work as ion channel, ion pump, various types of chemical and biophysical sensors, and so on. These proteins are considered as one of important targets for biophysical studies. However, their molecular mechanisms have not been studied well, because X-ray crystallography and NMR spectroscopy are hard to access them in general.

Our main goal is to clarify molecular mechanisms of transporters and receptors in cell membrane mainly by using stimulus-induced difference infrared spectroscopy which is sensitive to the structural and environmental changes of organic and bio-molecules.

Our research group was launched in 2009 and has been setting up experimental equipments.

## 1. Time-Resolved FT-IR Spectroscopy Detecting O–H and O–D Stretching Vibrations of Light-Driven Proton and Chloride-Ion Pump Proteins

Bacteriorhodopsin (bR) is one of well known light-driven proton pump protein, which has an all-*trans* retinal as a chromophore. Upon the light absorption, photo-isomerization of the retinal occurs from the all-*trans* to 13-*cis* form in less than one picosecond, followed by a cyclic reaction that comprises a series of intermediates, called as the K, L, M, N, and O states, back to the bR ground state (BR).

Hydration level of bR film samples are optimized by dropping the deuterium glycerol/water drops (20% v/v) around the sample. This sample preparation allowed us to collect the accurate light-induced difference FT-IR spectra (3850 to 1000  $\text{cm}^{-1}$ ) including the X–H and X–D stretching regions, corresponding to the structural changes in the hydrophobic and hydrophilic parts, respectively. By analyzing these spectral

Time-resolved light-induced difference FT-IR spectroscopy in IMS

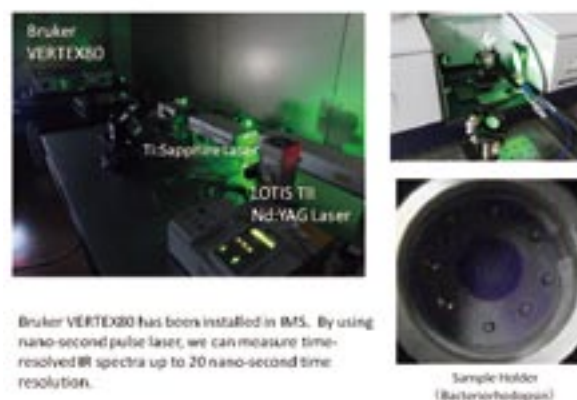


Figure 1. Light-induced difference FT-IR measurement system.

changes, real-time hydrogen-bonding changes of internal water molecules and protein moiety of BR will be elucidated, leading to better understand of the light-driven proton pumping mechanism of BR.

Dr. Kimura joined our group in Dec. 2009 and started to measure time-resolved infrared spectra of a light-driven chloride-ion pump, *pharaonis* halorhodopsin (*pHR*). The previous low-temperature FT-IR measurement revealed that the specific interaction among a chloride ion, the protonated Schiff base and internal water molecules changes upon the formation of K, L<sub>1</sub> and L<sub>2</sub> intermediates [Shibata *et al.*, *Biochemistry* **44**, 12279 (2005).] However, the structures in the later intermediates, such as N, O, and *pHR'* are still unclear. In this study, we applied time-resolved FT-IR difference spectroscopy on *pHR* at 12.5  $\mu\text{s}$  time resolution. As a result, we found that the H/D unexchangeable X–H groups showed two negative peaks at 3289 and 3315  $\text{cm}^{-1}$  in amide A region, with different decay kinetics. The former band was decayed with the time

constant of 4.2 ms, but the latter decay was fitted with the two time constants of 700  $\mu$ s and 6.2 ms. The faster and slower phases correspond to the conformational changes from  $L_2$  to  $[N \leftrightarrow O]$  states accompanying chloride release and from  $[N \leftrightarrow O]$  to  $pHR'$  involving chloride uptake, respectively.

## 2. Perfusion-Induced Difference FT-IR Spectroscopy Investigating Ion Binding Sites of Membrane Proteins

Recently, it has been demonstrated that stimulus-induced attenuated total reflection (ATR) FT-IR spectroscopy is one of the promising techniques for the investigation of the molecular mechanism of membrane proteins.

ATR FT-IR spectroscopy is a useful technique to obtain infrared spectra of membrane proteins immersed in aqueous solution. By exchanging buffer with and without salts, the difference spectra between the two conditions provide the structural information relating to the interaction change between membrane proteins and ions, especially around the ion binding site. We first applied this technique to a component of a flagellar motor protein complex, PomA/PomB, which forms ion channels passing  $Na^+$  ions to drive the rotation of flagella. We revealed that Asp24 is deprotonated upon binding of  $Na^+$  ion to PomA/PomB and is involved in an  $Na^+$  pathway, which probably reduces the energetic barrier formed in the inside of the hydrophobic channel.<sup>1)</sup>

Application of this ATR FT-IR to other membrane proteins, such as an ion channel (KcsA) and a transporter protein (V-

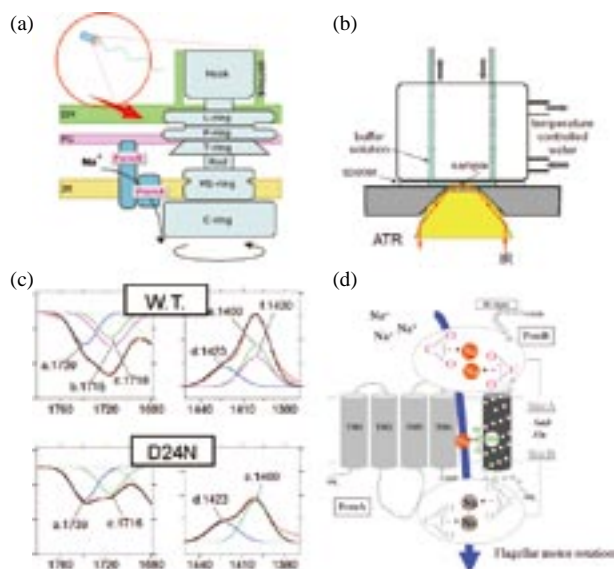


**Figure 2.** Sodium-ion binding induced difference FT-IR spectroscopy for a flagellar motor protein. (a) Schematic figure of supramolecular complex of flagellar motor. (b) A sample holder for perfusion-induced difference FT-IR spectroscopy. (c) COOH and COO<sup>-</sup> vibrations observed upon dissociation and binding of sodium ions, respectively. One of them was assigned to Asp24. (d) The proposed mechanism for sodium-ion flux through the PomA/PomB complex.

ATPase), started before coming to IMS. It has been succeeded to measure the difference infrared spectra between the conditions of several types of ions and pH. Based on these spectra, the molecular mechanism of recognition and transportation of ions will be discussed in near future.

In Apr. 2010, a graduate student, Mr. Guo, joined our group and started to construct an ATR FT-IR measurement system with surface-enhanced technique. He has succeeded to make thin gold films by vapor deposition method and observed the AFM images. The surface enhancement of raman scattering from pyridine solution was confirmed by raman microscopy. In future, we will make a thin gold film on an ATR crystal, attach membrane proteins on the surface and measure the light and perfusion-induced difference FT-IR spectra.

## 3. FT-IR Studies for Revealing Molecular Mechanisms of Visual Rhodopsins

In our vision, rhodopsin works in the dim light and cone pigments in the daylight. The former is specialized for scotopic vision and the latter is for discriminating color.

We found that Thr118-OH group of bovine rhodopsin is utilized for an internal molecular probe to investigate protein fluctuation.<sup>2)</sup> By monitoring a slow hydrogen/deuterium exchange (HDX) of the Thr118-OH group under native conditions and analyzing the data through the precise mathematical statistics, we proposed a quantitative two-step model in which the dark activation of rhodopsin is triggered by thermal isomerization of the retinal in a transiently opened conformation.

The red and green cone pigments from primate were heterologously expressed in HEK293 cells, purified by affinity chromatography, and then reconstituted in phosphatidylcholine (PC) liposomes. By using low-temperature FT-IR spectroscopy, the structural changes upon the retinal isomerization were analyzed and the molecular mechanism of red and green color discrimination was discussed.<sup>3)</sup>

### Acknowledgements

We thank many collaborators, especially Profs. Hideki Kandori (Nagoya Institute of Technology), Michio Homma, Yuki Sudo (Nagoya University) and Hiroo Imai (Kyoto University). We also thank Prof. Yakushi's group for use of the vapor deposition apparatus and raman spectrometer. We also thank Prof. Urisu's group for use of AFM.

### References

- 1) Y. Sudo, Y. Kitade, Y. Furutani, M. Kojima, S. Kojima, M. Homma and H. Kandori, *Biochemistry* **48**, 11699–11705 (2009).
- 2) V. A. Lórenz-Fonfría, Y. Furutani, T. Ota, K. Ido and H. Kandori, *J. Am. Chem. Soc.* **132**, 5693–5703 (2010).
- 3) K. Katayama, Y. Furutani, H. Imai and H. Kandori, *Angew. Chem., Int. Ed.* **49**, 891–894 (2010).

# Heterogeneous Catalytic Systems for Organic Chemical Transformations

Department of Life and Coordination-Complex Molecular Science  
Division of Complex Catalysis



UOZUMI, Yasuhiro  
OSAKO, Takao  
HAMASAKA, Go  
ZHOU, Haifeng  
BEPPU, Tomohiko  
WATANABE, Toshihiro  
KOBAYASHI, Noboru  
MUTO, Tsubasa  
TORII, Kaoru  
TAZAWA, Aya  
SASAKI, Tokiyo  
FUKUSHIMA, Tomoko

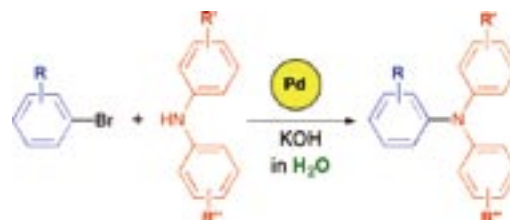
Professor  
Assistant Professor  
Post-Doctoral Fellow  
Post-Doctoral Fellow  
Graduate Student  
Graduate Student  
Graduate Student  
Graduate Student  
Technical Fellow  
Technical Fellow  
Secretary  
Secretary

Various organic molecular transformations catalyzed by transition metals were achieved under heterogeneous conditions by use of amphiphilic resin-supported palladium complexes, palladium membrane-installed microchannel devices, or self-supported bipyridyl–palladium complexes which were designed and prepared by this research group. In particular, Buchwald-Hartwig reaction, Suzuki-Miyaura coupling, and aerobic alcohol oxidation, which were performed in water under heterogeneous conditions with high recyclability of the polymeric catalysts, are highlights among the achievements of the 2009–2010 period to approach what may be considered ideal chemical processes of next generation. Representative results are summarized hereunder.

## 1. Clean Synthesis of Triarylamines: Buchwald-Hartwig Reaction in Water with Amphiphilic Resin-Supported Palladium Complexes<sup>1,2)</sup>

Catalytic aromatic amination was achieved in water under heterogeneous conditions by the use of immobilized palladium complexes coordinated with the amphiphilic polystyrene-poly(ethylene glycol) resin-supported di(*tert*-butyl)phosphine ligand. Aromatic amination of aryl halides with diphenylamine and *N,N*-double arylation of anilines with bromobenzene were

found to proceed in water with broad substrate tolerance to give the triarylamines in high yield with high recyclability of the polymeric catalyst beads. Very little palladium leached from the polymeric catalyst under the water-based reaction conditions to provide a green and clean (metal-uncontaminated) protocol for the preparation of triarylamines, including the optoelectronically active *N,N,N',N'*-tetraaryl-1,1'-biphenyl-4,4'-diamines (TPDs).

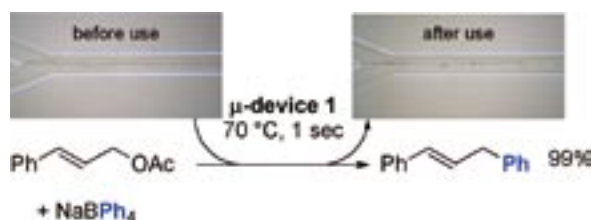


Scheme 1. Buchwald-Hartwig Reaction in Water with Amphiphilic Resin-Supported Palladium Complexes.

## 2. Palladium Membrane-Installed Microchannel Devices for Instantaneous Suzuki–Miyaura Cross-Coupling and Allylic Arylation<sup>3,4)</sup>

Instantaneous catalytic carbon–carbon bond-forming reac-

tions were achieved in catalytic membrane-installed microchannel devices that have a polymeric palladium-complex membrane. The catalytic membrane-installed microchannel devices were provided inside the microchannels by means of coordinative and ionic molecular convection at the interface between the organic and aqueous phases flowing laminarily, in which both non-crosslinked linear polymer ligands and palladium species dissolved. The palladium-catalyzed Suzuki–Miyaura reaction of aryl, heteroaryl, and alkenyl halides with arylboronic acids and sodium tetraarylborates was performed with the catalytic membrane-installed microchannel devices to give quantitative yields of biaryls, heterobiaryls, and aryl alkenes within 5 s of residence time in the defined channel region. These microchannel devices were applied to the instantaneous allylic arylation reaction of allylic esters with arylboron reagents under microflow conditions to afford the corresponding coupling products within 1 s of residence time.



**Scheme 2.** Instantaneous Allylic Arylation with Palladium Membrane-Installed Microchannel Devices.

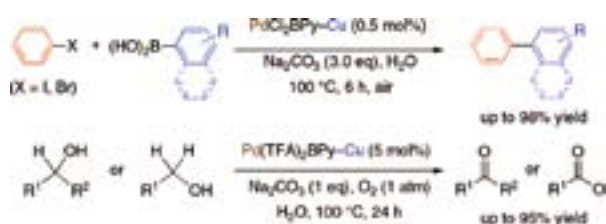
### 3. Suzuki–Miyaura Coupling and Aerobic Alcohol Oxidation in Water with Self-Supported Bipyridyl–Palladium Complexes<sup>5,6)</sup>

Self-supported bipyridyl–palladium catalysts ( $\text{PdX}_2\text{BPy–Cu}$ ) were developed *via* construction of metal–organic frame-

works (MOFs) of bipyridyl–palladium complexes bearing carboxylic groups and  $\text{Cu}(\text{NO}_3)_2 \cdot 3\text{H}_2\text{O}$  (Scheme 3). The self-supported catalysts efficiently catalyzed the aerobic oxidation of benzylic alcohols and the Suzuki–Miyaura coupling of phenyl halides with arylboronic acids in water to give the corresponding products in high yield (Scheme 4). The catalysts were reused without a loss of catalytic activity.



**Scheme 3.** Preparation of Self-Supported Bipyridyl–Palladium Complexes *via* Construction of Metal–Organic Frameworks (MOFs).



**Scheme 4.** Suzuki–Miyaura Coupling and Aerobic Alcohol Oxidation in Water with Self-Supported Bipyridyl–Palladium Complexes.

#### References

- 1) Y. Hirai and Y. Uozumi, *Chem. Commun.* **46**, 1103–1105 (2010).
- 2) Y. Hirai and Y. Uozumi, *Chem. –Asian J.* **5**, 1788–1795 (2010) (Frontispiece Article).
- 3) Y. M. A. Yamada, T. Watanabe, K. Torii and Y. Uozumi, *Chem. Commun.* 5594–5596 (2009) (Hot Article).
- 4) Y. M. A. Yamada, T. Watanabe, T. Beppu, N. Fukuyama, K. Torii and Y. Uozumi, *Chem. –Eur. J.* **16**, 11311–11319 (2010).
- 5) T. Osako and Y. Uozumi, *Chem. Lett.* **38**, 902–903 (2009).
- 6) T. Osako and Y. Uozumi, *Heterocycles* **80**, 505–514 (2010).

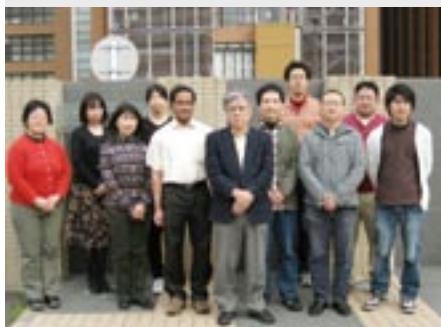
#### Awards

UOZUMI, Yasuhiro; The 26<sup>th</sup> Inoue Prize for Science.

HAMASAKA, Go; CSJ Presentation Award 2010.

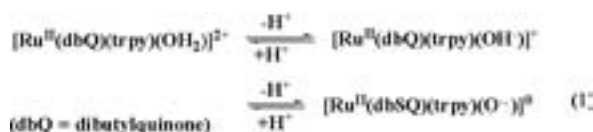
# Synthesis of Metal Complexes Aiming at Storage and Release of Chemical Energy

Department of Life and Coordination-Complex Molecular Science  
Division of Functional Coordination Chemistry



TANAKA, Koji	Professor
OHTSU, Hideki	Assistant Professor
KOBAYASHI, Katsuaki	IMS Research Assistant Professor
SUMANTA, Kumar	Post-Doctoral Fellow
BAI, Zhengshuai	Post-Doctoral Fellow
MIYAJI, Mariko	Post-Doctoral Fellow
TSUKAHARA, Yuhei	Graduate Student
DOYAMA, Yuko	Technical Fellow
YAMAGUCHI, Yumiko	Secretary
NOGAWA, Kyoko	Secretary

Metal complexes that have an ability to oxidize H<sub>2</sub> and alcohols at potentials more negative than reduction of dioxygen are feasible electrode catalysts in H<sub>2</sub>/O<sub>2</sub> and alcohol/O<sub>2</sub> fuel cells. Electrochemical oxidation of Ru<sup>II</sup>(polypyridyl)(OH<sub>2</sub>) is accompanied by deprotonation to produce the correspondent Ru<sup>IV</sup>=O and Ru<sup>V</sup>=O complexes. Those high valent Ru=O complexes are expected for an application to electrode catalysts in fuel cells, since they have an ability to oxidize of some of organic molecules. However, intrinsic highly positive redox potentials for the generation of the active species does not meet a requirement to convert chemical energy of H<sub>2</sub> and alcohols to electricity. On the other hand, introduction of dioxolene ligands into Ru-aqua complexes results in spontaneous deprotonation of the aqua ligand, and unusual Ru-oxyl radical complexes are formed due to intra-molecular charge transfer from the resultant O<sup>2-</sup> ligand to dioxolene (eq. 1). Oxyl radical complexes formed in eq. 1 are expected to have an ability of not only abstraction of hydrogen atom of C–H bonds of alcohols but also formation of oxygen–oxygen bond

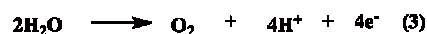
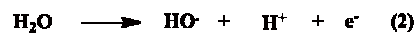


in the four-electron oxidation of water. Oxidations of alcohols and water under mild conditions would play the key role in the energy conversion to construct a sustainable society.

## 1. Substituents Dependent Capability of Bis(ruthenium-dioxoleneterpyridine) Complexes toward Water Oxidation

Water splitting to H<sub>2</sub> and O<sub>2</sub> driven by visible light is an

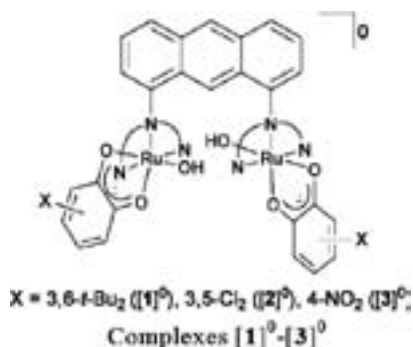
ultimate energy conversion from sunlight to a storable chemical energy. Water splitting using semiconductors under visible light irradiation has been well documented so far. Relatively low quantum efficiencies (~5%) in those reactions are ascribed to a reaction path through highly energetic one electron water oxidation that takes place at quite positive potentials (+2.31 V vs. NHE, pH 7, eq. 2). Accordingly, developments of efficient catalysts that have an ability to catalyze four-electron oxidation of water opens a door leading to an energetically sustainable society because four-electron water oxidation thermodynamically occurs at much more modest potentials (+0.815 V, eq. 3).



Recently, water oxidation using transition metal complexes has been intensively studied, though the reaction mechanism, especially the step of O–O bond formation from two water molecules, still remains unclear. Furthermore, Ce(IV) was used as an oxidant in most of water oxidation reactions. Taking into account that Ce(IV) is available as an oxidant only in very strong acidic aqueous solutions, electrochemical oxidation of water has various advantages not only to regulate the reaction conditions such as pH, applied potentials, and solvents but also to keep track of efficiencies and durability of catalysts by a change of catalytic currents during the reactions.

Dioxolene coordinated on metals take three redox states; quinone (q), semiquinone (sq), and catechol (cat). Among various metal-dioxolene complexes, ruthenium complexes in particular show strong interactions between Ru and dioxolene because of close energy levels of the dπ orbital of Ru to π and π\* orbitals of dioxolene. Furthermore, three oxidation states of dioxolene are able to coordinate on Ru<sup>II</sup>, Ru<sup>III</sup> and Ru<sup>IV</sup>, but

strict classification of those nine redox isomers (3×3) is practically impossible due to close energy levels of HOMO and LUMO energy levels of the metal and ligand. For example, the actual electronic structure of  $[\text{Ru}(\text{OAc})(\text{dioxolene})(\text{trpy})]^0$  ( $\text{trpy} = 2,2':4',2''\text{-terpyridine}$ ) gradually changes from the canonical  $\text{Ru}^{\text{II}}(\text{sq})$  configuration to the  $\text{Ru}^{\text{III}}(\text{cat})$  one with increasing electron withdrawing ability of dioxolene substituents. We have reported that a dinuclear ruthenium complex  $[\text{Ru}_2(\text{OH})_2(3,6\text{-}t\text{-Bu}_2\text{q})_2(\text{btpyan})](\text{SbF}_6)_2$  ( $[\mathbf{1}]^{2+}$ ,  $3,6\text{-}t\text{-Bu}_2\text{q} = 3,6\text{-di-}t\text{-butyl-1,2-benzoquinone}$ ,  $\text{btpyan} = 1,8\text{-bis}(2,2':6',2''\text{-terpyrid-4'-yl)anthracene}$ ) work as an excellent catalyst in the four-electron oxidation of water, since the electrochemical oxidation of water using an ITO electrode modified with  $[\mathbf{1}](\text{SbF}_6)_2$  evolved large amounts of  $\text{O}_2$  (33,500 turn-overs) at pH 4 (buffered) in  $\text{H}_2\text{O}$ . In the electrochemical oxidation of water catalyzed by  $[\mathbf{1}]^{2+}$ , redox reactions of dioxolene ligands play the central roles in not only the store of the electrons generated by proton dissociation of the hydroxyl group but also release of them to ITO electrode. However, the actual oxidation state of the Ru atom and dioxolene ligands in the catalytic cycle, and the process of the oxygen-oxygen bond formation prior to  $\text{O}_2$  evolution still remain unclear. We, therefore, prepared bis(ruthenium-hydroxo) complexes having dichloro ( $[\mathbf{2}]^0$ ) and  $\text{NO}_2$  ( $[\mathbf{3}]^0$ ) substituted dioxolene, and compared the redox behavior among  $[\mathbf{1}]^0$ ,  $[\mathbf{2}]^0$ , and  $[\mathbf{3}]^0$  to elucidate the role of dioxolene ligand in water oxidation.



The electronic structure of  $[\mathbf{1}]^0$  is expressed by  $[(\text{sq})\text{Ru}^{\text{II}}(\text{OH})(\text{HO})\text{Ru}^{\text{II}}(\text{sq})]^0$ . The catalytic cycle of water oxidation by  $[\mathbf{1}]^0$  is explained by the following stepwise reactions (i) two-electron oxidation of  $[\mathbf{1}]^0$  produces  $[(\text{q})\text{Ru}^{\text{II}}(\text{OH})(\text{HO})\text{Ru}^{\text{II}}(\text{q})]^{2+}$  ( $[\mathbf{1}]^{2+}$ ), (ii) dissociation of protons coupled with electron transfer to q generates  $[(\text{sq})\text{Ru}^{\text{II}}(\text{O}^{\cdot-})(^{\cdot-}\text{O})\text{Ru}^{\text{II}}(\text{sq})]^0$ , (iii) coulomb repulsion between two  $\text{O}^{\cdot-}$  ligands are removed by oxidation of sq, which facilitates to form O–O bond by a radical coupling reaction, (iv) an attack of water to a Ru atom is induced by oxidation of the complex, which cleaves one of the resultant Ru–O–O–Ru bond, (v) the second attack of water to another Ru atom release  $\text{O}_2$  with regeneration of  $[\mathbf{1}]^{2+}$ . On the other hand, the electronic structures of  $[\mathbf{2}]^0$  and  $[\mathbf{3}]^0$  are

approximated by  $[(\text{cat})\text{Ru}^{\text{III}}(\text{OH})(\text{HO})\text{Ru}^{\text{III}}(\text{cat})]^0$ . Two-electron oxidation of the latter takes place on metal center to give  $[(\text{cat})\text{Ru}^{\text{IV}}=\text{O}=\text{O}=\text{Ru}^{\text{IV}}(\text{cat})]^0$  rather than ligand centered oxidation affording  $[(\text{sq})\text{Ru}^{\text{III}}(\text{OH})(\text{HO})\text{Ru}^{\text{III}}(\text{sq})]^{2+}$ . It is considered that the O–O bond formation in  $[(\text{cat})\text{Ru}^{\text{IV}}=\text{O}=\text{O}=\text{Ru}^{\text{IV}}(\text{cat})]^0$  is very hard due to the stability of the  $(\text{cat})\text{Ru}^{\text{IV}}=\text{O}$  moiety. Indeed, the complexes  $[\mathbf{2}]^0$  and  $[\mathbf{3}]^0$  practically did not evolve  $\text{O}_2$  under the electrolysis up to +2.20 V (vs. SCE) in  $\text{H}_2\text{O}$ .

## 2. A New Type of Electrochemical Oxidation of Alcohols Mediated with a Ruthenium-Dioxolene-Amine Complex in Neutral Water

The present society is maintained by combustion of tremendous amounts of fossil fuels and consumption of natural resources without regeneration of them. Global industrialization since 19 century inevitably has caused serious depletion of natural resources and environmental damages. As a result, energy conversion from natural energy to chemical one is believed as the top research area to build a sustainable society. Both  $\text{H}_2/\text{O}_2$  and direct methanol ( $\text{CH}_3\text{OH}$ ) fuel cells have the great feasibility as future energy sources. A key issue in practical uses of fuel cells is that only platinum or platinum-based alloys have been used as  $\text{H}_2$  and  $\text{CH}_3\text{OH}$  oxidation electrodes. It is, therefore, highly desired to develop metal complexes that have an ability to oxidize  $\text{H}_2$  and  $\text{CH}_3\text{OH}$  under mild conditions in place of platinum metal.

Aminyl radicals ( $\text{NR}_2^{\cdot}$ ) that are known as reactive reaction intermediates abstract hydrogen atoms of various organic molecules. Some of those radicals are stabilized on metal complexes and successfully isolated. Recently, we have demonstrated that deprotonation of amino group of  $\text{Ru}(\text{dioxolene})$  (amine) (dioxolene = 3,5-di-*tert*-butyl-1,2-benzoquinone (q), -semiquinonate (sq), and -catecholate (cat)) reversibly produces the correspondent aminyl radical complex due to an intra-molecular electron transfer between deprotonated amino group and dioxolene ligand. Although aminyl radical metal complexes hardly showed a catalytic activity for oxidation of organic molecules, two-electron oxidation of those complexes creates catalytic ability to oxidize alcohols. This fact has driven us to examine a potential application for electrocatalysts of oxidation of  $\text{CH}_3\text{OH}$  in aqueous conditions by considering smooth conversion between aminyl radical and amino groups on Ru. So, we examined the redox behavior of the  $[\text{Ru}^{\text{II}}(\text{terpy})(\text{sq})(\text{NH}_3)]^+ / [\text{Ru}^{\text{II}}(\text{terpy})(\text{q})(\text{NH}_3)]^{2+}$  (terpy = 2,2':6',2''-terpyridine) couple (abbreviated as  $[\text{Ru}^{\text{II}}(\text{sq})(\text{NH}_3)]^+ / [\text{Ru}^{\text{II}}(\text{q})(\text{NH}_3)]^{2+}$ ) in the absence and presence of a base in  $\text{CH}_3\text{OH}$  and in  $\text{H}_2\text{O}$ , and found an unprecedented two-electron oxidant character created by proton and electron loss of  $[\text{Ru}^{\text{II}}(\text{q})(\text{NH}_3)]^{2+}$  in the oxidation of alcohols in neutral water.

# Visiting Professors



Visiting Professor  
**NISHIHARA, Hiroshi** (*from The University of Tokyo*)

### Coordination Programming of Electro-Functional Materials

One goal of molecular electronics is to control electron conduction in molecular wires and networks by combining appropriate molecular units. To evaluate the total performance of the molecular wires, we are developing the construction of linear and branched metal complex oligomer and polymer wires by an interfacial stepwise coordination method and investigating electron conduction properties of internal molecular segments as well as the resistivity at the electrode-molecular wire junction. Also, the surface coordination programming of hetero molecular wires is being applied for development of cyanobacterial photosystem I (PSI)-based photosensors.



Visiting Associate Professor  
**UENO, Takafumi** (*from Kyoto University*)

### Novel Functional Nano Bio-Materials Based on Protein Assembly

Our research interests focus on the understanding, utilization, and design of protein assemblies that promote chemical reactions. We are developing strategies to functionalize natural protein assemblies as well as prepare artificial protein assemblies. This will expand the possibilities of our research into several emerging fields by bringing together the fields of organic chemistry, inorganic chemistry, biochemistry, molecular biology and structural biology.



Visiting Associate Professor  
**OYAMA, Dai** (*from Fukushima University*)

### Development of Highly Functionalized Transition Metal Complexes Based on Non-Innocent Ligands

Redox reactions are one of the most fundamental chemical reactions. Nature often utilizes redox-active organics in chemical transformations. Therefore, significant attention is currently focused on ligand-centered redox reactions in transition metal complexes.

We have investigated the synthesis and properties of the ruthenium complexes containing both pyridyl binding sites and azo, naphthyridine or quinone moieties which are closely related to biologically important molecules. In particular, we have studied on some important reaction systems such as multi-electron CO<sub>2</sub> reductions and H<sub>2</sub> evolution, based on proton-coupled electron transfer (PCET).